TECHNISCHE UNIVERSITÄT WIEN
Vienna University of Technology

D I S S E R T A T I O N

Installation
of a neutron beam instrument
at the TRIGA reactor in Vienna

Ausgeführt zum Zwecke der Erlangung des akademischen Grades eines Doktors der Technischen Wissenschaften unter Leitung von

Em. Univ.-Prof. Dipl.-Ing. Dr. Gerald Badurek
Dipl.-Ing. Dr. Erwin Jericha
und
Univ.-Prof. Dipl.-Phys. Dr. Hartmut Abele
E 141 - Atominstitut

eingereicht an der Technischen Universität Wien
Fakultät für Physik
von

DI Wilfried Mach
Matr. Nr. 00625363

Franz-Glaser-Gasse 36
1170 Wien

Wien, am 11. September 2018   Wilfried Mach

Zusammenfassung

Iᴍ Zuge dieser Arbeit wurde ein neuer Strahlplatz für thermische Neutronen mit einem weißen Spektrum und hohem Fluss geplant, simuliert, installiert und charakterisiert.

Der hohe Neutronenfluss von bis zu ~$10^7\,\mathrm{cm^{-2}\,s^{-1}}$ wird die Grundlage für eine Serie neuer Experimente sein. In Kombination mit der neuen Reaktorinstrumentierung des Tʀɪɢᴀ Reaktors in Wien, ist es möglich, den Reaktor zu pulsen. Dies ermöglicht einen peak flux von sogar ~$10^{10}\,\mathrm{cm^{-2}\,s^{-1}}$. Da alle anderen Beamlines am Tʀɪɢᴀ Reaktor ein monochromatisches Spektrum und daher einen um ungefähr drei Größenordnungen kleineren Fluss haben, wird dieser neue Strahlplatz die experimentellen Möglichkeiten am Atominstitut erheblich erweitern.

Allerdings führt ein so hoher Neutronenfluss einerseits und ein direkter Blick auf den Reaktorkern andererseits zu hohen Ortsdosisleistungen. Um diese zu minimieren, wurden innerhalb des Reaktorstrahlrohres Perfektkristalle aus Saphir und Wismut installiert. Die Dosisleistung verursacht durch schnelle Neutronen und γ-Strahlung wird hierdurch erheblich reduziert. Außerdem wurde eine neue Art von Strahlenschutzbeton entwickelt, um Dosisleistungslimits einhalten zu können. Borcarbid, Serpentinit und Hämatit als Zuschlagstoffe verbessern dessen Eigenschaften der Neutronenthermalisation und steigern die Absorptionswirkung von Neutronen und γ-Strahlung. Die Eigenschaften dieser neu entwickelten Betonsorte wurde mittels des strengen Geheimhaltungsauflagen unterliegenden Softwarepakets Mᴄɴᴘ6 [1] theoretisch simuliert und auch experimentell am Tʀɪɢᴀ Reaktor verifiziert. In der Folge wurde die gesamte Strahlenschutzkammer des neuen Strahlplatzes in Mᴄɴᴘ6 simuliert.

Überzeugt, dass das Design die vorgeschriebenen Limits an Ortsdosisleistungen erfüllen wird, wurde der Strahlplatz errichtet.

Nach Fertigstellung wurden die tatsächlichen Ortsdosisleistungen sorgfältig an einer beträchtlichen Anzahl von Messpunkten erhoben. Es zeigte sich, dass die Messwerte in voller Übereinstimmung zu den Simulationsergebnissen stehen. In Folge wurde die Betriebsbewilligung des Strahlplatzes nach §6 des Österreichischen Strahlenschutzgesetzes vom Bundesministerium für Wissenschaft, Forschung und Wirtschaft (BMWFW) erteilt.

Ambitionierte Forschungsprojekte werden an diesem neuen Strahlplatz in naher Zukunft durchgeführt werden, deren Realisation an den anderen Strahlplätzen des Reaktors nicht möglich wären. So werden wir zum Beispiel Grundlagenforschung vorantreiben, indem wir neue Instrumente zur Manipulation von Neutronenstrahlen entwickeln sowie bereits existierende weiter verbessern, wie etwa den magnetischen Neutronenspinresonator Mᴏɴᴏᴘᴏʟ [2], der unter anderem für das derzeit am Hochflussreaktor FRM II in München in Aufbau befindliche Hochpräzisons Beta-Zerfall Projekt PERC [3] sicherlich noch sehr von Nutzen sein wird. Natürlich wird der thermische weiße Strahl auch die neue Möglichkeiten als Neutronenradiographiestation eröffnen. Die Entwicklung von Neutronendetektoren mit Ortsauflösung im µm-Bereich ist nur eine weitere Möglichkeit zur Nutzung des neuen Strahlplatzes.

Nach ersten Tests am VCN-Strahl am PF2 des ILL in Grenoble im Jahr 2014 wurde vom Neutronenresonator MONOPOL ein gänzlich neuer Prototyp entwickelt, welcher Ende des Jahres 2018 das erste Mal am thermischen weißen Strahl dieser neuen Anlage des Atominstituts getestet werden soll.

Abstract

As described in this thesis, a new multi-purpose facility for a thermal white neutron beam with high flux was planned, simulated, installed and characterized.

Its high thermal neutron flux of up ~$10^7\,\mathrm{cm}^{-2}\,\mathrm{s}^{-1}$ will be the basis to realize a series of new experimental projects. In combination with the recently installed new instrumentation of the Vienna TRIGA research reactor, which allows to run this reactor in a pulsed mode of operation, it will even be possible to achieve a peak flux of ~$10^{10}\,\mathrm{cm}^{-2}\,\mathrm{s}^{-1}$. Taking into account that all other available beamlines of the TRIGA reactor are monochromatic and thus have a three orders of magnitude lower flux, such an intense neutron beam will lead to an immense broadening of the experimental possibilities at the Atominstitut.

However, high flux and a direct view to the reactor core lead to high radiation dose rates. Therefore, single crystals made of sapphire and bismuth were installed inside the reactor beam tube to filter out fast neutrons and γ-radiation in order to drastically decrease the total dose rate. Furthermore, a special kind of radiation absorbing concrete was designed as a biological shielding to meet radiation protection limits. Its content of boron carbide, serpentine and hematite as additives facilitates neutron thermalization and increases the absorption of both neutron and γ-radiation. The performance of this newly developed radiation protection concrete was simulated with the classified software package MCNP6 [1] and also verified experimentally at the TRIGA reactor. Subsequently the radiation shielding of the complete white beam facility was simulated using MCNP6.

Being confident that its design fulfills the ambient dose rate limits we finally have constructed the new facility.

After completion the real ambient dose rates were carefully measured at an extensive number of different positions. The experimental values turned out to be in full agreement with the simulation results. As a consequence, the legal permission to run this new facility was given by the Austrian Ministry of Science, Research and Economy.

In the immediate future we intend to use it for a series of ambitious new projects whose realization could not be conceived on the hitherto available beamlines of the TRIGA reactor. We definitely will push forward fundamental physics experiments by developing new and improving existing neutron beam manipulation devices, like e.g. the neutron magnetic spin resonator MONOPOL [2] which without doubt will become very useful for the high precision beta decay experiment PERC [3] that is currently under construction at the high-flux reactor FRM II in Munich. Clearly this white beam facility will also open new possibilities for us when used as a station for neutron imaging. The development of position sensitive neutron detectors with high spatial resolution in the µm-range is another topic of our research focus to be mentioned.

After first tests on the VCN-beam at the ILL in Grenoble in 2014 a new prototype of the neutron resonator MONOPOL will be tested for the first time on a thermal white neutron beam in end of 2018 on this new facility of the Atominstitut.

Contents

1. Introduction

1.1. The neutron & its plethora of applications

Since their discovery by Chadwick in 1932 [4] neutrons have become an incredibly versatile and indispensable tool for a still growing number of applications in scientific research. So-called slow neutrons, for instance, have kinetic energies comparable to collective excitations in solids, and according to the quantum physical wave-particle dualism they exhibit deBroglie wavelengths which are of the order of interatomic distances. Due to their electric neutrality, neutrons are able to penetrate even thick layers of matter and hence provide a nondestructive insight into the interior of large-volume samples. More than this, because of the lack of any Coulomb repulsion they are not shielded by the electron shell and thus may interact directly with the atomic nuclei. As a consequence, unlike to the case of X-ray scattering the neutron scattering amplitudes vary non-systematically from element to element and are even different for different isotopes of the same element, not only in size but even in sign. Due to their non-zero (anomalous) magnetic dipole moment, neutrons interact with matter not only via nuclear forces but also via electromagnetic dipole-dipole forces with the atomic shell electrons (the analogous interaction with the nucleons can usually be neglected because of their much larger mass), and thus are ideal to probe magnetic structures and excitations of solids. Therefore it is not at all surprising that neutron scattering experiments play a well-established essential role in condensed matter research. It is worth to mention, that the strong interaction between a neutron and a nucleus depends on their relative spin orientation but except for the special case of oriented nuclei this leads only to incoherent scattering contribution. But since magnetic dipole moments are always aligned along the particle spin, the magnetic dipole-dipole interaction between neutrons and the shell electrons depends also on the mutual orientation of the partners involved. Given the full alignment of the electron moments in samples that are magnetized to saturation, one may thus profit in investigating magnetic structures from the interference between the coherent nuclear and magnetic neutron scattering contributions by using fully polarized neutron beams, in particular if the spin state of the scattered neutrons is analyzed too. Unpolarized neutrons would be sufficient to separate just the intensity contributions of nuclear and magnetic scattering, but the underlying measurement procedure is less elegant and in general requires more experimental effort. It is necessary to magnetize the sample successively in two orthogonal directions, i.e. perpendicular and parallel to the scattering vector, whereas with polarized neutrons the orthogonal direction of the external magnetic field and just two measurements with simply achievable opposite spin orientations of the incident beam are sufficient. It has to be mentioned, however, that the finally detected count rates are at least one order of magnitude higher with unpolarized beams than with polarized ones, even if the experimental setup of the latter is equipped with state-of-the-art polarizing devices.

1. Introduction

Apart from their enormous importance for condensed matter research, neutrons are used in nuclear research and are indispensable for nuclear energy systems. Neutrons experience not only the strong and the electromagnetic interaction but also the weak and the gravitational force and they have become a unique and extremely sensitive quantum physical tool for a manifold of fundamental experiments in cosmology and particle physics (see e.g. [5]). Leaving nuclear physics applications with *fast*, *intermediate*, *resonance*, and *epithermal* neutrons which cover roughly the energy range from $1\,\mathrm{eV}$ to $20\,\mathrm{MeV}$ out of consideration here, the typical energies used in condensed matter and fundamental physics research span about seven orders of magnitude, ranging from *hot* ($E \sim 0.1-1\,\mathrm{eV}$), *thermal* ($E \sim 10-100\,\mathrm{meV}$), *cold* $E \sim 0.1-10\,\mathrm{meV}$) and *very cold* ($E \sim 0.3\,\mathrm{\mu eV}-100\,\mathrm{\mu eV}$) to *ultracold* ($E \leq 300\,\mathrm{neV}$) neutrons.

Europe has a long tradition in neutron scattering and still plays a leading role in this field of science. Currently 24 European active neutron research facilities exist, the three largest are the Institut Laue-Langevin (ILL) in Grenoble, whose high-flux reactor since 1970 is the most intense steady neutron source worldwide, the high performance Forschungs-Neutronenquelle Heinz Meier-Leibnitz (FRM-II) in Garching near Munich, Germany, and the ISIS Neutron and Muon Source spallation facility at the Rutherford Appleton Laboratory, near Oxford. There are, of course, important neutron research centers and high-flux neutron sources also in America, Africa, Asia and Oceania, as e.g. the High Flux Isotope Reactor (HFIR) and the next-generation Spallation Neutron Source (SNS) at the Oak Ridge National Laboratory (ORNL), the Los Alamos Neutron Science Center (LANCSE), the pulsed spallation neutron facilities KENS in Tsukuba near Tokyo, and JSNS at the Japan Proton Accelerator Complex (J-PARC) in Tokai, and the Australian Centre for Neutron Scattering (ANSTO) in Lucas Heights near Sydney, to name just a few examples. But without doubt the European Spallation Source (ESS), which now is under construction in Lund, Sweden, will allow Europe to stay at the foremost front and to set the pace for long time since it will be about a factor 30 (!) brighter than today's leading facilities.

One might expect that neutron research can only be performed effectively at high-flux sources. With respect to scattering experiments which are required for probing condensed matter this is roughly true, indeed. But one should not forget that beam time at the instruments of large scale facilities is very costly and thus is allocated only after competitive peer-reviewed selection of the best experiment proposals. It is clear that there is almost no room left for on-site preparatory tests of the often new setup components and/or new measurement procedures. This is *the* domain where even low-flux neutron sources like the small $250\,\mathrm{kW}$ TRIGA reactor of the Atominstitut become very important due to their incomparably higher flexibility and freedom with respect to verify the principal feasibility of often unconventional, if not 'crazy', new methodical concepts. There is indeed a long and successful tradition at the Atominstitut in developing new experimental techniques, in particular if polarized neutrons are involved. For instance more than thirty years ago the hitherto fastest chopper was developed, allowing to produce very short pulses of polarized neutrons without any mechanical intervention [6]. Since the pulses were achieved just by purely electronic means both their width and their

repetition rate could be varied almost instantaneously and completely independent from each other. Another spectacular new conceptual idea emerging from the Atominstitut was the so-called *dynamic neutron polarization* (DNP) method [7], which for the first time should allow one to convert an unpolarized neutron beam at the cost of a tiny energy difference between the two initial neutron spin states into a fully polarized one without the normally unavoidable intrinsic loss of 50% of the incoming neutron flux. However, although its principal feasibility was checked both by thorough analytical analysis [8, 9] and numerical simulations [10, 11] it still waits for its experimental realization because of its highly sophisticated and correspondingly expensive technical requirements, which are based on the inelastic interaction of neutrons and radio-frequency fields [12]. In 2002 a novel *traveling-wave* mode of operation [13, 14] of a neutron monochromator/chopper assembly based on spatial magnetic spin resonance [15–17] was suggested in order to decouple its wavelength resolution from its achievable time resolution. In recent years several prototypes of such traveling-wave neutron spin resonators have been developed at the Atominstitut. The first experimental tests at the TRIGA reactor could be performed only with a dichromatic beam of thermal neutrons delivered from 1st and 2nd order (002)-reflection of a highly oriented pyrolytic graphite (HOPG) monochromator [18]. Nevertheless these experiments allowed to improve the resonator performance step-by-step from one prototype to the next and to demonstrate that the proposed concept is indeed useful for flexible neutron beam property tailoring. The most advanced of these prototypes, named MONOPOL_3.1, was designed and optimized for installation at the PF2-VCN beam line at the high-flux reactor of the ILL Grenoble, where it could be tested recently for the first time with a *white* beam of very cold neutrons [2, 19].

As a first 'real' application MONOPOL will be implemented in the PERC (proton and electron radiation channel) project [20] which is currently under construction at the beam facility MEPHISTO at the high-flux reactor FRM II in Garching by an international collaboration of several universities (Technische Universiät München, Universität Heidelberg, Universität Mainz, Technische Universität Wien) and the Institut Laue-Langevin in Grenoble [3, 21]. PERC is a new user facility for high-precision measurements of angular correlations in the beta decay of free cold neutrons, delivering an intense beam of decay electrons and protons whose spectra and angular distributions will be free of distortions and with an expected background at a level of 10^{-4}, i.e. about ten times better than hitherto achieved. It is a lucky coincidence that many precisely measurable entities of neutron physics are linked with theories 'beyond the Standard Model (SM)' of particle physics. For instance, the electric dipole moment of the neutron is practically zero ($d < 0.30 \times 10^{-25}$ e cm), but supersymmetry predicts a non-zero value whose experimental verification would be the first proof ever for the hitherto never observed violation of T-invariance. Undoubtedly such a spectacular finding would lead to a complete paradigm change of our understanding of the universe. Another topic of extreme interest is the precise measurement of weak interaction parameters that are accessible via the neutron beta-decay. Since from such decay experiments more parameters can be determined than are needed in the electroweak standard model they open a window of opportunity to provide important new insights both into and also beyond the

Standard Model (SM) of particle physics. Exploiting the incredibly high level of precision experiments with cold and ultracold neutrons have reached, PERC definitely will play a leading role in this forefront field of physics research.

But probably the most spectacular scientific breakthrough that until now has ever emerged from the Atominstitut was the invention of perfect crystal neutron interferometry by Prof. H. Rauch, head of the institute from 1972-2005 [22], which allowed for the first time to split a neutron matter-wave with a wavelength of the order of 0.1 nm coherently into two sub-waves that were separated over a macroscopic distance of several centimeters and to recombine them again to yield clearly visible interference fringes. Since then a still ongoing series of really breathtaking pioneering quantum physical experiments has been successfully realized by his group, whose description would be beyond the scope of this short introduction (for a comprehensive survey see [23]). Likewise fascinating new vistas have opened up due to recent spectacular observations of neutron quantization in the Earth's gravitational field [24]. In order to study gravitational and cosmological problems an ambitious project, *q*BOUNCE , was initiated at the Atominstitut by Prof. H. Abele. Within the framework of this project a new method of '*gravitational resonance spectroscopy*' (GRS) was developed over the last few years which in formal analogy to magnetic resonance spectroscopy (MRS) allows to stimulate resonant transitions between such discrete gravitational energy states of the neutrons [25, 26]. These experiments have set new constraints on deviations from Newton's gravitational law at the micrometer scale which are predicted in theories with extra dimensions that propose unification of the Planck scale with the scale of the Standard Model. *q*BOUNCE provides a totally new opportunity to either find additional hypothetical forces and fields similar to gravitation, or to exclude their existence with absolute certainty. In this context it should be mentioned that a recent neutron interferometric experiment performed at the instrument S18, that is operated at the ILL Grenoble under the exclusive responsibility of the Atominstitut, could set stringent limits for a scalar so-called '*chameleon field*', a prominent quintessence dark energy candidate [27].

1.2. Motivation to realize a *Thermal White Neutron Beam* facility at the Triga reactor

As stated already in the previous Section, neutron scattering experiments at small research reactors can of course not compete with those performed at high-flux facilities. Only thermal but no cold neutrons are available at the Atominstitut, and the installation of a cold neutron source will very likely remain out of reach because of the required high investment and operational costs. From the horizontal plan of the TRIGA reactor plotted in Fig. 1.1 both the position and the nomenclature of its beam channels can be seen. The channels denoted A, B, and C are directed radially towards the rector core, whereas channel D is a tangential one. There are two additional beam ports, the *Thermalizing Column* and the *Thermal Column* where the neutrons have to penetrate through massive graphite blocks of about 1 m thickness and consequently have a very pure thermal energy spectrum with almost

negligible contamination with particles of higher energy. These two ports are used for neutron radiography, which is a typical application of small reactors as it allows to perform useful material oriented research even with moderate neutron flux. The radiography facility at the thermal column is mainly used for high resolution investigations of small samples not larger than about 9 cm in diameter and can be handled even by undergraduate students. The other serves for inspection of larger objects ($d_{max} = 35$ cm) on an industrial scale, but it suffers from the fact that it is not easily accessible. Inside of beam channel A a pneumatic transfer system is installed that is at present dedicated exclusively to the local radiochemistry group for thermal neutron activation analysis (TNAA) and thus is not available for other purposes.
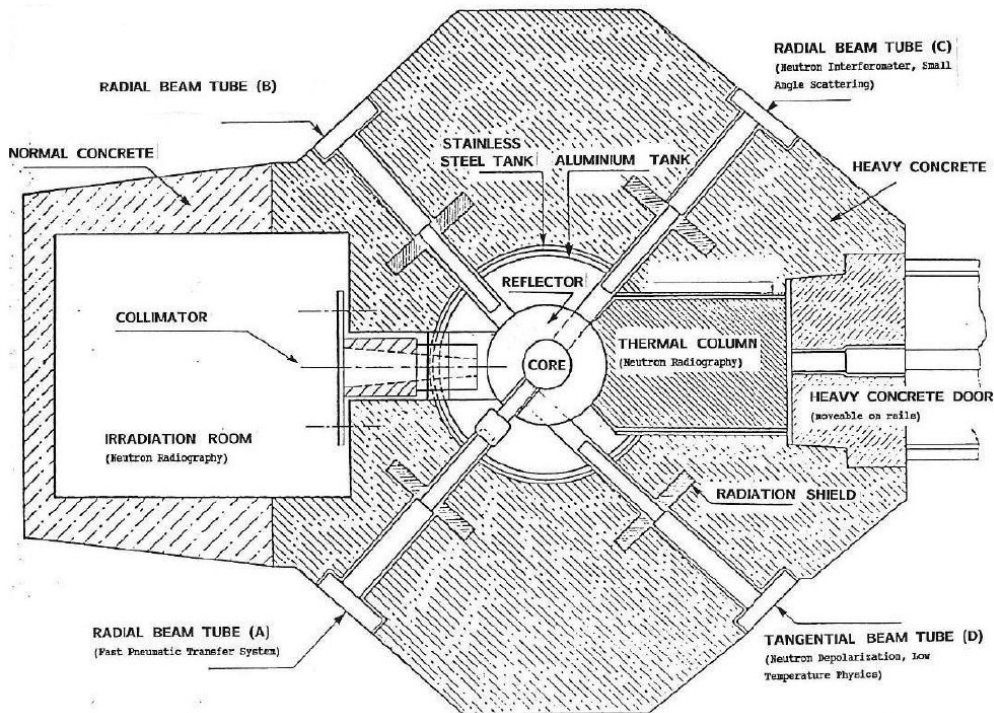
Fig. 1.1.: Position and nomenclature of the TRIGA beam channels.

With the exception of a special test setup of a so-called 'Fourier time-of-flight diffractometer' [28] all neutron *scattering* experiments that have been performed so far since the first criticality of the TRIGA reactor on March 7, 1962, at the three available beam channels B, C, and D exclusively used monochromatic neutrons because it was impossible to handle polychromatic beams outside of the solely available 'standard' heavyweight concrete radiation shielding elements without running into severe radiation protection problems. As it was the case also at radial channel B before its recent update, the beam lines installed at channels C and D use Bragg-reflection at highly oriented pyrolithic graphite (HOPG) mosaic single crystals to produce monochromatic neutrons with correspondingly rather low neutron flux of typically about$(10^1 - 10^4 \text{cm}^{-2}\,\text{s}^{-1})$ which can propagate through appropriate apertures in the heavy-concrete blocks to the respective experimental setups (see Figs. 1.2 and 1.3).

Fig. 1.2.: Massive heavyweight concrete blocks for radiation shielding are placed around the beam channels B, C, and D, where Bragg reflection at HOPG crystals is used to guide monochromatic beams through apertures of the radiation shields to the experimental setups. Between the channels C and D the radiography unit at the thermal column is seen, which is less demanding with respect to radiation protection. Right bottom corner: experimental installations at beam line B before the recent update.

In spite of the inevitable restriction to monochromatic thermal neutrons an appreciable number of innovative methodical concepts and pioneering new experiments were conceived at the Atominstitut, but for most of them only preparatory feasibility tests could be done there. For their full experimental realization it was almost always necessary to use foreign large scale neutron research facilities. Without doubt the most important example is the previously mentioned perfect crystal neutron interferometer which has been developed at the Atominstitut and was then '*exported*' successfully to the ILL Grenoble. Other, less spectacular examples of experiments that were prepared at the Atominstitut but could then be performed successfully only at foreign neutron scattering centers are the development of an inverted geometry polarized neutron time-of-flight spectrometer with electronically tunable energy analyzer [29] the demonstration of polarized neutron space-time focusing [30], or the unambiguous verification of the topological nature of the 'Scalar Aharonov-Bohm Effect' [31].

Simply because of limited monetary resources for more than 50 years it seemed

Fig. 1.3.: The beam line at the radial channel B of the TRIGA reactor in Vienna before the recent upgrade. A HOPG mosaic single crystal, mounted in front of the beamtube at the center of the heavyweight concrete radiation shielding, reflects a monochromatic beam out of the main beam. As it can be seen, its trajectory is almost parallel to the reactor wall. The components in the foreground are just residuals of a previous experimental setup.

to be not realistic that it would ever be possible to provide a polychromatic neutron beam at one of the channels of the TRIGA reactor which could be used safely for any kind of neutron scattering experiment and/or just for testing newly developed technical equipment. But in the course of the renewal of the reactor control instrumentation and the appointment of Prof. Abele the responsible ministry was inclined to give a sufficiently high financial donation to the Atominstitut to install a new *Thermal White Neutron Beam* facility, with the clear goal to broaden the scope of scientific applications of the TRIGA research reactor. Since, apart from scientific research, training of students and external users, as for instance international experts from the IAEA, plays also an important role at the TRIGA reactor Vienna, an '*easy to use*'-concept of this new facility was of particular importance. Therefore its design criteria aimed to establish the following characteristics

- High neutron flux ($\gtrsim 10^6\,\mathrm{cm^{-2}\,s^{-1}}$)
- Low γ-radiation background
- Large beam diameter ($\gtrsim 60 \times 60\,\mathrm{mm^2}$)
- Easy access
- High flexibility
- Ease of use
- No violation of ambient dose rate limits ($< 5\,\mathrm{\mu Sv/h}$)
- Compliance with Austrian laws and regulations [32, 33]

which reveal that a configuration with high flexibility and consequently low specialization was clearly favored.

After thorough discussion within our group we decided that it would be the best way to obey the ambient dose rate limits by building a shielded chamber which is large enough to allow the installation of any kind of neutron scattering experiment without the need of guiding the polychromatic neutron beam to any location outside of the chamber. To allow access to the instrument at any time without a reactor shutdown it was therefore necessary to implement a carefully designed and safely operating beam shutter which is coupled to a likewise safe interlock system to the entrance door of the chamber. To facilitate right from the start the conception of the elaborate organizational and technical tasks which had to be resolved, Fig. 1.4 shows already here an exterior view of the new *Thermal White Neutron Beam* facility at beam channel B of the TRIGA reactor immediately after its completion end of May 2018. In the following chapters and sections its constructional details and the necessary steps towards its realization will be described.

However, before we do so, we dedicate the remainder of this chapter to the presentation of the necessary legal requirements and the preparatory actions of civil works.

1.3. Supplementary notes

After first experimental tests and simulations the feasibility of the new neutron beam facility (see Chapter 3) was shown. The facility was planned in all details: a

Fig. 1.4.: The shielding chamber of the new thermal white neutron beam facility at the TRIGA reactor. The chamber (red) has a size of $\sim 5.2 \times 4.2 \times 2.2 \, \mathrm{m}^3$. The reactor (yellow) can be seen in the back. The entrance to the interior of the chamber is regulated by the mesh door which is part of a sophisticated interlock system. This allows access to the installed experimental setup at any time without requiring a rector shutdown.

specification sheet (Leistungskatalog) was worked out to define all details of the new facility. Further, a call for bids (Ausschreibung) was necessary because of the expectable price of the facility. This was organized in cooperation with the legal department of the TU Wien. Civil engineers[1] verified the load capacity of the reactor hall floor (described in section 1.3.2), since the reactor hall is with basement and a detailed constructional drawing was created respecting all details of application (such as necessity of self-assembly and disassembly, hall crane load, delivery, cable feedthroughs, maximal gap dimensions between concrete elements, edge protection, floor leveling,...). Companies for mixing the special concrete, for pouring the precast concrete parts and for building the chamber at the reactor in Vienna were searched for.

Since §5 StrSchG (Federal radiation protection law of Austria, described in Section 1.3.1 and in [32]) prescribes a license from the Ministry of Science, Research and Economy of Austria for this kind of radiation sources, details of the project were planned in close collaboration with the ministry and their external consultants to improve the quality of this project by implementing their suggestions and to meet legal requirements.

After all these organizational challenges, the call for bids was started in autumn 2016, the bid was accepted at the end of 2016, the concrete parts were casted in February 2017 and the facility was installed in March 2017. Small jobs like e.g. painting the chamber walls were done in April 2017.

After that, first tests with external consultants started in May 2017. An official test run was requested in May and normal operation was permitted in September 2017 by the ministry of science, research and economy of Austria.

During the test run, first measurements to characterize the new facility were done. The characterization was finished at the end of 2017. These results are described in Chapter 4 in detail.

1.3.1. Statutory provisions

Any institution which is responsible to operate a nuclear reactor is obliged to strictly obey legal regulations. Thus it evidently follows that any fundamental modification of existing or implementation of new facilities which are essential for the safe operation of the reactor requires approval by a higher-ranking authority. According to §5 StrSchG (Austrian Federal Radiation Protection Law) [32], which reads as

> §5 (l) Die Errichtung von Anlagen für den Umgang mit Strahlenquellen, die im Hinblick auf deren Betrieb schon bei ihrer Errichtung die Vorbereitung und Durchführung von Maßnahmen für den Strahlenschutz erfordern, bedarf einer Bewilligung. Vor Erteilung der Bewilligung dürfen solche Anlagen nicht errichtet werden.

it was thus necessary to get an approval from the responsible Austrian Federal Ministry of Education, Science and Research to build and to run such a new

---

[1]Fröhlich & Locher und Partner Zivilgesellschaft m.b.H.

Thermal White Neutron Beam facility. Therefore the planning, the installation, and also the first test measurements were done in close collaboration with the ministry and its external consultants for radioprotection[2].

To simplify both the procedure of its approval and its construction the *Thermal White Neutron Beam* facility was planned to need no changes of the existing structure of the reactor hall and the reactor itself. Therefore, no re-approval of the reactor was necessary. Additionally, the whole chamber is neither fixed permanently to the reactor nor to the reactor hall. If necessary it can therefore be disassembled and moved aside by the team of reactor operators without any serious difficulty, just like a precious piece of furniture.

As it is regulated in §5 StrSchG [32], after the whole project definition was completed [34], it was possible to successfully request an approval for construction ('Errichtungsbewilligung') by the ministry at November 16, 2016. It should be noticed here that the invaluable collaboration with the two external consultants resulted in some minor but nevertheless very important improvements (concerning activation analysis, assessment of fire load, minor details on the interlock system and on scattered neutrons) which then had been included in the final project definitions, see Refs. [35] and [36].

In addition to the set of regulations concerning the radioprotection law it was also necessary to comply with other statutory provisions, as e.g. the employee protection law ('Arbeitnehmerschutzgesetz'), and with some internal administrative standards. Due to the size of the project, a *call for bids* was required.

1.3.2. Preparatory civil works

The detailed construction plans of the radioprotection chamber of the *Thermal White Neutron Beam* facility were drawn by civil engineers. Since the weight of this heavy concrete chamber is about 50 tons and the reactor hall has got a basement underneath, it was an absolute must to check in advance whether the given floor load limit of $5\,\mathrm{t\,m^{-2}}$ is sufficient to sustain such a massive weight. The civil engineer's report finally confirmed that referring to the floor load no further building measures are necessary [34].

As already mentioned in the previous section, the radiation protection chamber is just standing on the regular reactor hall floor but is not fixed permanently to the reactor hall. Since the flatness of the floor is of crucial importance for correct assembling of the chamber the floor flatness had to be characterized carefully by the civil engineers which were responsible for the general construction survey. Of course, also the exact dimensions and orientations of both the reactor walls and the radiation channel B had to be precisely measured in order to match the chamber as accurate as possible to the reactor wall and to align it along the neutron beam axis. As it can be seen in Fig. 1.5, the floor is not very flat indeed: the height difference between the highest and the lowest point of the dedicated part of the floor is about 1.4 cm. Therefore a properly designed floor support had to be built prior to the installation of the chamber.

---

[2]Dr. Gabriele Hampel, 2014-15 Präsidentin des Deutsch-Schweizerischen Fachverbands für Strahlenschutz, and Ing. Harry Fluhr, Landesamt für Umweltschutz Rheinland-Pfalz, Mainz
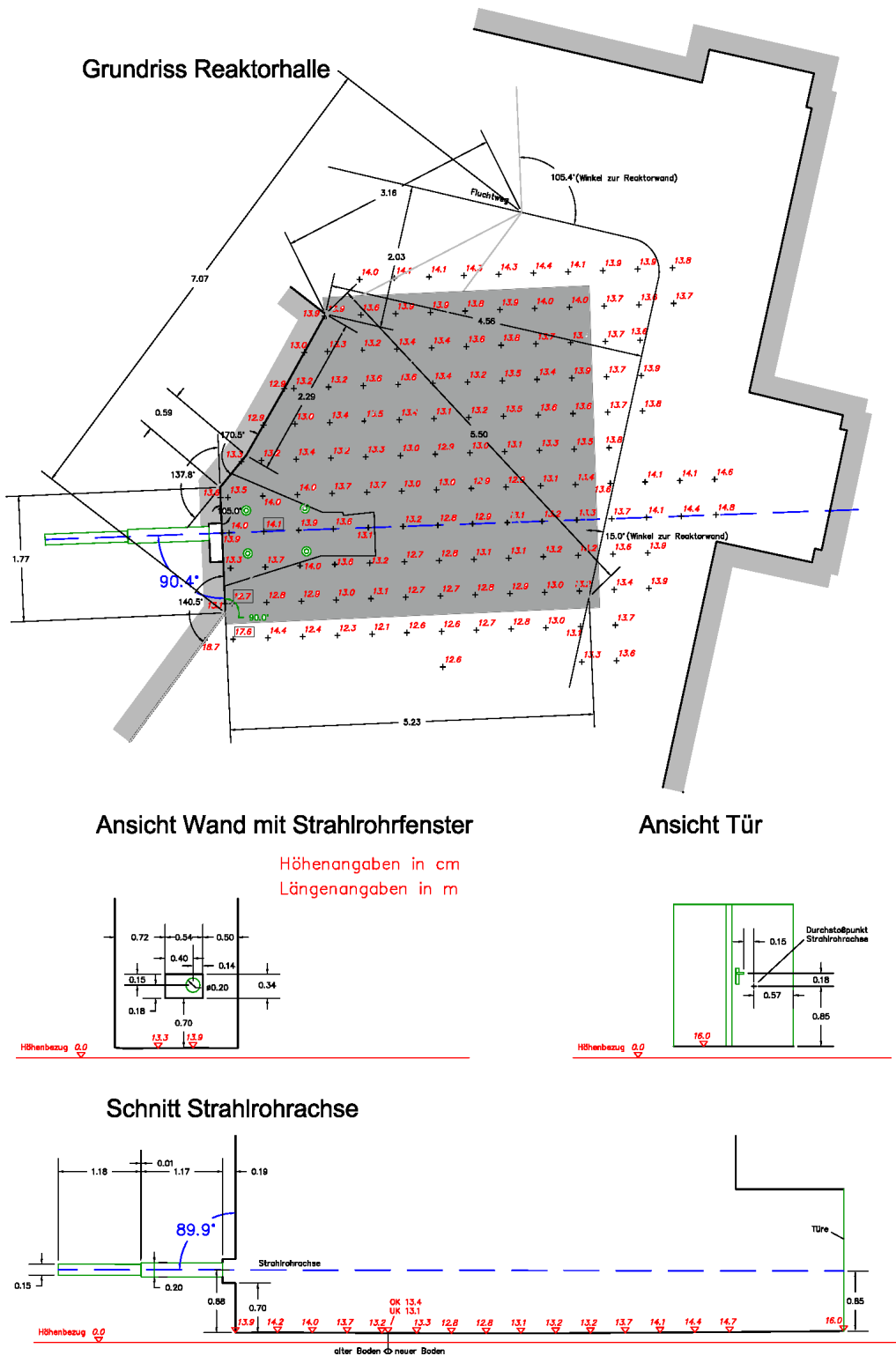
Fig. 1.5.: Survey of the dimensions of the reactor hall and the flatness of the floor where the radiation protection chamber is located (colored in grey), the position of beam channel B, and of its beam axis. Heights are given in cm, lengths in m.

2. The Impact of Single Crystal Filters on Neutron Spectra

THE objective of the new beam facility is the flexible provision of a *thermal* white neutron beam for different future experiments.

However, due to the direct view to the reactor core the neutron beam of beamtube B will contain a significant portion of unwanted reactor γ-radiation[1], but also epithermal and fast neutrons. This 'contamination' of the thermal neutron beam needs to be minimized for three reasons:

Background - epithermal and fast neutrons are often a major source of background in detectors.

Dose rate - epithermal and fast neutrons cause an up to 400 times higher radiation dose in the human body than thermal neutrons, as it can be seen in Fig. 2.1.

Shielding - since radiation shielding of neutrons always implies that neutrons are absorbed, the $\frac{1}{v}$-dependency of the absorber is crucial. That leads to much bulkier absorbers for fast neutrons and therefore to less free space for experiments, and consequently also to higher costs.

In order to minimizing this contamination it has to be quantified first. Therefore, a short and general survey of neutron flux spectra is given in Section 2.1. After that, in Section 2.2 the flux spectrum of a nuclear reactor with its specific characteristics is explained and the theoretically simulated spectrum is compared with the experimentally measured flux distribution at beamtube B of the TRIGA reactor. As expected, the latter is not entirely thermal as favored.

One common way of getting rid of the unwanted components is using curved neutron guides of several meters of length. By total reflection these neutron guides transport only slow neutrons, but no γ-radiation or fast neutrons which are absorbed at the very beginning of the guide. Due to the very small critical angles of total neutron reflection (see Section 5.1) and the correspondingly large radii of curvature these guides are at least several meters long. Unfortunately they are therefore no option for our project due to limitations imposed by the available space.

A further possibility of minimizing the unwanted fast neutron and reactor-γ components is to use neutron filters. These filters scatter out fast neutrons utilizing solid-state effects, while thermal neutrons pass the filter material. Thus, the neutron spectrum is modified massively. Besides that, a filter made of a material with high density also improves the γ-component.

The physics behind neutron filters will be described in Section 2.3. With that knowledge the required physical properties of neutron filters will be shown and a

---

[1]Reactor γ-radiation: γ-radiation coming out of the reactor core. It is collimated like the neutron beam itself. Contrary, *secondary γ-radiation* which is generated by neutron absorption in the shielding material is not collimated at all but diffuse.
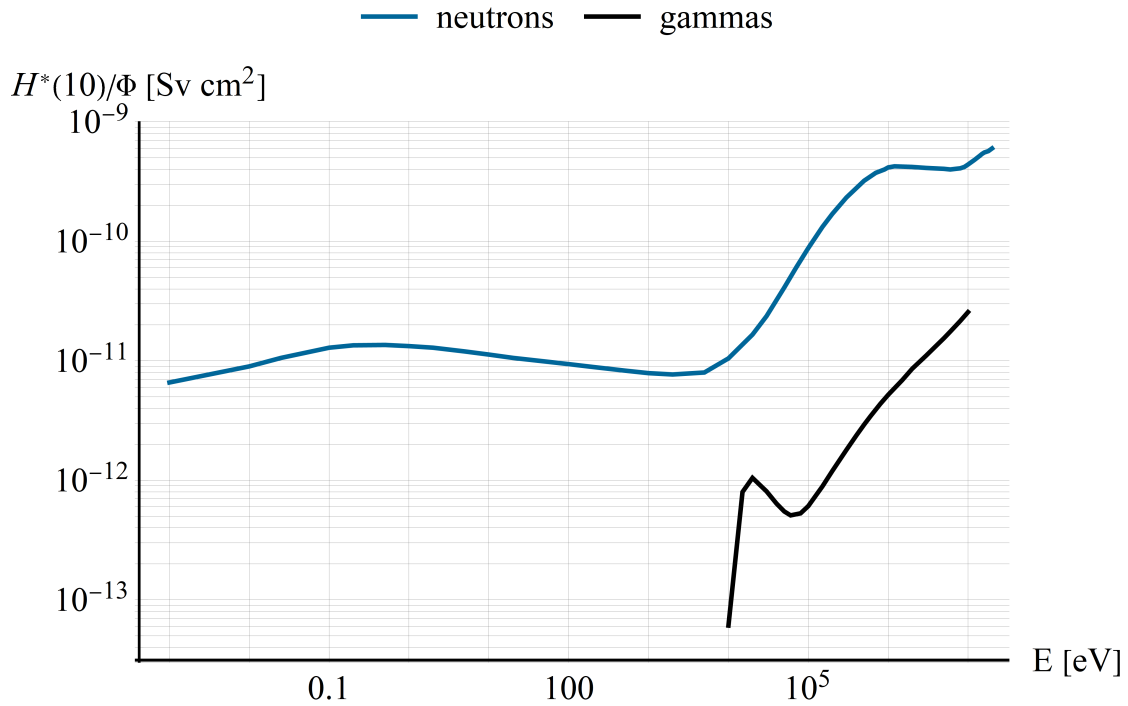
Fig. 2.1.: Plot of the energy dependency of the ambient dose equivalent $H^*(10)$ from ICRP 74 [37].

discussion about different filter materials and the chosen filters can be found in Section 2.4.

With the background mentioned above in Section 2.5 a filter transmission function is calculated. As described in Section 2.6, applying this transmission function on the known neutron flux spectrum of the TRIGA reactor will finally lead to the *Thermal White Neutron Beam's* spectrum that is delivered at the exit of beamtube B.

2.1. Considerations on neutron flux and flux spectra

A short survey on the manifold possibilities on representing the spectral distribution of an ensemble of neutrons shall be given in this Section.

2.1.1. Gedankenexperiment on discrete probability distributions

Let us imagine a vessel, containing 50% neutrons with the velocity v_1 and 50% neutrons with the velocity v_2, where $v_2 = 2v_1$.

The probability distribution of the velocities of the neutrons is measured by drawing neutrons out of the vessel randomly, measuring their velocity and putting the neutron back in the vessel. The measured probability distribution is called velocity **spectrum** $\hat{N}(v)$. In this case it is discrete, dichromatic and equally distributed as it is shown in Fig. 2.2.a.

(a) dichromatic spectrum
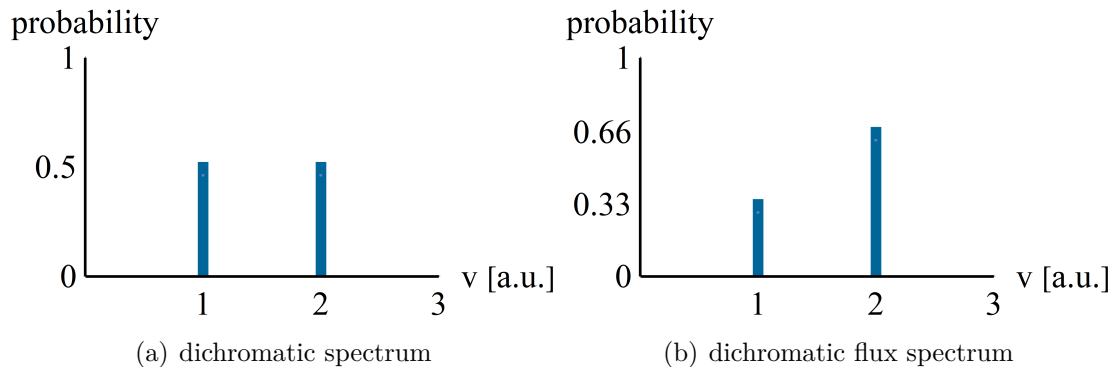

(b) dichromatic flux spectrum

Fig. 2.2.: The difference between spectrum (left) and flux spectrum (right) of a dichromatic ensemble of gas atoms which are distributed equally on the velocities v_1 and v_2 with $v_2 = 2v_1$.

Contrary, if we mount a detector on the wall of the same vessel, the faster neutrons are detected more often by the detector since they have twice as much wall contacts, thus twice as much detector contacts. Therefore, a third of the measured neutrons will have v_1 and two-thirds will have v_2, see Fig. 2.2.b. The measured distribution is called velocity **flux spectrum** $N_{Flux}(v)$.

The difference of these two probability distributions is due to the different act of drawing the neutron. In the case of the velocity spectrum the neutron is drawn fully randomly - the probability of being drawn is equal for every neutron. For the flux spectrum the probability of being drawn is proportional to the neutron's velocity. Thus, the velocity spectrum and the velocity flux spectrum are connected:

$$N_{Flux}(v) = \hat{N}(v) \, \frac{v}{\bar{v}} \tag{2.1}$$

where $\bar{v}$ is the mean velocity of the neutron ensemble:

$$\bar{v} = \int_0^\infty \hat{N}(v)v.$$

Another important quantity to characterize neutron beams is the neutron flux:

$$\Phi(v) = N_0 N_{flux}(v)$$

with N_0 as the total number of neutrons per unit volume. When velocity distributions of particles are measured as in the second part of the Gedankenexperiment (with putting the neutron back in the vessel, by drawing not all neutrons in the vessel or by having a huge amount of neutrons inside the vessel), the particle selection process is always dependent on the particle velocity. Thus, these measured velocity distributions are flux spectra and not spectra. Most particle measurement techniques and all measurement techniques used for this thesis were techniques like those in the second part of the Gedankenexperiment, thus all measured neutron velocity distributions are neutron flux spectra.

2.1.2. The Maxwell-Boltzmann flux distribution

Relation (2.1) is not only valid for discrete probability distributions but also for continuous ones. The velocity dependent Maxwell-Boltzmann probability distribution [38]

$$\frac{d\hat{N}_0}{dv} = N_0 \; \hat{N}(v) = N_0 \; \left(\frac{2}{\pi}\right)^{\frac{1}{2}} \left(\frac{m_n}{k_B T}\right)^{\frac{3}{2}} v^2 \; e^{-\frac{m_n v^2}{2k_B T}} \; ,$$

where m_n is the mass of the neutron, k_B the Boltzmann constant, and T the moderator temperature, can therefore be rewritten as a Maxwell-Boltzmann flux spectrum distribution

$$\frac{dN_0}{dv} = N_0 \; N_{Flux}(v) = \Phi(v) = N_0 \; \frac{1}{2} \left(\frac{m_n}{k_B T}\right)^2 v^3 \; e^{-\frac{m_n v^2}{2k_B T}}. \tag{2.2}$$

As can be seen in Fig. 2.3, the flux spectrum is shifted and contains more faster neutrons as described in Section 2.1.1. It is noteworthy that both the spectrum and the flux spectrum describe the neutron ensemble correctly but in a different way. For the experimentalist, the flux spectrum is the more important entity, since in almost every experiment he draws his particles depending on their velocity, like in the second part of the Gedankenexperiment.

Since neutron energy E, velocity v, wavelength λ and flight-time of the neutron t_{TOF} are connected by

$$E = \frac{m_n v^2}{2}, \qquad \lambda = \frac{h}{m_n v}, \qquad E = \frac{m_n l_{\mathrm{TOF}}^2}{2 t_{\mathrm{TOF}}^2} \tag{2.3}$$

neutron flux spectra can be described as a function of all of these properties, and Eq. (2.2) can therefore be rewritten as:

$$\frac{dN_0}{dE} \;=\; N_0 N_{Flux}(E) \;=\; \Phi(E) = N_0 \;\;\frac{E}{(k_B T)^2} \;\; e^{-\frac{E}{k_B T}} \tag{2.4}$$

$$\frac{dN_0}{d\lambda} \;=\; N_0 N_{Flux}(\lambda) \;=\; \Phi(\lambda) = N_0 \; \frac{1}{2} \left(\frac{h^2}{m_n k_B T}\right)^2 \; \frac{1}{\lambda^5} \;\; e^{-\frac{h^2}{2k_B T m_n \lambda^2}} \tag{2.5}$$

$$\frac{dN_0}{dt_{\mathrm{TOF}}} = N_0 N_{Flux}(t_{\mathrm{TOF}}) = \Phi(t_{\mathrm{TOF}}) = N_0 \;\; \frac{1}{2} \; \left(\frac{m_n}{k_B T}\right)^2 \; \frac{l_{\mathrm{TOF}}^4}{t_{\mathrm{TOF}}^5} \; e^{-\frac{m_n l_{\mathrm{TOF}}^2}{2k_B T t_{\mathrm{TOF}}^2}}. \tag{2.6}$$

In Fig. 2.3 the effect of the differential in Eqs. (2.2), (2.4), (2.5) and (2.6) is illustrated: the vertical lines corresponding to steps of $300\,\mathrm{m\,s^{-1}}$ are equidistant only in the velocity plots but not in the other plots where they had to be recalculated by using Eq. (2.3). This means that the maximum of a spectrum cannot be recalculated for a different physical quantity simply by using Eq. (2.3) without taking into account the differential too. While e.g. the maximum of the Maxwell-Boltzmann
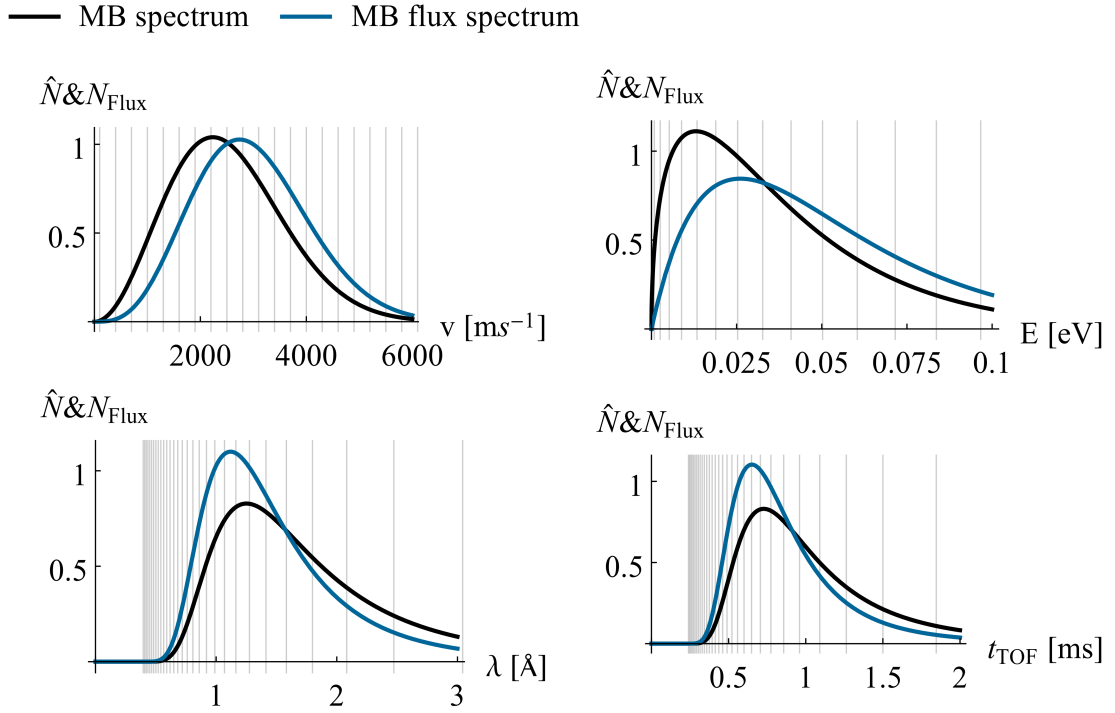
Fig. 2.3.: The ideal Maxwell-Boltzmann spectrum and the Maxwell-Boltzmann flux spectrum for neutrons leaving a moderator with $303\,\mathrm{K}$ plotted as functions of velocity v, energy E, wavelength λ, and flight-time t_{TOF} over a distance of $2.3\,\mathrm{m}$. Notice that the vertical lines corresponding to velocity steps of $300\,\mathrm{m\,s^{-1}}$ are equidistant only in the velocity plots (see the text).

flux spectrum for $303\,\mathrm{K}$ is at $2737\,\mathrm{m\,s^{-1}}$, corresponding to an energy of $26.10\,\mathrm{meV}$, one would obtain a totally wrong value of $39\,\mathrm{meV}$ if the influence of the differential is ignored and only Eqs. (2.3) is used for calculating the energy of the spectrum maximum. Tabs. 2.1 and 2.2 summarize the possibilities of characterizing a given (flux) spectrum.

2.2. A nuclear reactor's neutron flux spectrum

The neutron flux spectrum of a nuclear reactor can be divided in three characteristic energy regions:

fast region - neutrons released by the fission process from ^{235}U evaporate from the nucleus. Therefore, their energies are Maxwell-Boltzmann distributed around the mean energy of the process which is about $2\,\mathrm{MeV}$. Often this spectrum is described by the Watt-fission spectrum [40]:

$$\Phi_{fis}(E) = k_1 sinh(k_2 E)e^{-\frac{E}{k_3}}.$$

with $k_1 = 0.453$, $k_2 = 0.965$ and $k_3 = 2.29$ for the fission of ^{235}U [41].

Maximum	energy [meV]	velocity [ms^{-1}]	wavelength [Å]
spectrum	13.05	2235	1.25
flux spectrum	26.10	2737	1.12

Tab. 2.1.: Maxima (the most probable values) of a Maxwell-Boltzmann spectrum and flux spectrum (303 K [39]) expressed in energy, velocity and wavelength.

Mean	energy [meV]	velocity [ms^{-1}]	wavelength [Å]
spectrum	39	2522	2.00
flux spectrum	52	2971	1.57

Tab. 2.2.: Mean of a Maxwell-Boltzmann spectrum and flux spectrum (303 K [39]) expressed in energy, velocity and wavelength.

epithermal region - the neutrons released from the fission process scatter with the moderator material. Independently from the initial energy of the neutron, with every scattering process, the neutron loses the same fraction of energy. This results in a *1/E*-energy dependency.

thermal region - when the neutron ensemble is in the same energy regime as the moderator material - for a moderator temperature of $\sim$300 K this is the 100 meV-regime - the neutron ensemble is in thermal equilibrium with the moderator. Again, the neutron spectrum therefore is Maxwell-Boltzmann distributed.

Following [41] these three regions can be described mathematically by

$$\Phi_{fis}(E) = C_3 \sqrt{E} e^{-\beta E} \tag{2.7}$$

$$\Phi_{epi}(E) = \frac{C_2}{E^\alpha} \tag{2.8}$$

$$\Phi_{therm}(E) = C_1 \frac{E}{(k_B T)^2} \; e^{-\frac{E}{k_B T}} \tag{2.9}$$

where E is the energy, C_1, C_2 and C_3 are normalization constants. $\alpha = 1$ for infinitely thick moderators without absorption and $\alpha > 1$ for real moderators. β is a parameter describing the reactor type.

Since these three Eqs. combined describe a neutron reactor flux spectrum and the spectrum needs to be continuous in the transition regions at about 0.4 eV and 1 MeV a transition function for the continuous transition at these energies is required [41]:

$$f_{therm,epi}\left(\frac{E}{k_B T}\right) = \left\{ \begin{array}{r} 0 \\ 1 + 1.6(\frac{E}{k_B T} - 5)e^{-\frac{E}{3k_B T}} \end{array} \right\} \text{ for } \left\{ \begin{array}{l} 0 \leqslant \frac{E}{k_B T} \leqslant 3.19 \\ \frac{E}{k_B T} > 3.19. \end{array} \right. \tag{2.10}$$
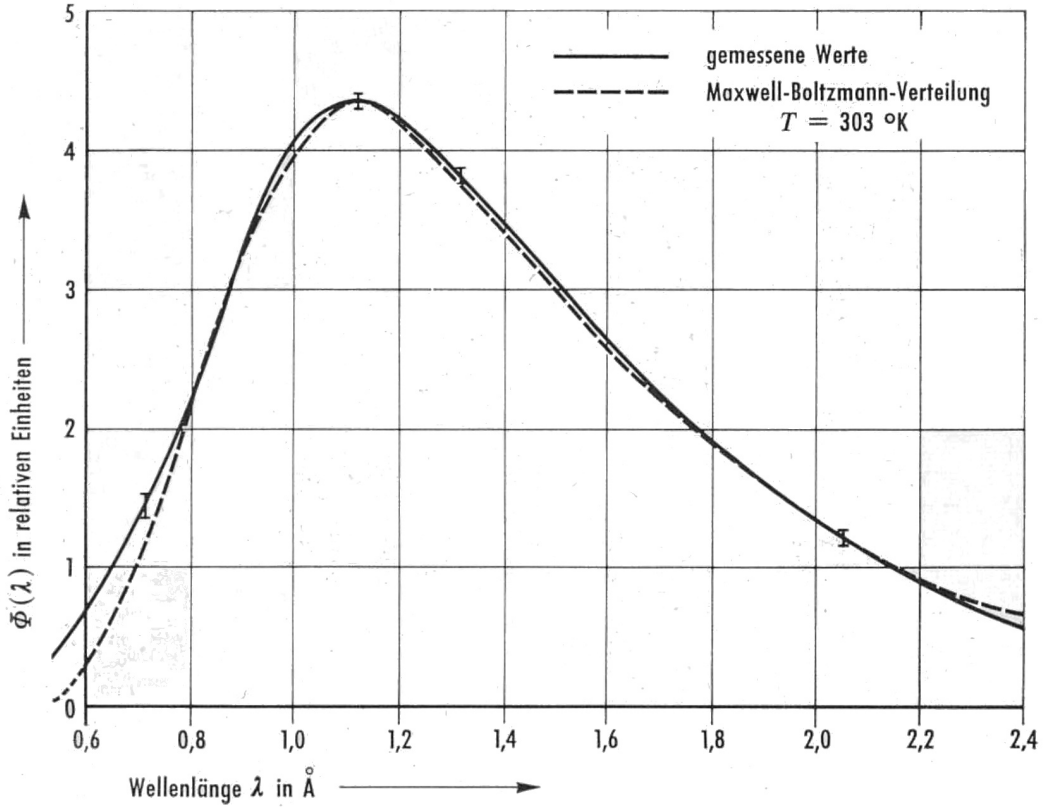
Fig. 2.4.: The measured neutron flux spectrum of the neutron beam in beam tube B is Maxwell-Boltzmann distributed in the thermal energy regime [39].

Thus, the whole neutron flux spectrum Φ_{TRIGA} in beamtube B of the TRIGA reactor is represented by a sum of Eqs. (2.7), (2.8), and (2.9):

$$\Phi_{\text{TRIGA}}(E) = C\left(\Phi_{therm} + f_{therm,epi}\Phi_{epi} + \Phi_{fast}\right), \qquad (2.11)$$

where Eq. (2.8) is weighted with the transition function (2.10) and C is a normalization constant.

The neutron flux spectrum of the TRIGA reactor in Vienna is well known. The thermal neutron flux spectrum was measured with a crystal spectrometer in 1965 by Rauch. As expected the spectrum is in good agreement with a Maxwell-Boltzmann spectrum, see Fig. 2.4 [39].

Simulations in MCNP6 of the whole reactor core have shown also that the neutron flux spectrum in beamtube B behaves as expected [42–44]. This simulation model has been benchmarked with metal foil activation measurements both inside the core and inside of beamtube B. This combination of measurement and simulation provides the neutron spectrum in beamtube B (see Fig. 2.5). Fitting the model mentioned above generates an analytic function of the expected neutron flux in beamtube B of the TRIGA reactor.

The fitting parameters of Eqs. (2.7), (2.8) and (2.9) are provided in Tab. 2.3. While C_1, C_2, are C_3 are normalization constants, α depends on the moderator size and material. For an ideal (thus, infinitely thick and non-absorbing) moderator, α
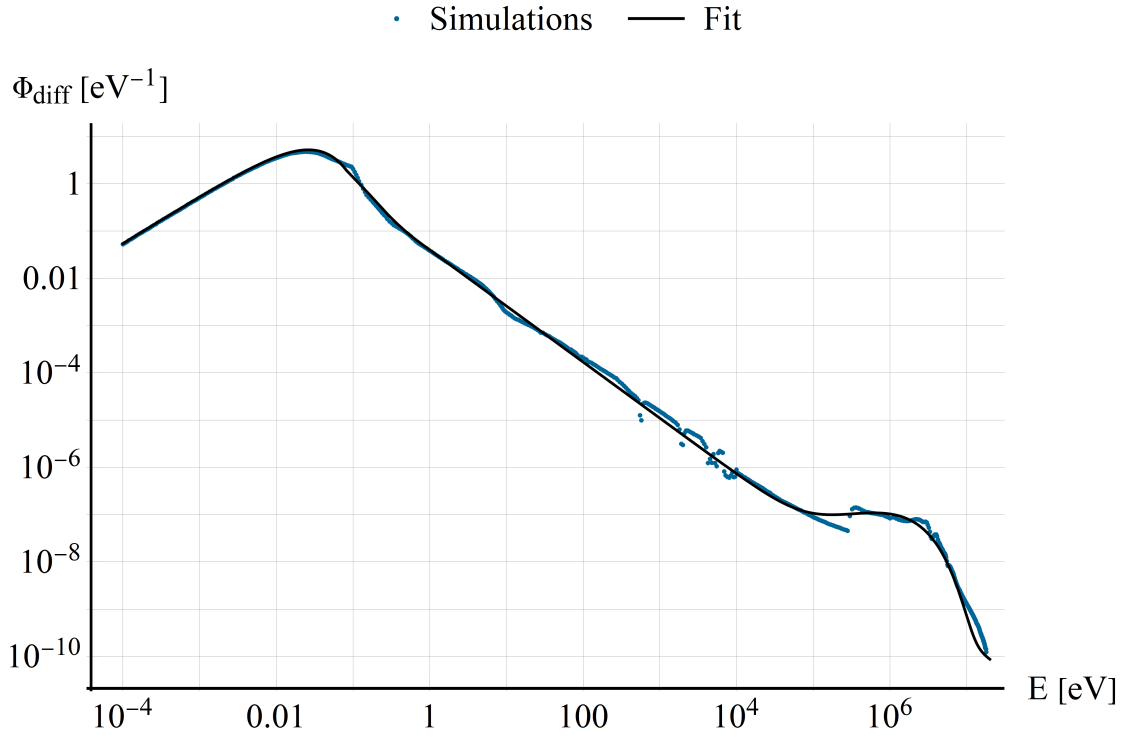
Fig. 2.5.: The simulated differential neutron flux spectrum (normalized to 1) in beamtube B [42] (dots) and the corresponding fitted spectrum model.

fit parameter	value	rel. error
C_1	0.46	0.02
C_2	0.040	0.03
C_3	5.17×10^{-11}	0.03
α	1.100	0.003

Tab. 2.3.: Fit parameters of for the neutron flux spectrum in beamtube B.

would be exactly 1.

With this analytic spectrum simulations can be done to calculate the impact of the installed neutron filters, as will be shown in Section 2.6. Furthermore, it will allow to simulate the radiation absorption properties of the chamber, as will be described in Chapter 3.

2.2.1. Flux measurements

Measurements inside of beamtube B were performed [45] to verify the theoretically modeled spectrum in Eq. (2.11) but also to determine the neutron flux inside of beamtube B. This is important for simulating the ambient dose rate via MCNP6. The neutron flux was measured on three positions in beamtube B by activating gold foils. The results are compiled in Tab. 2.4.

	total flux	thermal flux	epithermal flux	fast flux
1	$(5.73 \pm 0.50)10^{11}$	$(3.28 \pm 0.30)10^{11}$	$(1.73 \pm 0.15)10^{11}$	$(7.28 \pm 0.70)10^{10}$
2	$(3.13 \pm 0.30)10^9$	$(1.40 \pm 0.10)10^9$	$(7.11 \pm 0.70)10^8$	$(1.02 \pm 0.10)10^9$
3	$(6.04 \pm 0.60)10^8$	$(3.39 \pm 0.30)10^8$	$(2.22 \pm 0.20)10^8$	$(4.43 \pm 0.40)10^7$

Tab. 2.4.: Total, thermal ($E < 0.55\,\text{eV}$), epithermal ($0.55\,\text{eV} < E < 100\,\text{keV}$), and fast ($E > 100\,\text{keV}$) neutron flux measured by Au-foil activation. The positions are $5\,\text{cm}$, $125\,\text{cm}$ and $185\,\text{cm}$ away from the reflector in beamtube B [42].

2.3. Theory on filters

In 1959 Brockhouse described a new type of filter which preferentially transmits neutrons of low energy, and which can thus be used to produce beams of thermal neutrons which are mostly free from fast neutrons [46]. The total cross section for thermal neutrons can be much smaller for bound atoms than for single atoms or an ensemble of free atoms owing to solid-state effects. When the energy of the neutron is in the range of the binding energy of the atoms (in the low eV-range) the neutron gets more and more insensitive to solid state effects. The total cross section converges to the cross section of the free atom for high energies, see Fig. 2.6. This effect can be used to filter out epithermal and fast neutrons.

2.3.1. Neutron scattering cross sections

Gurevich [48] defines an *incoherent scattering* process as a process in which the change of the state of the scatterer is not collective but individual as the scattering may occur in a particular scattering center. On the other hand, *coherent scattering* occurs, when the particular scattering center cannot be identified, since the scattering takes place on a whole set of nuclei. "In the case of coherent scattering, one must add the amplitudes of waves scattered by different centers. As a result of interference, a single wave is produced with resultant amplitude due to scattering by the set of particles as a whole. The square of this resultant amplitude determines the coherent component σ_{coh} of the scattering cross section σ_{scatt}. In the case of incoherent scattering, one must add the squares of the amplitudes of the individual scattered waves, and therefore, the incoherent scattering cross section σ_{inc} is simply the sum of the cross sections of the individual centers" [48]. This leads to

$$\sigma_{coh} \sim \left| \sum_i^N a_i e^{iqr_i} \right|^2 \sim N^2 \sigma(q)$$

$$\sigma_{inc} \sim \left(\sum_i^N a_{i,inc}^2 \right) \sim N\sigma_{inc}$$

Furthermore, in an *elastic scattering* process, the total kinetic energy of neutron and nucleus stays the same but a change in the energy of the neutron in the
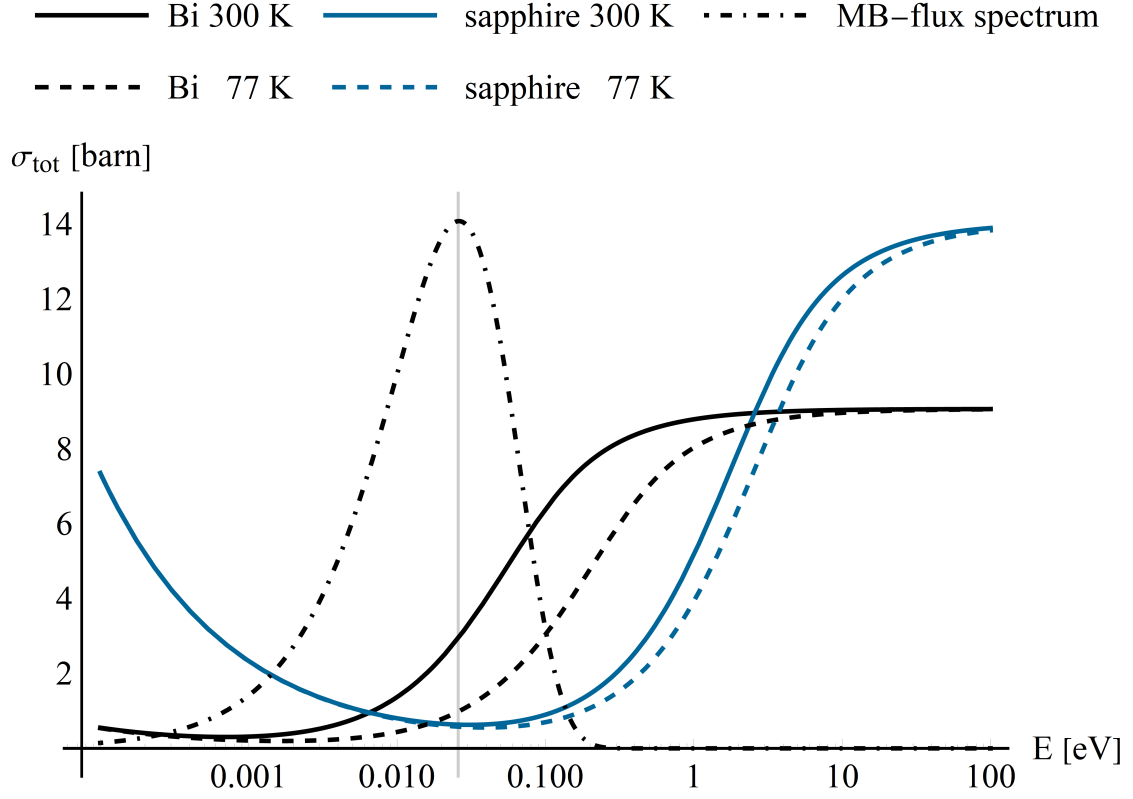
Fig. 2.6.: Energy dependence of the total cross section σ_{tot} of single-crystalline bismuth and sapphire at two different temperatures calculated by using Eq. (2.14). For the calculation σ_{free} is taken from [47]. A Maxwell-Boltzmann flux-spectrum (dash-dotted line) for neutrons with a moderator temperature of 300 K is plotted for comparison.

laboratory system might occur [48]. Therefore, the total cross section for neutrons of matter basically is the sum of [49]:

$$\sigma_{tot} = \sigma_{scatt} + \sigma_{abs}$$
$$\sigma_{scatt} = \sigma_{coh} + \sigma_{inc}$$
$$\sigma_{coh} = \sigma_{coh}^{el} + \sigma_{coh}^{inel}$$
$$\sigma_{inc} = \sigma_{inc}^{el} + \sigma_{inc}^{inel}.$$

While the coherent terms σ_{coh} are more sensitive to the structure of the target, the atomic dynamics in the target are more important for the inelastic[2] terms σ_{inel}:

elastic coherent scattering σ_{coh}^{el} - also known as Laue-Bragg scattering. Scattering on a periodic scattering potential.
inelastic coherent scattering σ_{coh}^{inel} - neutron scattering on phonons as collective motion of the crystal and creation or annihilation of them.

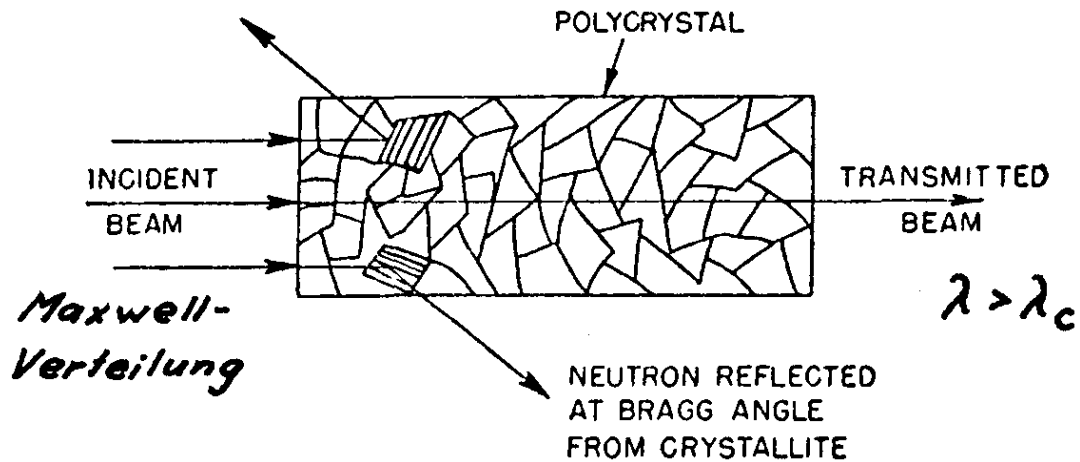[2] also known as thermal diffuse scattering σ_{td}

Fig. 2.7.: Laue-Bragg scattering of thermal neutrons in poly crystalline matter. [51]

elastic incoherent scattering σ^{el}_{inc} - caused by the statistical fluctuations of a periodic scattering potential due to different isotopes and/or spin orientations.

inelastic incoherent scattering σ^{inel}_{inc} - interaction of the neutron with one single nucleus (therefore incoherent) at different times and different positions, thus providing information about diffusion processes or thermal movements of the nuclei [50].

While incoherent scattering is independent from the crystal properties, elastic coherent scattering and inelastic coherent scattering are not. Therefore, these two properties as well as the neutron absorption strongly define the filter characteristics.

Crystals with low neutron absorption and incoherent scattering are well suited as filters since the total cross section in the thermal regime basically is the sum of elastic coherent and inelastic scattering.

Since the 1950ies, several materials like Al_2O_3 (sapphire), MgO, Be, Bi, Pb, CaO, BeO, SiO_2, or graphite have been tested on their filter properties.

2.3.2. Elastic coherent scattering

Elastic coherent scattering (also known as Laue-Bragg-scattering) occurs, when the Bragg-equation is fulfilled

$$n\lambda = 2d_{hkl}\sin\theta, \tag{2.12}$$

where λ is the neutron wavelength, d_{hkl} is the distance between the lattice planes and θ is the scattering angle of the neutron. Since $\sin\theta$ cannot exceed 1, the Bragg scattering cannot occur for wavelengths larger than the Bragg-cutoff-wavelength

$$\lambda_c = 2d_{hkl,max}.$$

Nevertheless, for polycrystalline materials at least one lattice plane can be found for $\lambda < \lambda_c$ to fulfill the Bragg-equation (2.12), see Fig. 2.7. This Bragg-cutoff-wavelength is specific for different materials and is somewhere between 3 Å and 7 Å

[51]. Polycrystalline materials such as beryllium are therefore well-suited as filters for cold neutron beams.

An ideal filter for filtering out epithermal and fast neutrons needs to be a single crystal. In single crystals thermal neutrons get hardly scattered out of the beam due to the fact that there are only few lattice planes which fulfill the Bragg-Eq. (2.12). Not every material can be grown as a single crystal of good quality and reasonable size and sold to a reasonable price since crystal growing is a quite sophisticated science.

2.3.3. Inelastic scattering of thermal neutrons

In the thermal regime, usually the inelastic cross section σ_{inel} is small compared to the elastic coherent cross section. In the static incoherent approximation it is [52]:

$$\sigma_{inel}(\lambda) = \sigma_{free} \left\{ 1 - \frac{\lambda^2}{2B} \left(1 - e^{-\frac{2B}{\lambda^2}} \right) \right\}. \tag{2.13}$$

Rewriting Eq. (2.13) as a function of energy by using

$$\lambda = \sqrt{\frac{h^2}{2m_n E}} \quad :$$

$$\sigma_{inel}(E) = \sigma_{free} \left\{ 1 - \frac{h^2}{4EBm_n} \left(1 - e^{-\frac{4EBm_n}{h^2}} \right) \right\} \tag{2.14}$$

where σ_{free} is the scattering cross section of the free atom and the factor B is defined as

$$B = \frac{6h^2}{mk_B\Theta} \left(\frac{1}{4} + \left(\frac{T}{\Theta}\right)^2 \int_0^{\frac{\Theta}{T}} \frac{x\,dx}{e^x - 1} \right) \tag{2.15}$$

where h is the Planck constant, k_B the Boltzmann constant, m is the mass of the nucleus, T is the temperature, and Θ the Debye temperature of the crystal. B is well known as part of the Debye-Waller factor

$$\exp\left(-\frac{2B\sin\theta}{\lambda} \right)^2.$$

Eq. (2.14) shows in combination with Eq. (2.15) that σ_{inel} depends on the filter temperature T, the Debye-temperature Θ, and the neutron energy E. For higher energies σ_{inel} converges towards σ_{free}, and in the static incoherent approximation it converges towards 0 for lower energies where it is dominated by the absorption cross section σ_{abs}, which was shown already in Fig. 2.6. Furthermore, the these equations reveal the following important effects:

- Cooling down neutron filters improves their behavior, especially when materials with a low Debye-temperature Θ are used.
- The higher the Debye-temperature Θ the higher the filter quality, since the ratio of the scattering cross section in the epithermal and fast region to the cross section in the thermal region gets higher.

2.3.4. Elastic scattering of fast neutrons

For crystal filter materials the total cross section in the thermal energy regime apart from a Bragg reflection is dominated by the inelastic cross section σ_{inel}. In the static incoherent approximation used in Eq. (2.14) it converges to σ_{free} for energies between about $1\,eV$ and $1\,keV$. However, this approximation no longer holds for higher energies, since there two effects have to be taken into account which are neglected in this approximation:

- forward scattering of fast neutrons
- for higher energies, the total cross section is dominated by the elastic scattering cross section σ_{el} which is not constant, however, above about $1\,keV$
- for even higher energies (more than $10\,MeV$) elastic scattering can be neglected and the total scattering cross section is dominated by inelastic scattering, i.e. $\sigma_{scatt} \approx \sigma_{inel}$.

Since MCNP is not capable of simulating the solid-state physics effects in the thermal energy region, these effects have to be taken into account explicitly when modeling the neutron spectrum behind the filter.

Elastic scattering cross section

The behavior of σ_{el} strongly depends on the isotope and can have a quite complicated shape caused by resonances above $1\,keV$, as it is shown in Fig. 2.8. This is important if neutrons with such energies need to be filtered, as is the case in our project, since the direct view to the reactor core leads to a significant amount of fission neutrons of ^{235}U with an energy distribution well up in the MeV range.

This effect leads to a worse filter efficiency of sapphire for fission neutrons because the elastic scattering cross section σ_{el} of oxygen drops tremendously in the MeV-regime, as can be seen from Fig. 2.8. Fortunately, σ_{el} is well known and can be found in databases on neutron-induced reactions, like the ENDF database [47].

Fast neutron forward scattering

Not only the elastic scattering cross section is downgrading the filter efficiency for fast neutrons but also the fact that they are not scattered isotropically in the laboratory system like slow neutrons scattered by single nuclei, which is shown in Fig. 2.9. In fact, fast neutrons tend to be scattered in forward direction. Therefore, less neutrons get scattered out of the neutron beam by the filter. This raises the fraction of fast neutrons in the beam and thus the total dose rate and background. Obviously the magnitude of this effect strongly depends on the solid angle of the beamtube where the filter is installed.

The double differential cross sections $\frac{d\sigma}{d\Omega}$ of O, Al and Bi are well known and these data are accessible over databases on neutron-induced reactions, like the ENDF database [47]. By using these data scattering cross sections can be calculated which consider narrow-angle-scattering of fast neutrons.
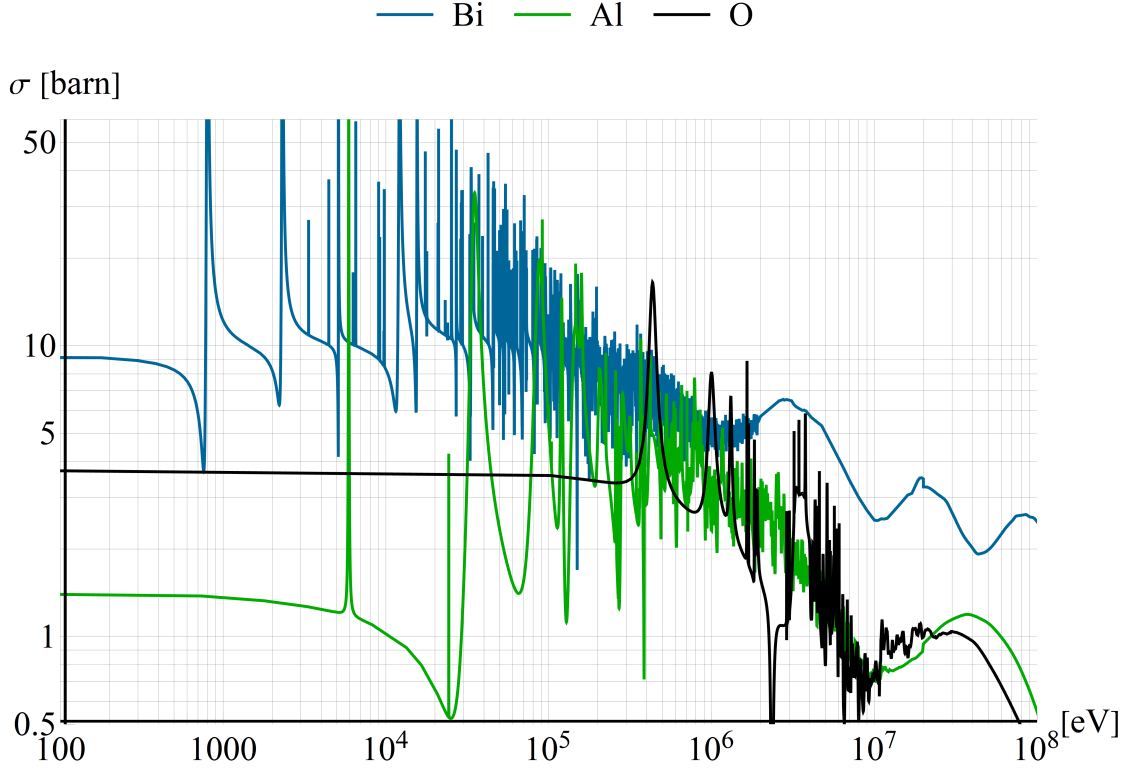
Fig. 2.8.: Elastic scattering cross section σ_{el} of oxygen, aluminium and bismuth, the three components of the filter set. In the crucial energy range of $1\,\mathrm{MeV}$ to $10\,\mathrm{MeV}$ the scattering cross section of oxygen is much smaller than in the epithermal energy regime. This leads to a poor filter effect. For low energies σ_{el} converges to σ_{free}.

The microscopic scattering cross section per atom $\sigma_{i,scatt}$ is the integral of the angle-dependent double differential cross section over 4π solid angle:

$$\sigma_{i,scatt} = \int_0^{4\pi} \frac{d\sigma}{d\Omega} d\Omega.$$

In our case, neutrons scattered in a grazing angle do not leave the beam since both the apertures and the beam diameter have macroscopic dimensions. Therefore they will still be detected together with the direct beam. This leads to a modified scattering cross section for our specific beam geometry

$$\sigma_{scatt} = \int_A^{4\pi} \frac{d\sigma}{d\Omega} d\Omega \tag{2.16}$$

with the solid angle

$$A = 2\pi[1 - \cos(\frac{\alpha}{2})] \ ,$$

where α is the critical angle a neutron must be scattered for leaving the direct beam. α is defined by the beamtube geometry and its divergence. For this setup it was defined to be $\alpha = 10°$. This angle is defined by the apertures in the beamtube. Since there are further apertures afterwards (such as the shutter block of the
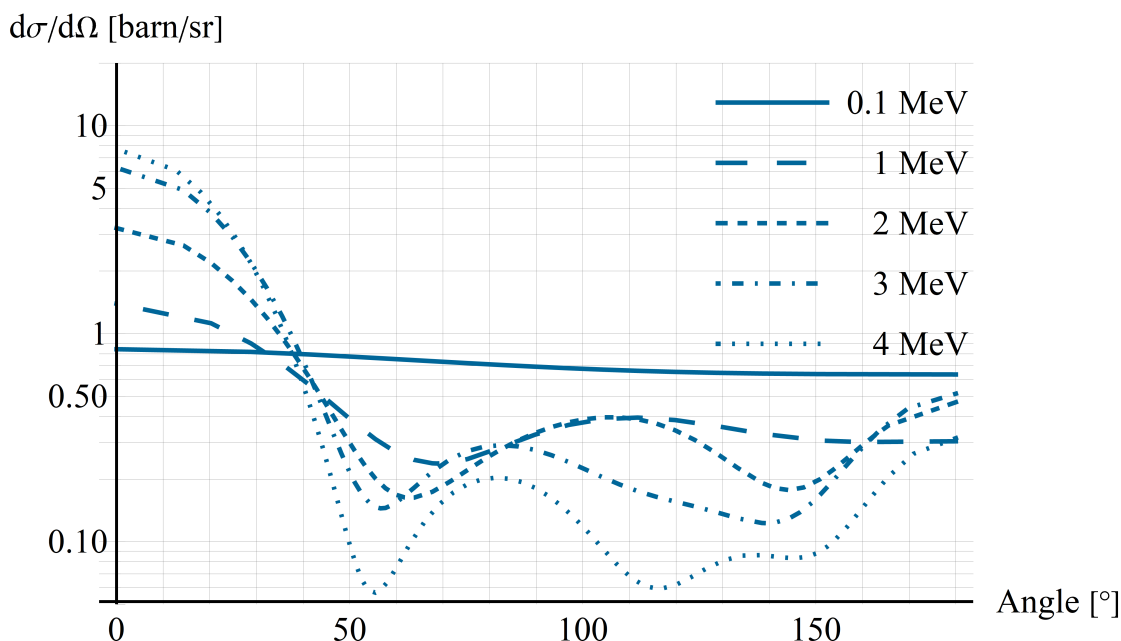
dσ/dΩ [barn/sr]

Fig. 2.9.: The double-differential elastic scattering cross section of ^{209}Bi. While 0.1 MeV neutrons are scattered almost isotropically, for higher energies more neutrons get scattered in the forward direction and remain within the beam.

beamstop or the beamport wall), most of these neutrons are absorbed in the shutter block installed after the end of the beamtube.

The energy dependent relative amount of neutrons scattered in a narrow solid angle A can be calculated easily as

$$\epsilon(E) = \frac{\int_0^A \frac{d\sigma(E)}{d\Omega} d\Omega}{\int_0^{4\pi} \frac{d\sigma(E)}{d\Omega} d\Omega} \ .$$

In Fig. 2.10 $\epsilon(E)$ is plotted for the three filter elements O, Al and Bi. Since thermal neutrons are scattered isotropically in all directions, for low energies $\epsilon(E)$ must converge to the fraction of the solid angle which is 0.0019 for $\alpha = 10°$. Moreover, the mass-dependence of the effect can be seen, since the it is higher for heavier nuclei.

2.3.5. Neutron absorption cross section

Every known isotope except ^4He has got a non-zero neutron absorption cross section σ_{abs} which can vary tremendously from isotope to isotope. More than that, the absorption cross section is energy dependent: While there can be resonance peaks or cutoffs in the epithermal and fast region, at low energies $\sigma_{abs}(E)$ exhibits a pure $1/v$- or $1/\sqrt{E}$-dependency, respectively, as it can be seen from Fig. 2.11. This means, that σ_{abs} may become appreciable in the thermal energy region. Therefore,
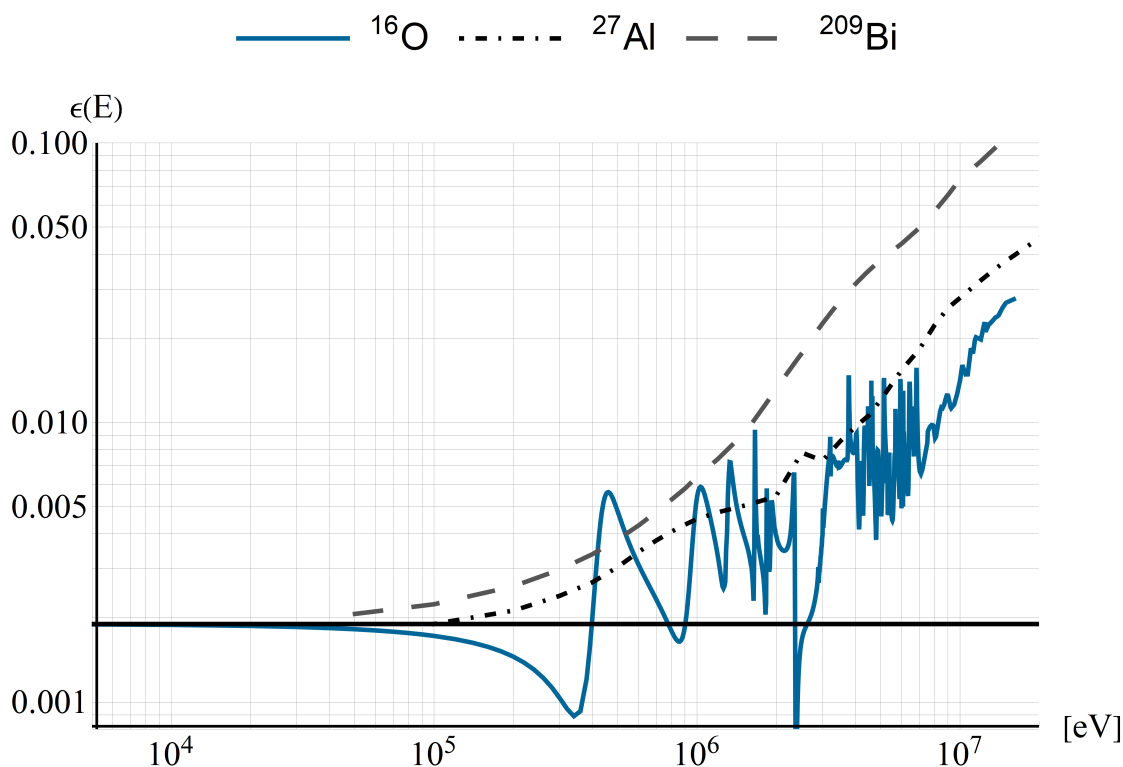
Fig. 2.10.: The relative amount of neutrons scattered in forward direction with an angle less than $\alpha = 10°$ for the filter elements. The horizontal line marks the fraction of a solid angle corresponding to $\alpha = 10°$ divided by 4π which is the low energy limit.

only elements with very low absorption cross section can be used as filter material, such as Be, C, O, Mg, Al, Si, Pb, Bi.

2.3.6. Gamma absorption

Since beamtube B has got a direct view to the core, a high amount of unwanted γ-radiation can be expected in the beam. As it is written in [53] the photons of the γ-radiation basically interact with matter by the following three effects:

Photo effect - Photons interact with the electrons of the atom. The photon gets absorbed, the electron emitted. The void gets filled by an other electron which emits X-ray radiation, or alternatively an Auger electron is emitted.

Compton scattering - Photons are scattered by an electron of the atom and lose energy.

Pair production - The photon can interact with the electric field of the nucleus or of a free electron for electron-positron production, this effect has a threshold energy E_{thresh}:

$$\gamma + Zp \rightarrow Zp + \left(e^+ + e^-\right), \qquad E_{thresh} = 1.022 \, \text{MeV}$$

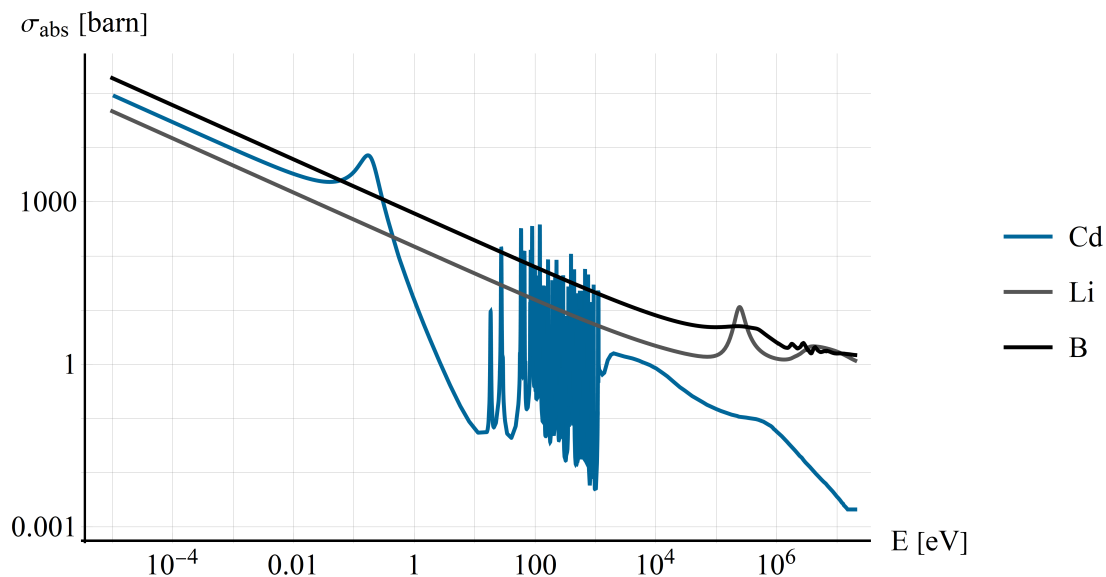$$\gamma + e^- \rightarrow e^- + \left(e^+ + e^-\right), \qquad E_{thresh} = 2.044 \, \text{MeV}$$

Fig. 2.11.: The absorption cross section σ_{abs} of natural cadmium, ^6Li and ^{10}B as a function of the neutron energy. These three materials are often used as neutron absorbers.

The cross sections σ_{Photo}, $\sigma_{Compton}$ and σ_{Pair} of the three effects have a more or less complicated dependency on the γ energy E and the atomic number Z, as shown in [53] for more details.

Process	E_γ	Z
Photoeffect	E^{-3}	Z^4
Compton scattering	E^{-1}	Z
Pair-production	$\ln(E)$	Z^2

Tab. 2.5.: The dependency of the three different effects on the photon energy E_γ and atomic number Z [53].

If a collimated beam with n_0 photons per second passes a thin foil with the thickness dx, dn photons get absorbed:

$$-\frac{dn}{n_0} = \mu dx$$

with

$$\mu = N \left(\sigma_{Photo} + \sigma_{Compton} + \sigma_{Pair} \right)$$

where N is the number of atoms per cm^3. μ is the linear attenuation factor and $\frac{\mu}{\rho}$ the mass attenuation factor, see Fig. 2.12.

In summary, for effectively shielding γ-radiation a high atomic number Z is beneficial, as which follows from Tab. 2.5, but also a high density ρ of the material is crucial to increase the total amount of nuclei and electrons in the shielding material. Therefore, lead, bismuth, iron, or uranium are an excellent choice for γ-shielding.
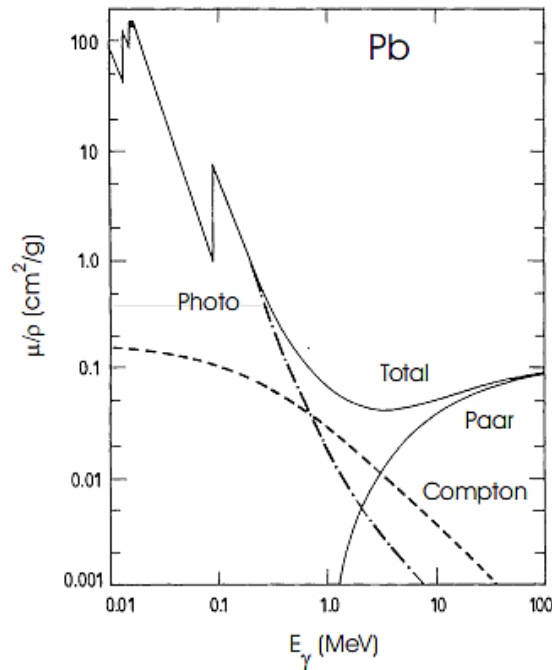
Fig. 2.12.: The mass attenuation coefficients μ_{photo}, $\mu_{Compton}$, μ_{pair}, and μ_{total} for lead [53].

2.4. Filter materials

Epithermal and fast neutrons are an unwanted ambient dose rate source. They can be filtered out of a thermal white neutron beam by using the energy dependence of inelastic scattering) as described previously (see Eq. (2.14). Thus, the following characteristics are crucial for a good thermal neutron filter:

High Debye-temperature - for a high scattering cross section ratio of the epithermal and fast energy region to the thermal energy region and therefore a steep filtering function.

Single crystal - to minimize the Bragg scattering of thermal neutrons.

Low absorption cross section - to minimize the absorption of neutrons in the thermal and sub-thermal energy range.

Cooling of the filter - improves the filter function. This is more important for filters with a low Debye-temperature Θ.

If the neutron beam is polluted with γ-radiation, the following characteristic of the filter is also of crucial importance:

High density - of the material to filter out γ-radiation

Considering the characteristics of good filters mentioned above, a lot of effort was put in this topic in the last decades to find the ideal combination of neutron filter material. While polycrystalline materials can be used when the filter is installed very close to the reactor core, filters which are installed within the beamtube at a distance to the core have to be single crystal materials [54].

	ρ [g cm^{-3}]	Θ [K]	σ_{abs} [barn]
Pb	11.34	87	0.171
Bi	9.78	116	0.034

Tab. 2.6.: Physical properties of lead and bismuth.

Quite a series of single crystals grown from Bi, Si, SiO$_2$, Al$_2$O$_3$, Pb, PbF$_2$, MgO, [55], or MgF have been investigated for this purpose [56]. A good overview of this topic is given by Mildner [57]. Taking the availability of single crystals at reasonable size and acceptable prices into account, sapphire is an excellent choice as filter material for thermal neutrons [57, 58].

2.4.1. Chosen filter materials

The *Thermal White Neutron Beam* facility is equipped with a combination of two different neutron filters: a 5 cm and a 10 cm bismuth filter and a 15 cm sapphire filter were available, therefore it was possible to change flux, flux spectrum and γ-radiation background by mounting different filter sets (in this thesis, these filter sets are called '15/0', '15/5', '15/10' and '15/15', where the first number indicates the length of the sapphire and the second that of the bismuth filter).

For filtering out epithermal and fast neutrons sapphire is currently the best choice because the effect on flux and flux spectrum is only small in the thermal regime but the effect on the fast neutron background is very large which can be seen by comparing the TRIGA flux spectrum with the 15/0 flux spectrum in Fig. 2.16. Therefore, it might be installed for all future experiments. While its components aluminum and oxygen have a reasonable low absorption cross section, its Debye-temperature of $\Theta = 1047$ K is one the highest of single crystals, except e.g. diamond ($\Theta = 1860$ K). Furthermore, sapphire ingots can be produced in large sizes with very few crystallographic defects, since the ingot growing process can be controlled very well. Sapphire is also demanded by industry leading to several producers and reasonable prices[3]. On the downside, the density of sapphire is only around 4 g cm^{-3} leading to poor γ absorption. Even more, due to neutron absorption, the aluminum in sapphire is a source of γ-radiation.[4]

A high quality mosaic single crystal of bismuth was chosen to act as γ-radiation filter since the density of bismuth is about as high as the density of lead, but the neutron absorption cross section σ_{abs} is much lower, the Debye temperature Θ is higher and the quality of the crystal is much better: While bismuth is an excellent choice for filtering γ-radiation, its abilities for filtering neutrons are only mediocre due to the quite low Debye temperature, see Figs. 2.6 and 2.13. The thermal neutron flux and the flux spectrum depend stronger on the bismuth filter length, which can be seen by comparing the 15/0 flux spectrum with the 15/15 flux spectrum in Fig. 2.16. Therefore, the bought bismuth filter[5] was cut in two

---

[3]The price of the used sapphire was about 25000 € for a cylinder with 10 cm diameter and 15 cm length of the quality class 'HEMLUX' where some light scatterers are allowed.

[4]Thus, the sapphire filter always needs to be closer to the core than the bismuth filter.

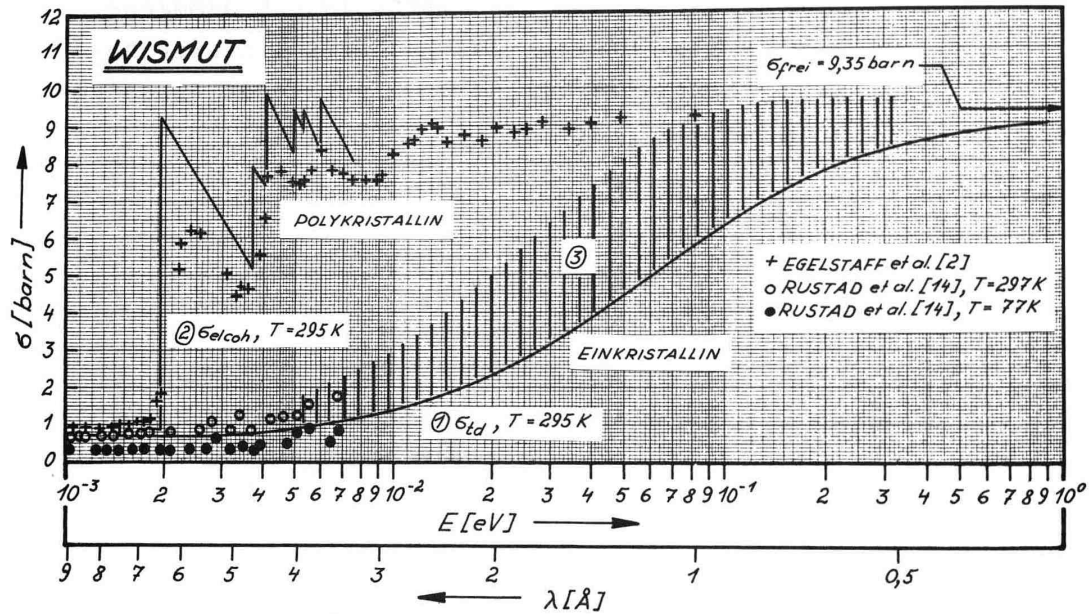[5]The price of the single crystal bismuth cylinder with 10 cm diameter and 15 cm length which is

Fig. 2.13.: Total cross section of bismuth [51]:

+: total cross section of polycrystaline Bi (300 K), measured

o: total cross section of single crystal Bi (297 K), measured

•: total cross section of single crystal Bi (70 K), measured

1: thermal diffuse cross section (300 K), calculated.

2: elastic coherent cross section for polycrystaline Bi, calculated.

3: The high mosaicity of single crystal Bi leads to broad maxima in the thermal regime due to Laue-Bragg-scattering. The average cross section is somewhere in the shaded area.

parts: one cylinder with 5 cm and one with 10 cm length. Thus, it is possible to match the filter length of the bismuth crystal and therefore the thermal neutron flux and the amount of γ-ray pollution in it according to the requirements of the actual experiment that is installed within the shielding chamber of the *Thermal White Neutron Beam* facility. Future experimentalists have to trade-off thermal neutron flux against γ-radiation background by choosing the best filter set for their experiment. Bismuth crystals are not very common and therefore quite expensive. Producing a bismuth crystal is quite challenging because among other things bismuth has got a negative thermal expansion coefficient.

Finally, it must be mentioned that many publications only focus on the thermal region of the filter transmission. Thus, it is necessary to emphasize the fact that estimating the filter transmission function by just using the static incoherent approximation of the scattering cross section leads to a tremendously wrong estimation of the neutron flux in the fast region. Especially when fission neutrons need to be filtered out, this is crucial. Only using the static incoherent approximation underestimates the fast neutron flux by a factor of >10 (see Tab. 2.7), leading to a much higher dose rate.

---

orientated randomly, was about 30000 €

2.5. Filter transmission

The energy dependent transmission function $T(d, E)$ of the filter can be defined as

$$T(d, E) = \frac{\Phi(d, E)}{\Phi(0, E)}$$

where $\Phi(0, E)$ is the incoming spectrum, $\Phi(d, E)$ the spectrum after the filter, and d the filter thickness.

Knowing the transmission function of a filter and the incoming spectrum $\Phi(0, E)$, the outgoing spectrum is

$$\Phi(d, E) = \Phi(0, E)\, T(d, E). \tag{2.17}$$

Since the used neutron beam is well collimated, $\Phi(d, E)$ can be calculated by assuming a simple exponential relation

$$\Phi(d, E) = \Phi(d, 0)\, e^{-\Sigma(E)d} \ .$$

Thus,

$$T(d, E) = e^{-\Sigma(E)d} \tag{2.18}$$

with

$$\Sigma(E) = \sigma(E)\frac{N_A \rho}{A_\mu} \ , \tag{2.19}$$

where N_A is the Avogadro constant, ρ the filter material density, A_μ the atomic mass, and $\Sigma(E)$ the total macroscopic cross section.

2.5.1. Total cross section composition

Adapting the upper equations for our filter set of two different materials (sapphire and bismuth) and for a total macroscopic scattering cross section Σ_{WB} which describes all effects occurring in the filter, the filter transmission function for the white beam can be defined as

$$T_{WB}(E) = e^{-\Sigma_{WB}(E)d_{Filter}} \tag{2.20}$$

with

$$\Sigma_{WB}(E) = \left(\sigma_{Sa}(E)\frac{\rho_{Sa}d_{Sa}}{A_{Sa}d_{Filter}} + \sigma_{Bi}(E)\frac{\rho_{Bi}d_{Bi}}{A_{Bi}d_{Filter}} \right) N_A \ ,$$

where d_{Sa} and d_{Bi} are the lengths of the sapphire and bismuth filter, respectively, and $d_{Filter} = d_{Sa} + d_{Bi}$ is the total filter assembly length. $\sigma_{Sa/Bi}(E)$ must consider

- the solid state physics effects in the thermal region,
- the deviation of the elastic scattering cross section σ_{el} from the free scattering cross section σ_{free} (see Fig. 2.8), and
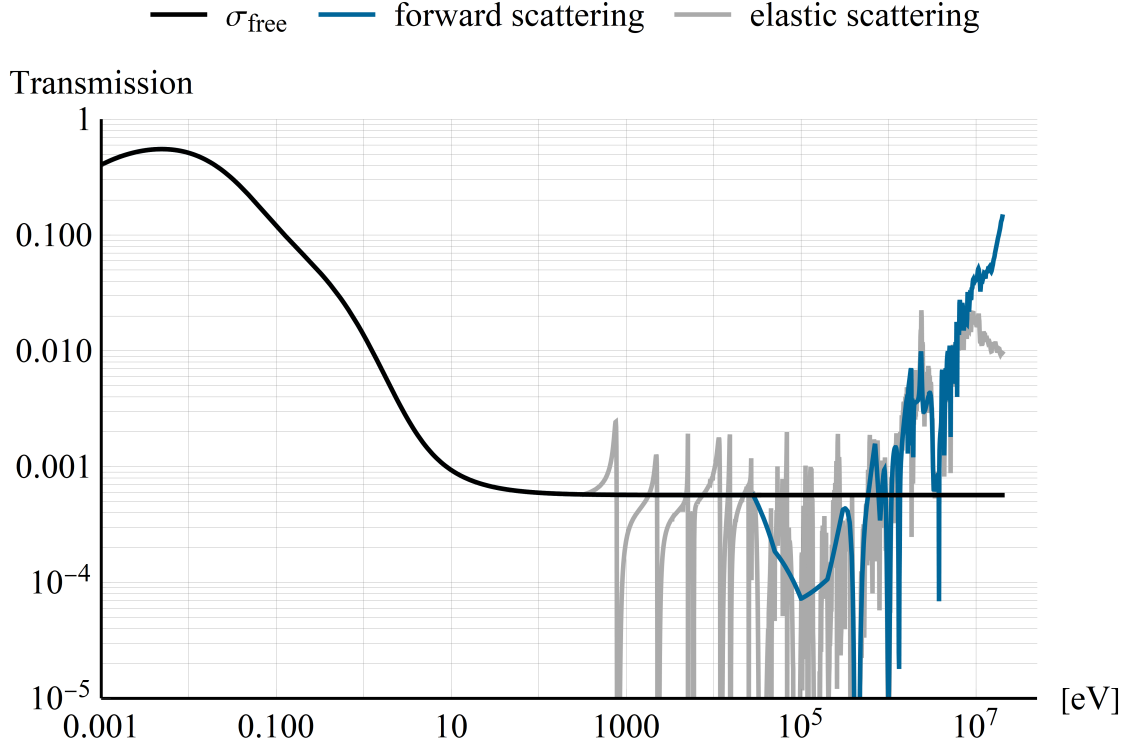- the effect of forward scattering (see Figs. 2.9 and 2.10).

Fig. 2.14.: Transmission function of the filter set consisting of a sapphire
(d_{Sa} =15 cm) and a bismuth (d_{Bi} =10 cm) single crystals for three
different approximations of the high energetic part of the function:
σ_{free} only uses the constant scattering cross section of the free nucleus,
'forward scattering' considers the anisotropic scattering of fast neut-
rons, and 'elastic scattering' only considers the elastic scattering cross
section.

Therefore, in the thermal and epithermal area $\sigma_{Sa/Bi}(E)$ need to be composed
of the respective inelastic cross sections σ_{inel} and the absorption cross sections
σ_{abs} (see Eq. (2.14) and Fig. 2.6). In the fast energy regime $\sigma_{Sa/Bi}(E)$ are just the
respective elastic cross sections σ_{el}, corrected by the increase of the fast neutron
portion due to forward scattering (see Eq. (2.16)):

$$\sigma_{Sa/Bi} = \begin{Bmatrix} \sigma_{inel} + \sigma_{abs} \\ \sigma_{el} \end{Bmatrix} \text{ for } \begin{cases} 0 \leqslant E \leqslant E_{joint} \\ E > E_{joint} \end{cases} \tag{2.21}$$

At E_{joint} the cross sections can be merged, i.e.

$$\sigma_{inel}(E_{joint}) + \sigma_{abs}(E_{joint}) = \sigma_{el}(E_{joint}) \approx \sigma_{free},$$

with $\sigma_{abs}(E_{joint}) \approx 0$. Typical values for E_{joint} are in the range between 10 eV and
1000 eV.

2.5.2. The Filter transmission function

Calculating the total cross section as described above leads to a transmission function (2.20) of the 15/10-filter set that is shown in Fig. 2.14. The three different curves correspond to three different approximations of the high energy part (E>E_{joint}):

- Taking only the static incoherent approximation into account, σ_{tot} converges to σ_{free}.
- Taking the actual elastic scattering cross section σ_{el} into account resonances appear and the worse filtering for fast neutrons gets visible.
- Taking also the effect of forward scattering (for $\alpha = 10°$) of fast neutrons into account shows an even worse filtering function for high energetic neutrons.

Up to about $1000\,\text{eV}$, there is no significant difference between these three approximations. However, at higher energies the difference is crucial.

2.6. The neutron flux spectrum

After deriving a formula for the theoretical flux spectrum of beamtube B and testing it experimentally (as it was described in Chapter 2.2), a filter function $T(d, E)$ was derived in Section 2.3 and 2.5 in order to specify the effect of filtering on the neutron spectrum. Hence, it is possible to calculate the neutron spectrum of the *Thermal White Neutron Beam* Φ_{WB} behind the filter set which is important for the simulations of the complete shielding in Chapter 3, as well as for planning of future experiments.

According to Eqs. (2.11) and (2.17), the neutron flux spectrum Φ_{WB} for the *Thermal White Neutron Beam* can be defined as:

$$\Phi_{WB}(E) = \Phi_{\text{TRIGA}}(E)\, T_{WB}(E), \tag{2.22}$$

where $T_{WB}(E)$ is the transmission function of the set of filters of sapphire and bismuth. Using the three different approximations for the scattering cross sections leads to different transmission functions and hence neutron flux spectra, as can be seen in Fig. 2.15.

The spectral differences also get visible when the relative neutron flux of the three different energy regimes (thermal, epithermal, and fast neutrons) is calculated for the different approximations described above (Tab. 2.7). Likewise from Fig. 2.16 and Tab. 2.8 the different performance of the four available filter configurations can be seen. For these data and plots elastic and forward scattering were taken into account.

In summary, in this chapter the neutron flux spectrum of beamtube B was modeled theoretically and fitted to experimental data. The impact of neutron filters on this modeled flux spectrum was calculated. For this, the elastic scattering but also fast neutrons being scattered in forward direction were taken into account. The calculated flux spectrum $\Phi_{WB}(E)$ (shown in Eq. (2.22)) is the available neutron flux spectrum for future experiments and depends on the used filter sets, as shown

in Tab. 2.8. Having now a possibility to calculate $\Phi_{WB}(E)$ is a huge success and was the declared goal of this chapter. With that important piece of information, it is now possible to use the neutron flux spectrum for shielding simulations, as it will be done in the following chapter.
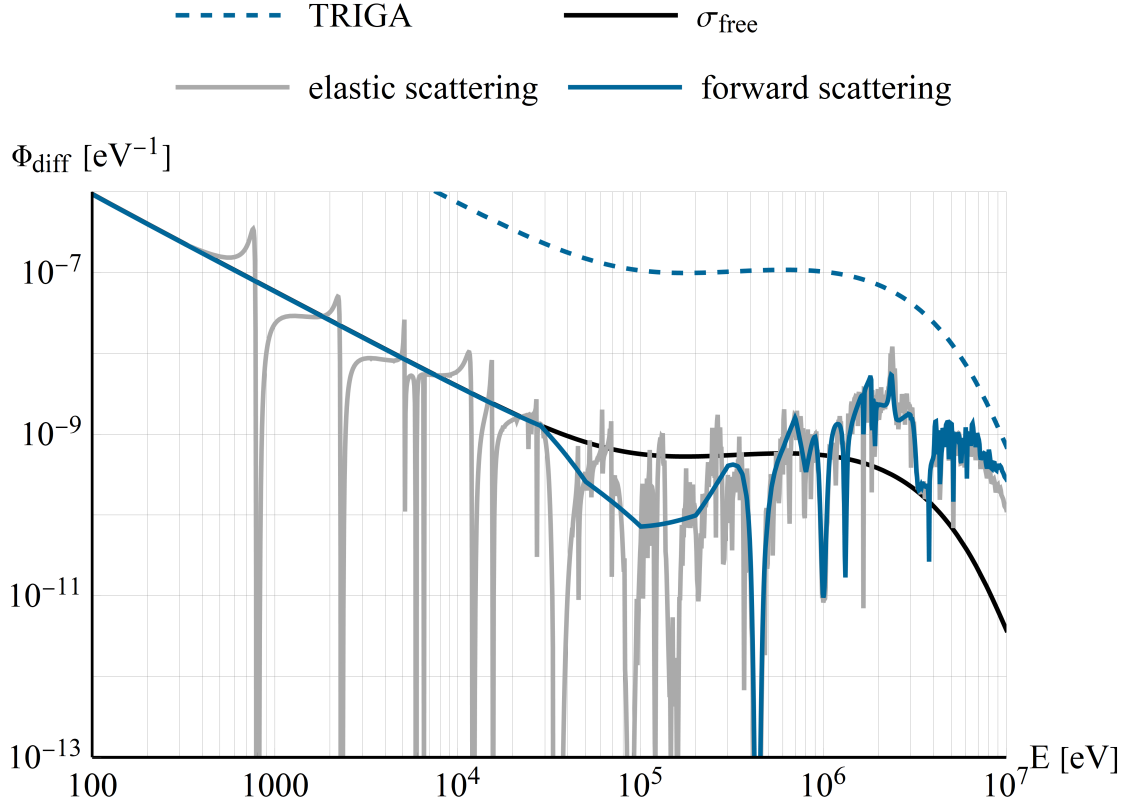

Fig. 2.15.: Calculated differential neutron flux spectra without filters (dashed, normalized to 1), and with filters when only σ_{free} is considered (black), when elastic scattering σ_{el} is considered (gray), and when also forward scattering is taken into account (blue).

	thermal	epithermal	fast
TRIGA spectrum	0.4565	0.2326	0.3107
inc. static approx.	0.9848	0.0135	0.0017
elastic scattering	0.9773	0.0134	0.0093
forward scattering	0.9769	0.0134	0.0097

Tab. 2.7.: Comparison of the three energy regimes of the TRIGA spectrum with three different approximations of the thermal white beam spectrum for the 15/10-sapphire/bismuth single crystal filter set. While the first two approximations underestimate the fast flux, the last one considers also forward scattering of fast neutrons and therefore provides reasonable results in the shielding simulations.
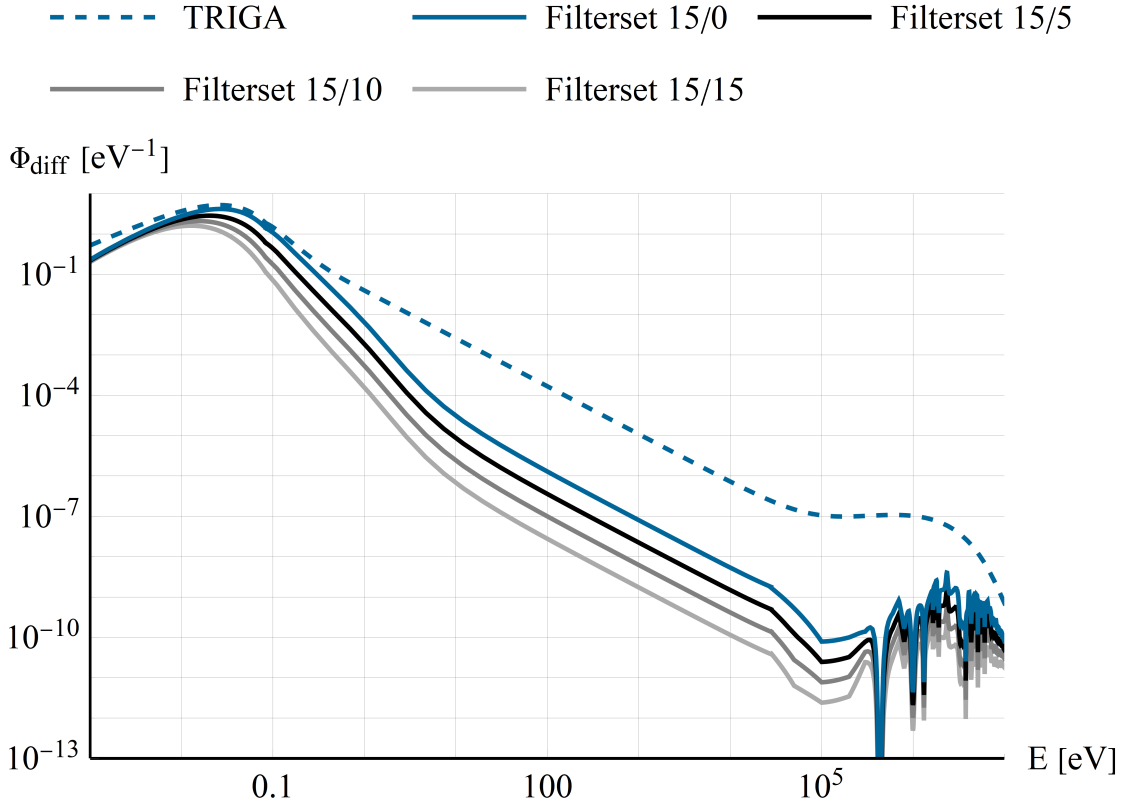
Fig. 2.16.: Calculated differential neutron flux spectra for different filter sets. 15/10 means that a 15 cm thick sapphire crystal and a 10 cm thick bismuth are installed, which is the standard filter set for all measurements in this thesis. The TRIGA flux spectrum is the spectrum without any filters (and normalized to 1), thus the flux spectrum in beamtube B from Section 2.2.

	thermal	epithermal	fast
TRIGA spectrum	0.4565	0.2326	0.3107
15/0	0.9369	0.0463	0.0165
15/5	0.9609	0.0259	0.0126
15/10	0.9766	0.0134	0.0091
15/15	0.9860	0.0064	0.0063

Tab. 2.8.: Comparison of three energy regimes of the different possible filter sets at the instrument. The values represent their relative contributions to the total neutron flux.

3. Shielding and Dose Rate Simulations

Since it is necessary for every neutron instrument to comply with radioprotection requirements, a shielding chamber was designed and built in front of beamtube B of the TRIGA reactor to meet given dose rate limits. Before construction, the design of this shielding was tested by means of computer simulations to see if the given dose rate limits can be met.

Generally speaking, radiation shielding simulations need to consider three different features of the setup:

- Particle beam characteristics: spectrum, flux, divergence, diameter
- Material composition
- Geometry of the shielding components

Clearly, the quality of a simulation depends on the accuracy of the description of these three features. Therefore, the next three sections will describe the way of finding proper approximations of the points mentioned above.

Among experiments and theoretical deductive reasoning, computer simulations have developed in the past decades as an important tool for research in natural science. Monte Carlo Simulation (MCS) is one broad class of techniques for solving problems using random sampling to obtain numerical results instead of solving e.g. differential equations directly. This approach is very efficient for simulating the shielding properties of the new facility. Particle (e.g. neutrons or photons) trajectories are calculated by assuming that the collision of two particles is a stochastic process which can be well approximated by random sampling, a procedure that reduces computing time tremendously. Particle trajectories do not affect each other which makes parallelization of computation much easier.

The design of the shielding was tested with the classified MCNP6 [1] software package developed and maintained by the Los Alamos National Laboratory. It is a standard tool for analyzing the transport of neutrons and photons by the Monte Carlo method. The code deals with transport of neutrons, photons but also e.g. the production and transport of secondary photons resulting from neutron interactions which is important for simulating the new instrument. However, neither a description of Monte Carlo simulations, nor the abilities, strengths and weaknesses and technical details of MCNP6 will be discussed in this thesis but can be found e.g. in [1, 59–61].

3.1. Neutron and gamma spectra

Due to the direct view to the reactor core, **reactor gamma radiation** will contaminated the neutron beam. Therefore, the knowledge of both the intensity and the energy spectrum of the gamma radiation is necessary for a simulation of

the radiation shielding components of the *Thermal White Neutron Beam*. Reactor gamma radiation consists of prompt gamma radiation from the fission process of ^{235}U and of gamma radiation produced from fission products. While the first component can be described by [62]

$$
\hat{N}(E) = \begin{cases}
0 & E < 0.085\,\text{MeV} \\
4.54(E - 0.085)e^{1.648E} & 0.085 \leq E < 0.3\,\text{MeV} \\
3.20e^{-2.3E} & 0.3 \leq E < 1.0\,\text{MeV} \\
0.95e^{-1.1E} & 1.0 \leq E < 8.0\,\text{MeV} \\
0 & E \geq 8.0\,\text{MeV}
\end{cases}
$$

the delayed gamma radiation from the fission products has got a complex shape and is dependent on geometry, type and runtime of the reactor. Measuring a reactor gamma spectrum is quite a complicated task and was never of particular interest in Vienna, therefore just a simple but proper estimation of the spectrum was done, see [59].

On the other hand, the **neutron flux spectrum** of beam tube B is well known, as discussed in section 2.2. The neutron flux spectrum is theoretically well described, it was measured in the 1960ies with a crystal spectrometer [39] and it was remeasured for core simulations in 2014 [42–44].

Since MCNP6 uses a free gas scattering model, where every material is treated as if it was a gas and solid-state effects are therefore neglected, the effects of the filters on the neutron flux spectrum (see Section 2.3) cannot be simulated. Therefore the filtered neutron flux spectra that were used as input for the numerical simulations were calculated theoretically, see Section 2.6 and Fig. 2.16. Afterwards, these spectra were discretized and divided by the bin width, since MCNP6 requires a binwise integral representation of the spectra. The discrete numerical values used as input for MCNP6 are listed in Appendix A.1.

Since the filters do not only change the spectrum but also the total flux, a filter factor $\varphi_{Sa/Bi}$ was introduced to describe this effect (see also Appendix A.1). This factor is just the total integral of Eq. (2.22) and is listed in Tab. 3.1 for the different filter sets:

$$
\varphi_{Sa/Bi} = \int_0^\infty \Phi_{\text{TRIGA}}(E)\, T_{Sa/Bi}(E)
$$

$\varphi_{0/0}$	$\varphi_{15/0}$	$\varphi_{15/5}$	$\varphi_{15/10}$	$\varphi_{15/15}$
1	0.361	0.190	0.108	0.067

Tab. 3.1.: The filter factor $\varphi_{Sa/Bi}$ for the four different filter sets.
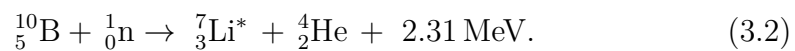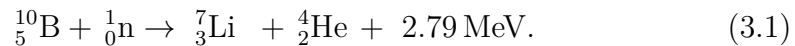
Tab. 3.1 also shows the supremacy of sapphire over bismuth with respect to neutron transmission: while 15 cm sapphire reduces the total neutron flux to about a third, adding only 5 cm reduces the total neutron flux to about one half. A filter set of 15 cm sapphire and 15 cm bismuth transmits only about 7 % of the total neutron flux of the TRIGA flux spectrum.

3.2. Composition of the radiation shielding concrete

The process of simulating the radiation shielding chamber required a lot of iterations. Many different variations of shielding geometry and properties had to be tested and it became more and more evident that ordinary concrete as shielding material would neither fulfill the required shielding properties nor provide sufficient spare space for experiments, since walls made just of ordinary concrete would have been much too thick. Therefore, as a result of our simulations, a special kind of radiation shielding concrete was designed[1] and transferred into a concrete recipe which may be manufactured by a commercial company. The recipe can be found in Tab. 3.2 and in much more detail in the Appendices A.2 and A.3.

Three essential additives improve the concrete's shielding abilities:

Boron carbide B_4C - With its high absorption cross section of $3835\,b$ the isotope ^{10}B is mainly responsible for the strong absorption of thermal neutrons in boron, leading to the following two reactions:

$$^{10}_{5}B + {}^{1}_{0}n \rightarrow {}^{7}_{3}Li \ + {}^{4}_{2}He + \ 2.79\,\text{MeV}. \tag{3.1}$$

$$^{10}_{5}B + {}^{1}_{0}n \rightarrow {}^{7}_{3}Li^* + {}^{4}_{2}He + \ 2.31\,\text{MeV}. \tag{3.2}$$

The first reaction has a probability of 7%, the second of 93%. The excited $^{7}_{3}Li$ nucleus emits a gamma photon of about $478\,\text{keV}$. This shows that shielding neutrons is a trade-off of a thermal neutron to 0.94 low-energy gamma photons. That this trade-off is beneficial for minimizing dose-rates shows Fig. 2.1. Unfortunately B_4C is quite expensive[2] and difficult to machine.

Hematite Fe_2O_3 - this additive increases the density of the concrete for better gamma shielding properties ($\rho \sim 5.3\,\text{g\,cm}^{-3}$).

Serpentine - Since hydrogen has a high (incoherent) neutron scattering cross section and its mass is almost the same as that neutrons it is an excellent moderation material. Serpentine contains crystallization water which enhances the moderation properties for epithermal and fast neutrons.

3.2.1. Concrete recipe evaluation

Since the main goal is to simulate the whole chamber made of this shielding concrete, it is crucial to translate the recipe reliably to MCNP. For this purpose slabs of shielding concrete but also of ordinary concrete with a dimension of $40 \times 40 \times 6\,\text{cm}^3$ were cast for comparison (Fig. 3.1). Experiments and numerical simulations have been done to evaluate the shielding properties of these slabs. The results of the simulations and the experiments were compared to find the optimal MCNP recipe of the shielding concrete. The simulated geometry can be seen in Fig. 3.2.

By means of gold foils activation the neutron flux behind a variable number of concrete slabs was measured. Additionally both the neutron and the gamma dose

---

[1]from Smartminerals GmbH

[2]about 40 € per kg

shielding concrete recipe	
Water content	$180 \, \mathrm{kg \, m^{-3}}$
Hematite	$2164 \, \mathrm{kg \, m^{-3}}$
Serpentine	$690 \, \mathrm{kg \, m^{-3}}$
Boron carbide B_4C	$68 \, \mathrm{kg \, m^{-3}}$
Density	$3360 \, \mathrm{kg \, m^{-3}}$

Tab. 3.2.: The recipe of the new shielding concrete. The B_4C content is variable. For the slabs casted for preliminary characterization experiments a content of $68 \, \mathrm{kg \, m^{-3}}$ was used, while for the finally realized chamber the content was $34 \, \mathrm{kg \, m^{-3}}$. For more details, see Appendix A.2 and [63, 64].

rates were measured. By this procedure it was possible to determine their shielding properties and compare these with the results of the numerical simulations.

An obviously superior behavior of the shielding concrete was found, but even more important was the assessment of a satisfying recipe for MCNP to simulate the accurate shielding properties of the whole chamber, (see Appendix A.3 and [65, 66]).

As for the real concrete this recipe contains about 20 different isotopes. Their proportions may vary slightly since the production of concrete is not an exact science. Therefore recipe is just a (good) estimation because no exact data were available.

Therefore, all shares of the ingredients of the MCNP recipe were varied during the simulations to find out any changes in the shielding properties. As expected, it turned out that the shielding properties of the concrete are only sensitive to variations of hydrogen and/or boron content, as well as of the total density. However, all these parameters are well known quantitatively and therefore can be controlled easily.

Since B_4C is by far the most expensive additive, the optimal concentration of B_4C for the chamber was investigated by simulating the neutron flux behind shielding concrete slabs with different contents of B_4C. From Fig. 3.3 it becomes evident that behind one slab without B_4C the neutron flux is about 4 times higher than for a slab containing B_4C. Behind two slabs without B_4C the flux is about twice as high as with added B_4C. Firstly, these simulations demonstrate the positive effect of B_4C on the shielding properties, and secondly, that there is no advantage in adding more than 1% B_4C. So, 1% is the optimal amount of B_4C which finally was chosen for the shielding concrete to build the whole chamber of the new *Thermal White Neutron Beam* facility.

3.2.2. Dose rate progression in concrete

Simulations comparing the dose rate progression inside of ordinary and shielding concrete lead to the following remarkable observations:

Firstly, with ordinary concrete shielding walls for the *Thermal White Neutron Beam* facility would have to be more than twice as thick as with shielding concrete
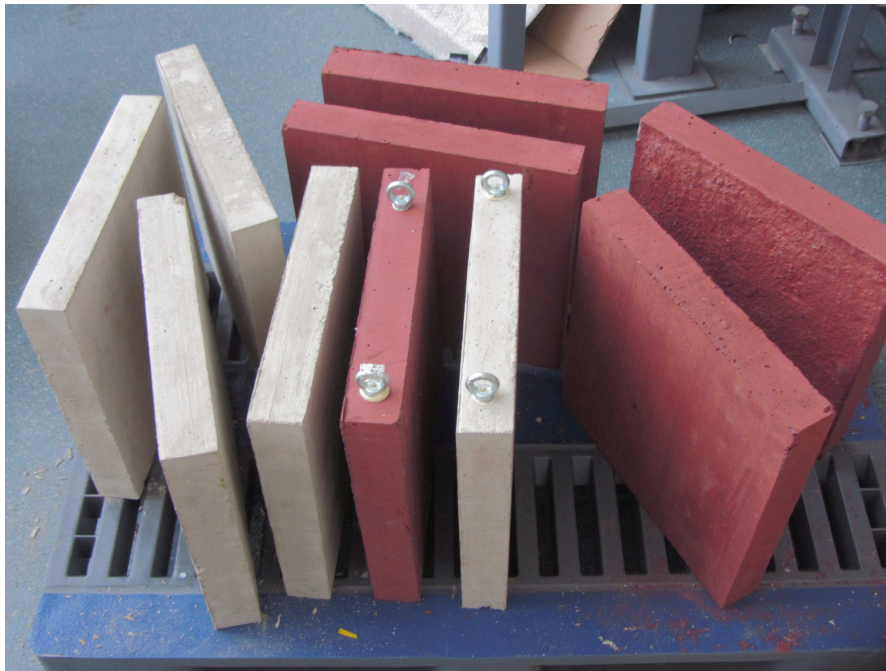
Fig. 3.1.: Concrete slabs of $40 \times 40 \times 6\,\text{cm}^3$ made of the new shielding concrete (red) and of ordinary concrete (gray) for comparison experiments. The red color is caused by the content of hematite.
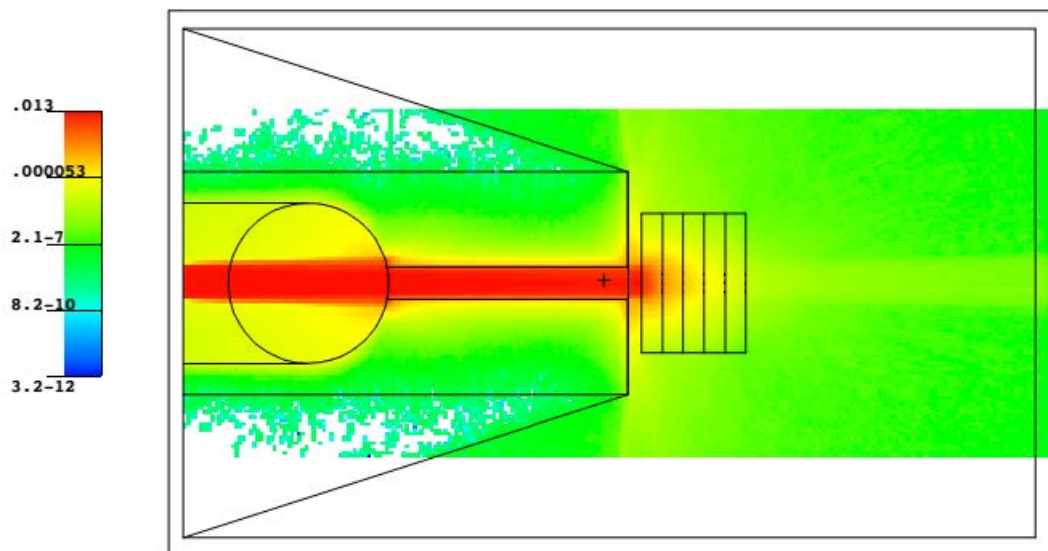

Fig. 3.2.: Layout of the MCNP simulation of the concrete shielding evaluation [66]. The neutron beam enters from the left (red), the trapezoidal geometry to the left is a boron acid tank standing directly in front of the beamtube. The five rectangles located in the center are the concrete slabs.
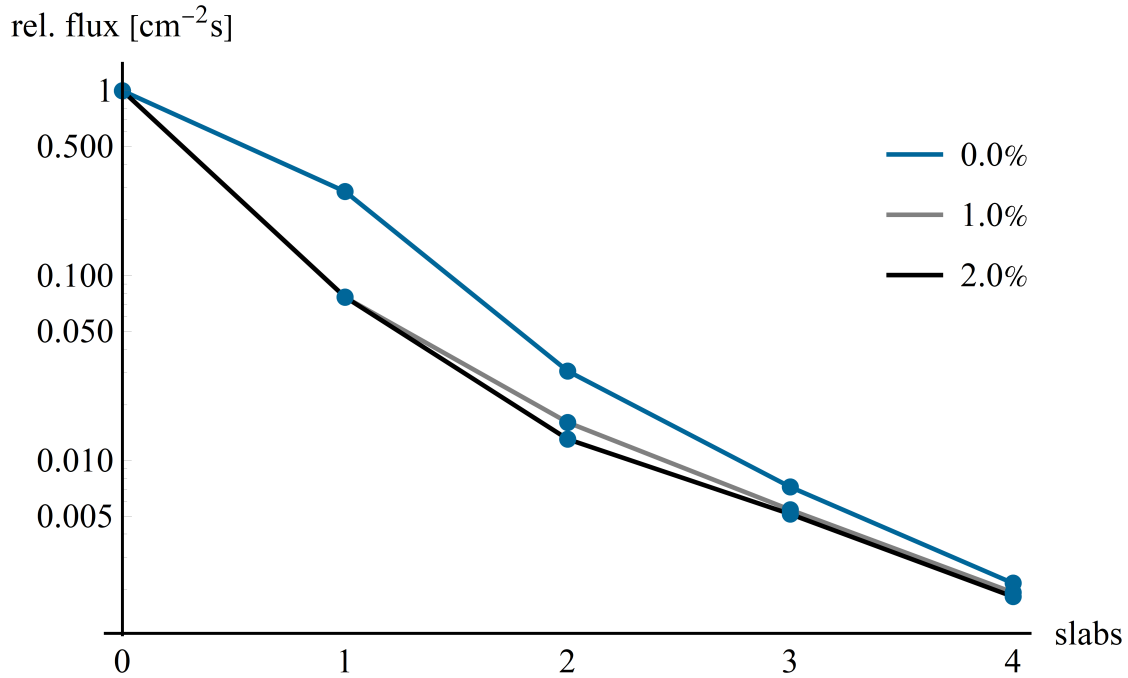
Fig. 3.3.: Relative neutron flux after shielding concrete slabs ($40\times40\times6\,\mathrm{cm}^3$) with varying B_4C content simulated in MCNP: without B_4C, after one slab the neutron flux is about 4 times higher, after two slabs, the flux is about twice as high as with added B_4C. Adding more than 1% B_4C is useless since there is an obvious saturation effect.

to meet the dose rate limit of $5\,\mathrm{\mu Sv\,h^{-1}}$, as can be seen from Fig. 3.4a. This would be neither practical nor possible.

Secondly, Fig. 3.4 clearly shows that the dose rate values for $0\,\mathrm{cm}$ (i.e. on the inner surface of the chamber) are much smaller for the shielding concrete, although the neutron source and the geometry in both simulations are exactly the same. While neutrons are absorbed in the shielding concrete rather quickly, the probability of being scattered back into the chamber is much higher for ordinary concrete due to the lack of neutron absorbing matter. This leads to higher dose rate values inside the chamber and therefore to a higher disturbing background for experiments.

Thirdly, Fig. 3.4 b also shows that in ordinary concrete behind several cm of shielding, the main dose rate source is no longer neutron radiation but secondary γ-radiation produced within the concrete. Within shielding concrete neutrons are mostly absorbed by B_4C, and according to Eq. (3.2) they release only low-energy secondary γ-radiation. And due to the presence of B_4C they are absorbed less deeply in the wall since compared to ordinary concrete more material of higher density is available to absorb the secondary gamma radiation.

Fourth, due to the good collimation of the beam the reactor gamma dose rate is the smallest fraction of the total off-beam dose rates, as can be seen also from Fig. 3.4 b.

(a) total dose rate

(b) neutron, secondary- and reactor gamma dose rate
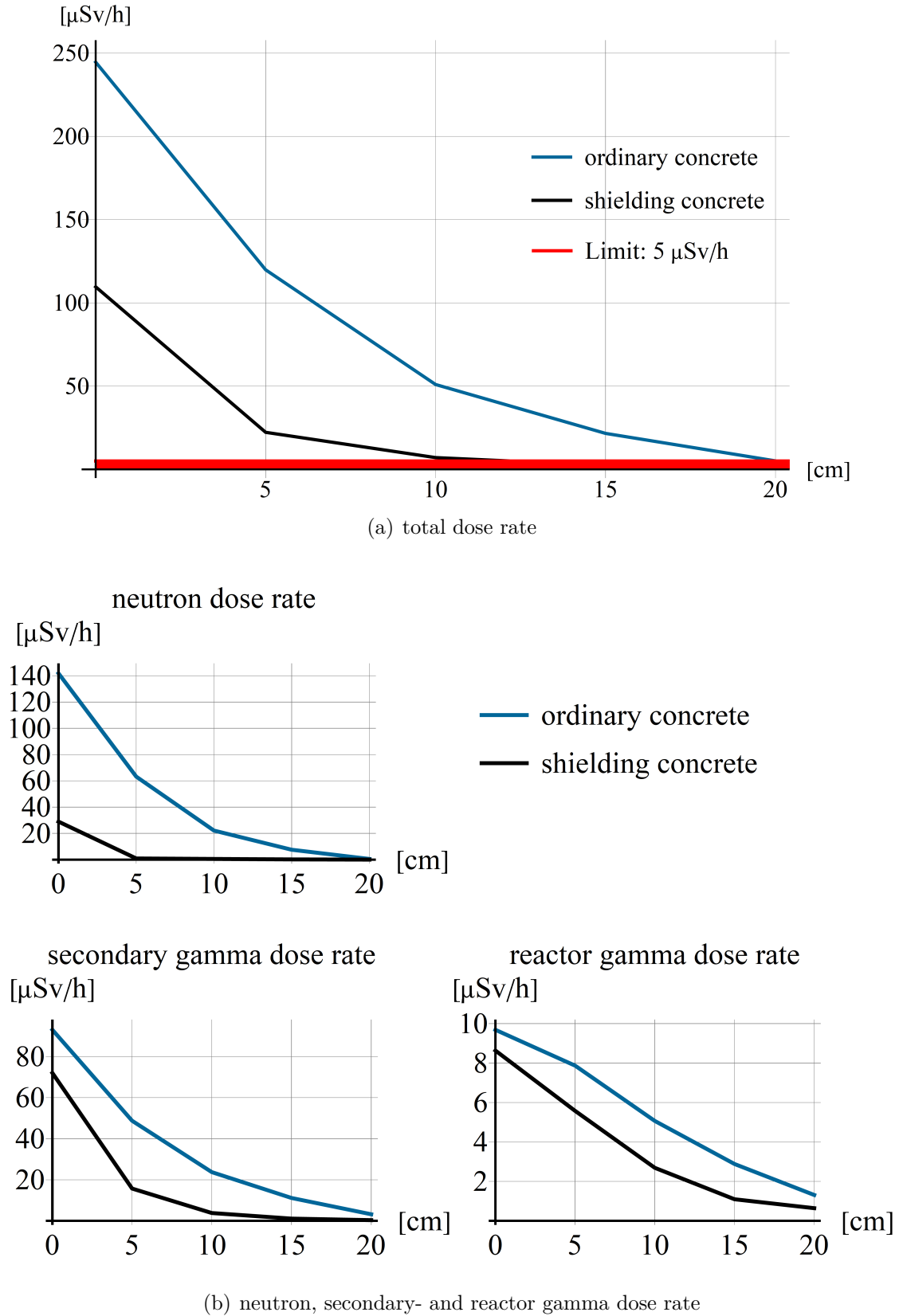
Fig. 3.4.: Simulated dose rate distributions in ordinary and shielding concrete. Data were taken from a full chamber model simulation at position about 30 cm next to the beam stop perpendicular to the direct beam. Notice that the scaling of the ordinates is different for the various quantities and chosen according to optimal visibility of the data.

Fig. 3.5.: Ground view of the shielding of the *Thermal White Neutron Beam* facility (roof removed). [34].

Fig. 3.6.: Open pre-chamber with installed shutter block ($\sim 70 \times 74 \times 67 \, \text{cm}^3$) standing on a hydraulic lift table. On the right the limit switches for positioning are visible. More pictures can be found in Appendix A.3.

3.3. Geometry

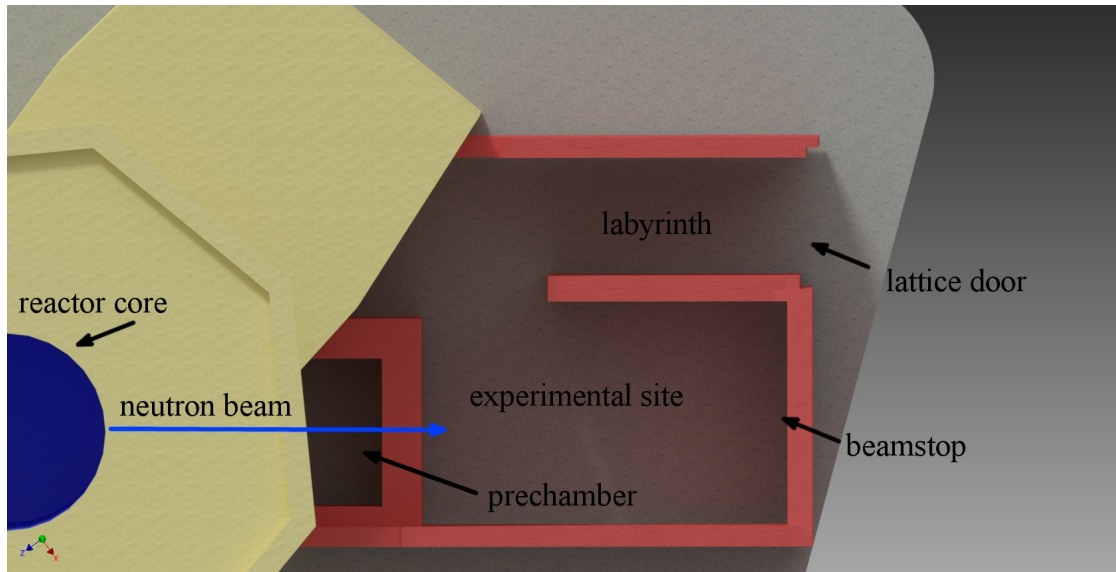One of the aims of the project was to install a neutron beam facility, where the experimental site is accessible during reactor run time. Therefore it was necessary to install a reliable beam shutter that is combined with an absolutely safe entrance control system.

Besides that, the most demanding challenge of finding a geometry for the chamber was the accessibility of the experimental zone: first ideas about a concrete chamber with sliding doors made of concrete were rejected due to its complexity. A concept of a chamber accessible through a labyrinth was worked out, where there is a simple mesh door at the entrance for locking the access to the open neutron beam. After several iterative simulations, it was shown that a labyrinth entrance is feasible since multiple neutron scattering inside the chamber is insignificant, which can be seen from Fig. 3.8. Also, the feasibility of blocking the neutron beam and gamma radiation with a shutter block in front of the beamtube to "turn off" the neutron beam was shown [59, 67], and can be seen from Fig. 3.6. Finally, the design of the chamber shown in Fig. 3.5 was fixed.

Simulations revealed that fulfilling the dose rate limit of $5\,\mu\mathrm{Sv}\,\mathrm{h}^{-1}$ is only possible by using a special shielding concrete. For this, the whole chamber was simulated with several different concrete recipes (ordinary concrete, ordinary concrete with different percentages of B_4C, heavy concrete, borated heavy concrete, shielding concrete). The results of the most important and interesting simulations are summed up in Tabs. 3.3, 3.4, and 3.5.

Ordinary concrete - Tab. 3.3 shows that the chamber made of ordinary concrete (shown in Appendix A.3) cannot fulfill the limit of $5\,\mu\mathrm{Sv}\,\mathrm{h}^{-1}$, since almost all total dose rate values are larger. This is essentially due to the smaller and less effective neutron absorption of ordinary concrete compared with specially optimized shielding concrete and the hence increased secondary γ-radiation that is produced within the wall.

Shielding concrete - Tabs. 3.4 and 3.5 show results of simulations of the chamber made of shielding concrete with 1 weight percent B_4C with open and closed shutter. The raised dose rate at tally number 6 can be neglected, since at this position the reactor foundation was not considered in the simulation. Furthermore, the dose rate next to the beamstop (position 13) is also somewhat raised but only from reactor gamma radiation. This problem can be solved easily by increasing the collimation of the direct reactor gamma beam by adding boron steel apertures inside the beamtube and inside the beamport in the intermediate wall (position 2).

Tab. 3.5 shows that for closed beam shutter the limit of $5\,\mu\mathrm{Sv}\,\mathrm{h}^{-1}$ is not exceeded also within the chamber: directly at the beamport (position 2), the dose rate is just $1.45\,\mu\mathrm{Sv}\,\mathrm{h}^{-1}$. Thus it is proven that the shutter system works properly and the chamber can be entered safely.
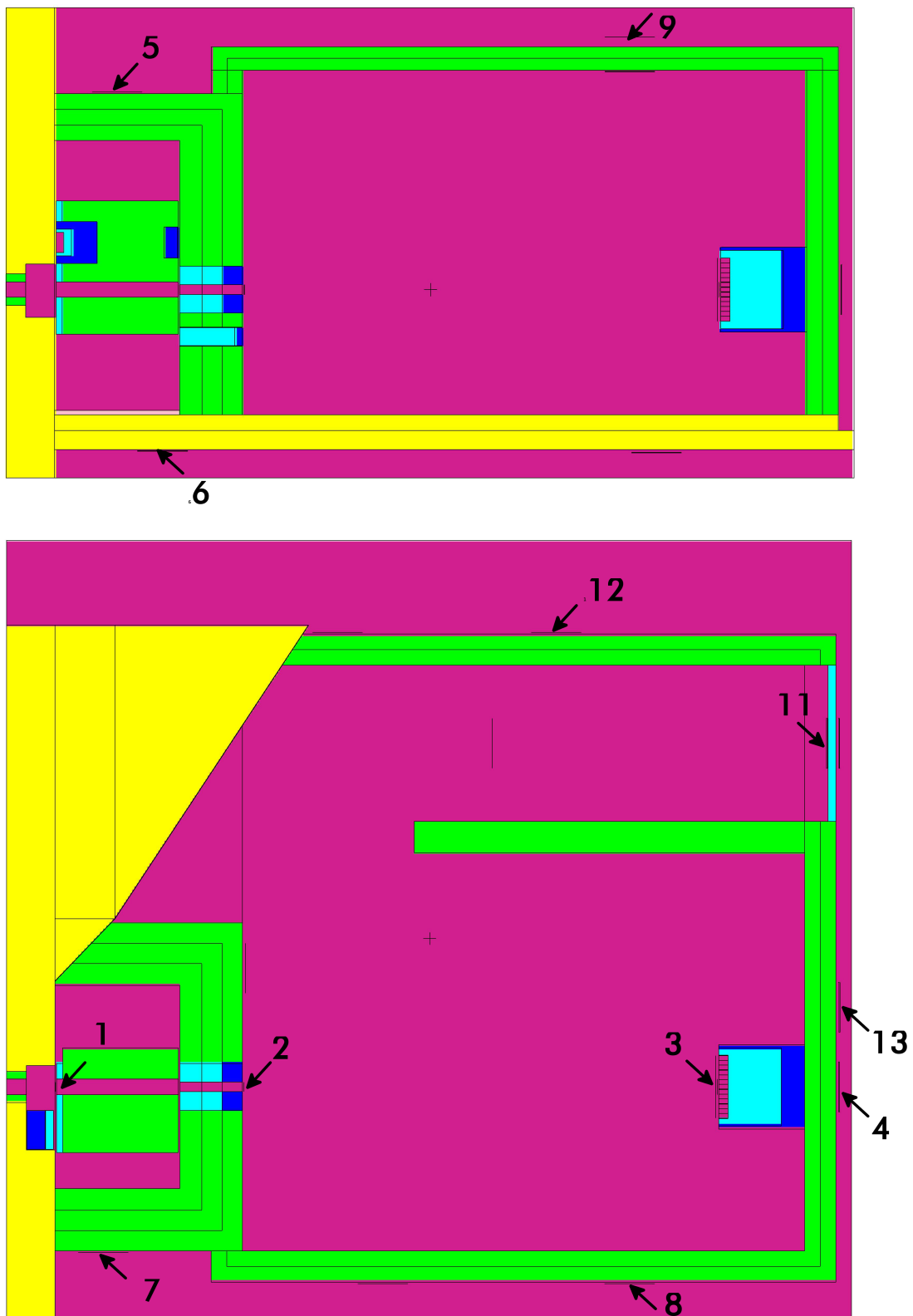
Fig. 3.7.: Side and ground view of the shielding of the *Thermal White Neutron Beam* facility [34]. The numbers correspond to the tallies in Tabs. 3.3, 3.4, and 3.5.

Fig. 3.8.: MCNP simulation for neutrons. The shadow behind the wall of the labyrinth can be seen, indicating that the concept of entering via such a labyrinth works properly. A scale value of 0.013 corresponds to $5\,\mathrm{Sv\,h^{-1}}$, 3.4×10^{-9} to $1\,\mathrm{\mu Sv\,h^{-1}}$ [34].

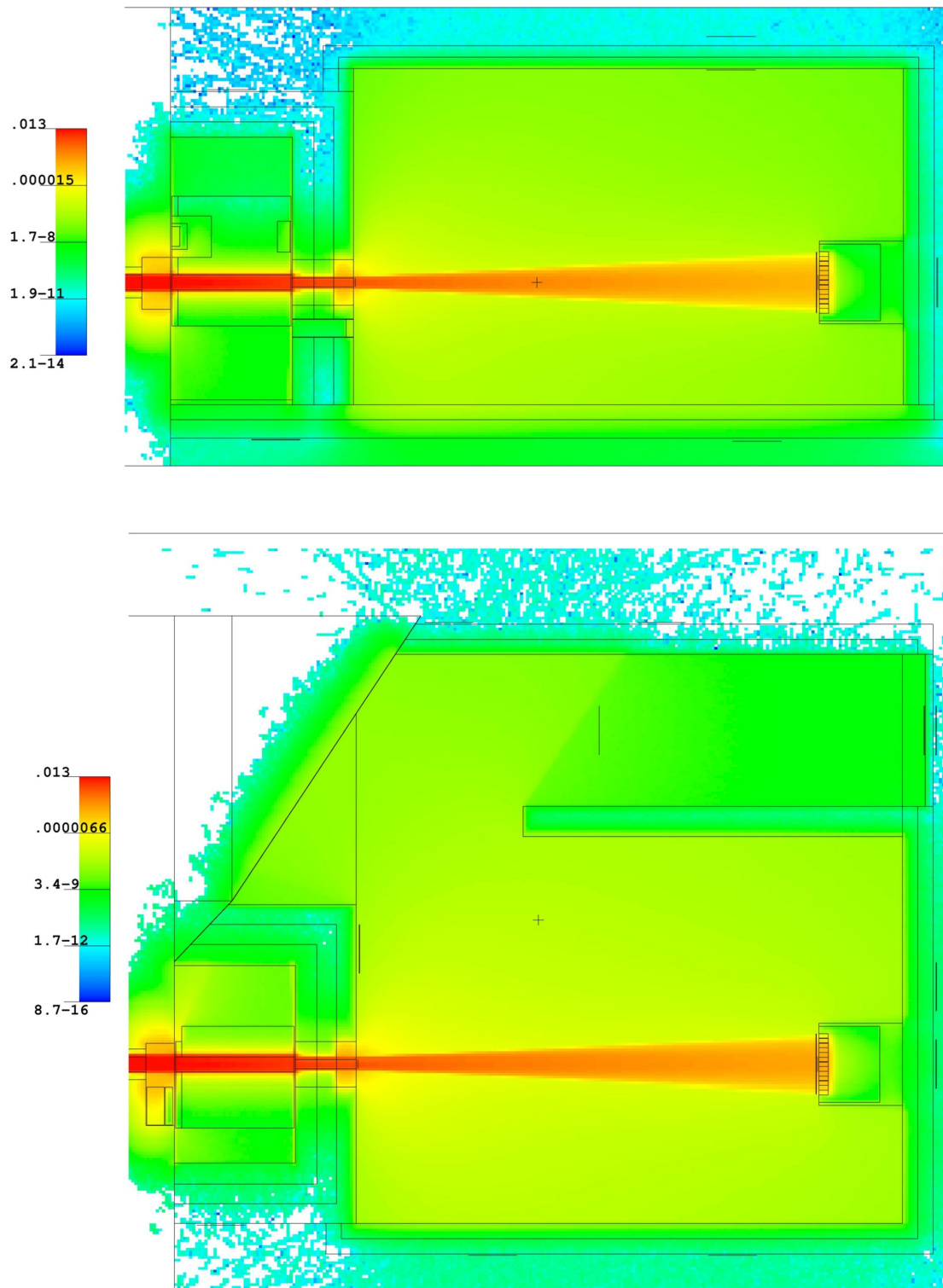|		$\dot{D}_n$	$\dot{D}_{sec}$	$\dot{D}_{reac}$	$\dot{D}$
		$\mathrm{H}^*(10)\,[\mu\mathrm{Svh}^{-1}]$			
4	behind beamstop	7.62	0.92	0.04	8.58
5	VK roof	1.80	5.48	0.00	7.28
6	VK floor	20.00	34.42	0.03	54.45
7	VK side	1.39	5.89	0.00	7.28
8	EK side	3.47	2.90	0.00	6.37
9	EK roof	3.55	3.08	0.01	6.64
10	EK floor	0.56	0.93	0.00	1.49
11	labyrinth exit	3.27	0.83	0.00	4.10
12	labyrinth side	0.51	1.24	0.00	1.75
13	beamstop side	2.52	1.09	0.18	3.79

Tab. 3.3.: Simulation of the dose rate distribution inside and outside of the shielding chamber made of **ordinary concrete** with neutron and gamma spectrum of the 15/10-sapphire/bismuth standard filter set inserted in the beamtube. Positions correspond to numbers in Fig. 3.7. Internal dose rate limit which must be fulfilled is $5\,\mu\mathrm{Sv}\,\mathrm{h}^{-1}$. Statistical errors in the simulation are smaller than 10%.

		$\dot{D}_n$	$\dot{D}_{sec}$	$\dot{D}_{reac}$	$\dot{D}$
		$\mathrm{H}^*(10)\,[\mu\mathrm{Svh}^{-1}]$			
4	behind beamstop	0.30	0.06	0.03	0.39
5	VK roof	0.23	0.18	0.00	0.40
6	VK floor	3.88	2.38	0.02	6.28
7	VK side	0.17	0.09	0.00	0.26
8	EK side	0.78	0.19	0.00	0.98
9	EK roof	0.59	0.27	0.01	0.87
10	EK floor	0.11	0.15	0.00	0.26
11	labyrinth exit	0.21	0.08	0.00	0.29
12	labyrinth side	0.08	0.05	0.00	0.13
13	beamstop side	0.31	0.07	0.14	0.52

Tab. 3.4.: Simulation of the dose rate distribution of the shielding chamber made of **shielding concrete with open shutter** with neutron and gamma spectrum of the 15/10-sapphire/bismuth standard filter set inserted in the beamtube. Positions correspond to numbers in Fig. 3.7. Internal dose rate limit which shall be fulfilled is $5\,\mu\mathrm{Sv}\,\mathrm{h}^{-1}$. Dose rate value 6 is higher than the limit, but on that position the foundation of the reactor is missing in the simulation. Statistical errors in the simulation are smaller than 10%.

		$\dot{D}_n$	$\dot{D}_{sec}$	$\dot{D}_{reac}$	$\dot{D}$
			$H^*(10)\,[\mu\mathrm{Svh}^{-1}]$		
2	**beamport**	**1.43**	**0.01**	**0.01**	**1.45**
4	behind beamstop	0.00	0.00	0.00	0.00
5	VK roof	1.08	1.07	0.05	2.21
6	VK floor	0.10	0.73	0.01	0.84
7	VK side	0.10	0.22	0.00	0.32
8	EK side	0.00	0.00	0.00	0.00
9	EK roof	0.00	0.00	0.00	0.00
10	EK floor	0.00	0.00	0.00	0.00
11	labyrinth exit	0.00	0.00	0.00	0.00
12	labyrinth side	0.00	0.00	0.00	0.00
13	beamstop side	0.00	0.00	0.00	0.00

Tab. 3.5.: Simulation of the dose rate distribution of the shielding chamber made of **shielding concrete with closed shutter** with neutron and gamma spectrum of the 15/10-sapphire/bismuth standard filter set inserted in the beamtube. Positions correspond to numbers in Fig. 3.7. The internal dose rate limit which has to be fulfilled is $5\,\mu\mathrm{Sv\,h}^{-1}$. Statistical errors in the simulation are smaller than 10%.

3.4. Discussion of the simulation results

The simulations in MCNP mentioned above laid the foundation of the project because its feasibility was confirmed.

It was shown, that shielding the beam without special shielding concrete would lead to walls too thick to be practicable. A recipe for shielding concrete was designed, translated to MCNP and tested experimentally. Since B_4C is the most expensive additive, the sufficient amount for the shielding chamber was found to be 1 weight percent. A feasible and handy chamber design was found. The chamber's integrated shutter system, accessibility when the reactor is running and handy accessibility without moving concrete walls but with a labyrinth system was shown to meet the given dose rate limit of $5\,\mu\mathrm{Sv\,h}^{-1}$ in every situation.

Furthermore, comparing the simulated dose rates outside of the chamber with real measurements (as will be described in the next chapter) allows for ex post benchmarking of the quality of the filter spectrum calculation, as it was performed and discussed in Chapter 2.

4. Characterization of the New Facility

A<small>FTER</small> finishing the installation of the *Thermal White Neutron Beam* facility the quality of the radiation shielding was examined carefully for getting a permanent permission for its operation from the responsible ministry. This examination was done in collaboration with an external expert. The academic interest of these measurements was mainly in the deviations compared to the simulations described in Chapter 3. Details of this comparison are given in Section 4.1.

After a general positive survey, the characteristics of the yet unknown neutron beam, as there are

- neutron flux at different positions
- beam cross section at different positions
- beam divergence
- beam homogeneity
- Cd-ratio of the neutron spectrum
- in-beam neutron and γ-dose rates
- the thermal neutron flux spectrum ,

were determined quantitatively. Sections 4.2 to 4.4 describe how these experiments were performed and present also their respective results. In Section 4.5, an estimation of the activation of the facility is given which is important for the dismantling process after its lifetime. The last section in this chapter is dedicated to a 'quick and dirty' Laue-Bragg-camera setup, which was installed in the radiation chamber of the new facility to demonstrate its usefulness and its adaptability to specific experimental requirements by examining the quality of the (finally left over) thinnest ($d_{Bi} = 5$ cm) of the two bismuth single crystals used for the construction and test of the radiation filter sets.

4.1. Dose rate measurements

The ambient dose rates $\dot{D}_i$ on the chamber's outer surface are of legal interest since the compliance of the limits needs to be verified in order to get the permission of routine operation of the facility. Therefore, these measurements were done first, in cooperation with the external international consultant[1] of the Ministry of Science, Research and Economy.

Comparing the results of the MCNP simulations with the measured ambient dose rate values will reveal the quality of the calculation of the spectrum in Chapter 2.

On the outer surface of the chamber a raster of measuring positions of about 50×50 cm^2 was defined and the ambient dose rates for neutron and gamma radiation

---

[1]Dr. Gabriele Hampel

were measured with a FH 40 G dosemeter, bought from a company named Thermo-Scientific [68]. The most prominent data points of this measurement are listed in Tab. 4.1. The background at these positions is listed in Tab. 4.2. Numbers correspond to the positions indicated in Fig. 3.7.

All ambient dose rates $\dot{D}_i$ in Tab. 4.1 were below the limit of $5\,\mu\text{Sv}\,\text{h}^{-1}$. Without meeting this specification it would not have been possible to get a legal permission for our new facility. Therefore, this is a very satisfying outcome!

To compare the measured dose rates given in Tabs. 4.1 and 4.2 with those of the MCNP simulations (see Tab. 3.4) it was looked for any statistical significant deviations. For this, it was checked for every position whether the difference between simulation and measurement is compatible with 0 using a 3σ-interval. This was done simply by using the relation

$$p_i = |\dot{D}_{Sim,i} - \dot{D}_{Meas,i} + \dot{D}_{Bg,i}| - 3\sigma_i\,. \tag{4.1}$$

Negative values of p_i mean that simulation and measurement are in agreement. On the other hand, positive values show a statistical significant deviation. The values of p_i at the various locations are compiled in Tab. 4.3.

The table shows very satisfying results. In all positions except "VK roof" the measurement is in full agreement with the simulation. This is quite impressive since a lot of assumptions had to be made for the calculation of the spectrum, the estimation of concrete recipe, and the definition of the model geometry. This is an indicator that all these assumptions were justified, but most importantly it indicates that the calculation of the neutron spectrum, especially of its fast region, is reliable.

The reason for the mismatch at the position "VK roof" can be found in the background measurement and the design of the shutter. The background measurement was done while the shutter was closed, hence the block was in the lower position. This leads to mediocre shielding properties on the roof of the pre-chamber and therefore to a background dose rate which is higher as when the shutter is opened.

Furthermore, a harder reactor γ-radiation spectrum than expected, or a higher total flux of reactor γ-radiation might be minor reasons for the deviation in $\dot{D}_\gamma$. Since the γ-radiation from the reactor is collimated, these possibilities affect the measurement "behind beamstop" and "beamstop side" most.

4.1.1. Characterization of the shielding concrete

After the installation of the new facility, the experiment described in Section 3.2.1 was repeated [71]. Since the installed filters change the neutron spectrum especially in the fast region enormously, measuring neutron dose rate, gamma dose rate, and neutron flux increases the reliability of the estimated shielding concrete recipe and the neutron flux spectrum.

Again, neutron and gamma dose rates were measured behind slabs of shielding concrete, as it is shown in Fig. 4.1. This experiment was also simulated in MCNP for comparison, shown in Fig. 4.2 and 4.3. These plots reveal that the simulation can predict the results of the measurement quite well within the required limits.

		$\dot{D}_n$	$\dot{D}_\gamma$	$\dot{D}$
		H*(10) [μSvh^{-1}]	
4	behind beamstop	0.85	0.42	1.27
5	VK roof	0.55	0.40	0.95
7	VK side	1.55	1.05	2.60
8	EK side	1.60	0.60	2.20
9	EK roof	1.70	0.65	2.35
11	labyrinth exit	0.60	0.25	0.95
12	labyrinth side	0.23	0.18	0.41
13	beamstop side	0.60	0.25	0.95

Tab. 4.1.: Ambient dose rates at selected positions for neutrons $\dot{D}_{n,i}$, gamma radiation $\dot{D}_{\gamma,i}$, and their sum $\dot{D}_i$ on the outer surface of the new facility [69, 70]. The numbers correspond to the positions indicated in Fig. 3.7. All measurements were done at 250 kW thermal power of the recator.

		$\dot{D}_n$	$\dot{D}_\gamma$	$\dot{D}$
		H*(10) [μSvh^{-1}]	
4	behind beamstop	0.08	0.16	0.24
5	VK roof	2.50	0.64	3.14
7	VK side	0.14	0.58	0.72
8	EK side	0.10	0.23	0.33
9	EK roof	0.15	0.36	0.51
11	labyrinth exit	0.045	0.127	0.172
12	labyrinth side	0.065	0.21	0.275
13	beamstop side	0.075	0.137	0.212

Tab. 4.2.: Background dose rates at the same positions as in Tab. 4.1 for closed beam shutter and 250 kW reactor power.

		$\dot{D}_n$	$\dot{D}_\gamma$	$\dot{D}$
				p_i
4	behind beamstop	-0.05	-0.02	-0.07
5	VK roof	+0.64	+0.10	+0.75
7	VK side	-0.06	-0.35	-0.39
8	EK side	-0.23	-0.21	-0.43
9	EK roof	-0.08	-0.31	-0.39
11	labyrinth exit	-0.02	-0.08	-0.09
12	labyrinth side	-0.06	-0.04	-0.25
13	beamstop side	-0.16	-0.04	-0.38

Tab. 4.3.: As defined in Eq. (4.1), p_i shows that simulation and measurement are in agreement.

Fig. 4.1.: Measurement of dose rate and flux progression inside of shielding concrete slabs using the new neutron beam facility.

4.1.2. In-beam dose rate

In 1970 the ambient dose rate in front of beamtube C was measured by Alfred Hefner in the course of his doctoral thesis [72]. Due to the similar geometry of beamtubes B and C their dose rate values turned out to be of comparable size.

Hefner measured $12\,880\,\text{rem/h}$ (which are equivalent to $12.8\,\text{Sv}\,\text{h}^{-1}$) without any collimator system inside of the beamtube at $250\,\text{kW}$ $1\,\text{m}$ away from the beamport for the sum of neutron and γ-radiation. A comparison with the reported ambient dose rate value of $0.2\,\text{Sv}\,\text{h}^{-1}$ from Pangl [73] shows the tremendous effect of the filter set on the ambient dose rate.

4.2. Flux measurements

Neutron scattering is an inherently intensity-limited technique. With the exception of some simple transmission techniques, a high as possible neutron flux is desirable for almost all neutron experiments to keep their required durations below an acceptable level. Even for likewise simple neutron irradiation experiments where the achievable reaction rates are directly proportional to the incident flux the latter is of crucial importance.

4.2.1. Metal foil activation

In general, the integral neutron flux Φ can easily be measured using the standard technique of metal foil activation [74, 75]. Metal foils of known composition, diameter and thickness, and thus known number of atoms n are irradiated in a neutron beam for a defined period of time t_{irr} leading to a neutron activation A which can easily be measured by β- or γ-spectroscopy of the decaying isotopes.
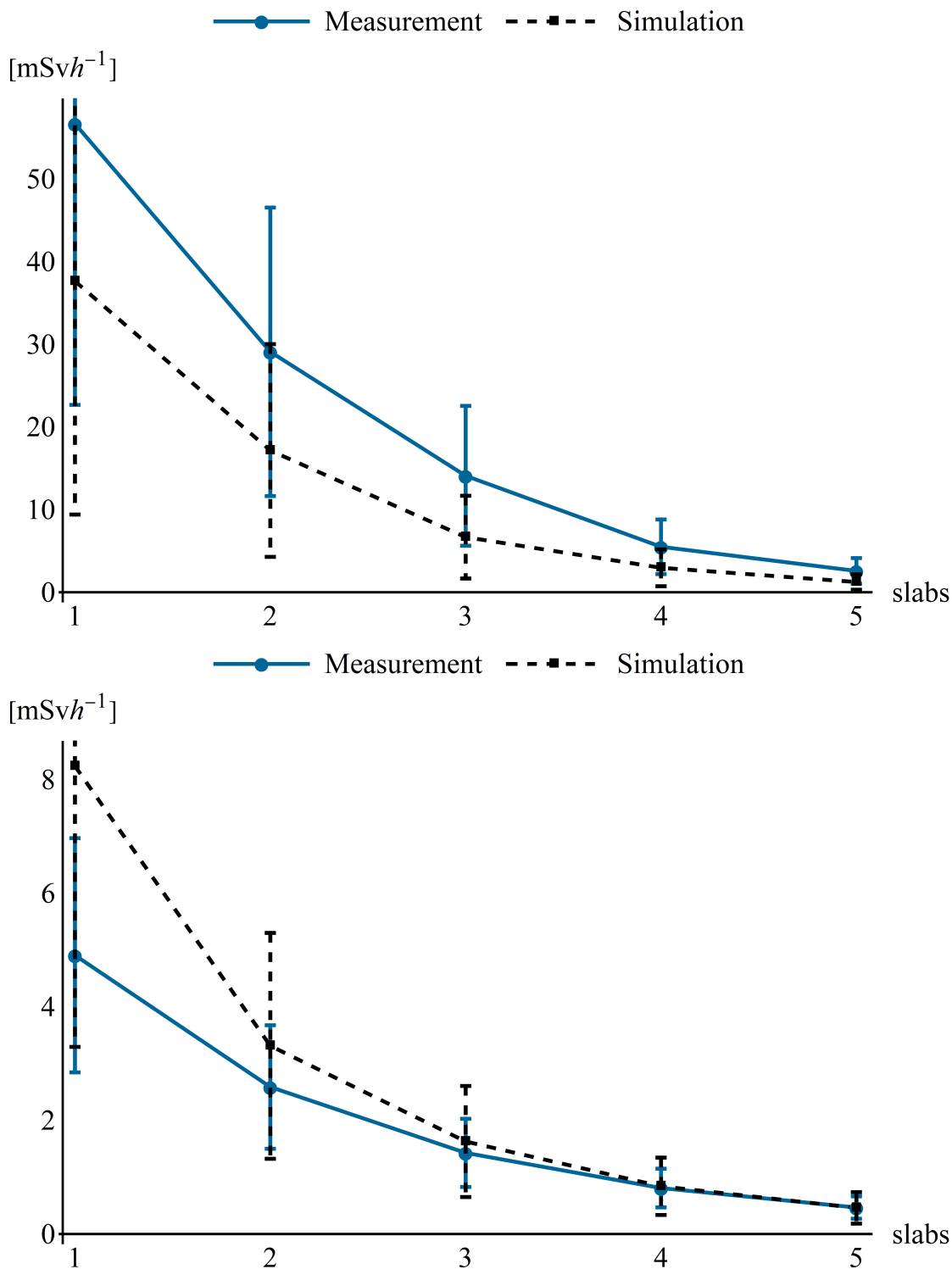
Fig. 4.2.: Simulation and measurement of the **neutron dose rate** (above) and **total gamma dose rate** (below) behind several slabs of shielding concrete.
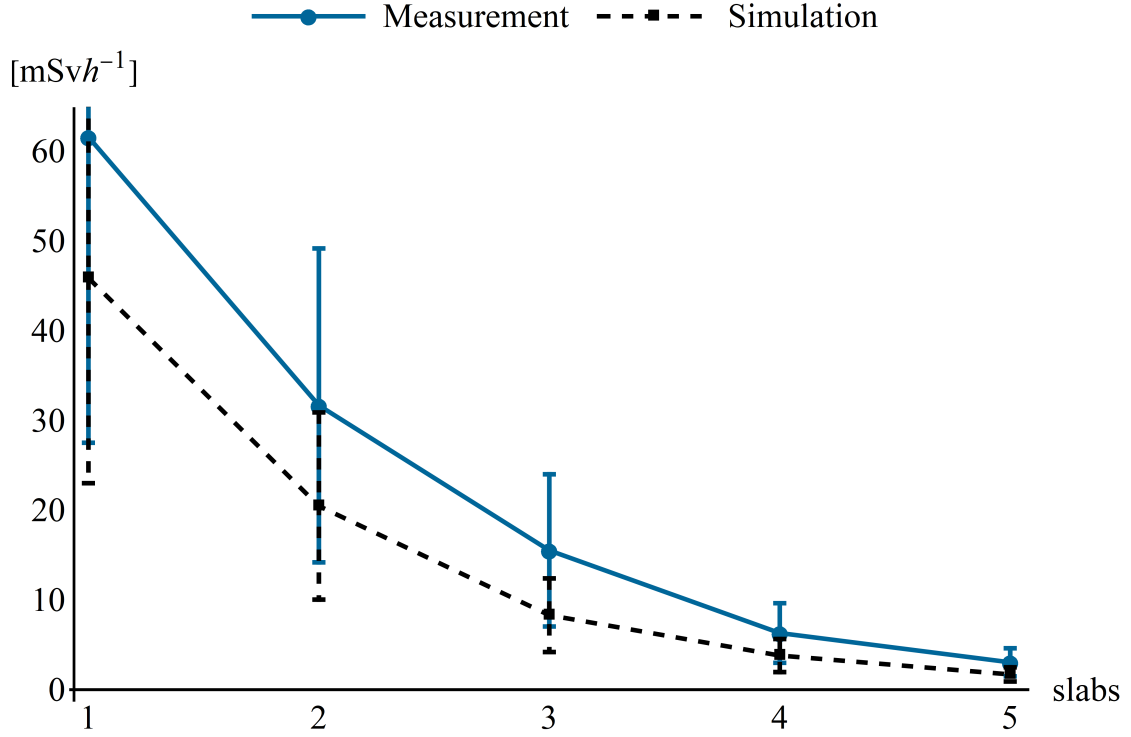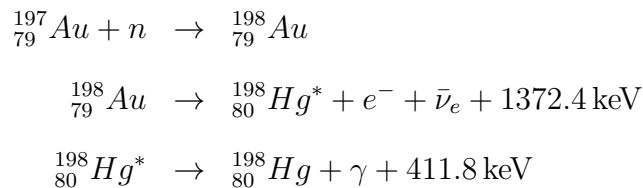
Fig. 4.3.: Simulation and measurement of the **total dose rate** behind several slabs of shielding concrete.

Many different elements can be used for this purpose like Al, Ti, Mn, Fe Co, Ni, Cu, Ag, In, Sn, Dy or Au. For such flux measurements thermal neutrons are often shielded by Cd-foils. Since there is a very steep increase in $\sigma_{abs,Cd}$ around $0.4\,\text{eV}$ (see Fig. 2.11) thermal neutrons get absorbed, leading to a measurement only of the epithermal & fast neutron flux $\Phi_{epi\,\&\,fast}$. Thus from two subsequent measurements without and with Cd-foil coverage it is possible to determine the pure thermal flux $\Phi_{thermal}$ via the trivial relation

$$\Phi_{thermal} = \Phi_{total} - \Phi_{epi\,\&\,fast}\,.$$

Different half-lifes, decay channels, absorption cross sections σ_{abs}, resonances or thresholds in the latter lead to different application areas for different elements. For thermal neutrons, Au and In are often the first choice due to a high neutron absorption cross section σ_{abs} (see Fig. 4.4) and a half-life which is long enough to allow for a convenient measurement of the activity A, but short enough to achieve sufficient statistical accuracy within reasonably short time interval. Moreover, the foils can be re-used after about 10 half-lifes when their activity has dropped roughly by three orders of magnitude.

Irradiation of Au-foils leads to the following chain of reactions

$$^{197}_{79}Au + n \quad \rightarrow \quad ^{198}_{79}Au$$

$$^{198}_{79}Au \quad \rightarrow \quad ^{198}_{80}Hg^* + e^- + \bar{\nu}_e + 1372.4\,\text{keV}$$

$$^{198}_{80}Hg^* \quad \rightarrow \quad ^{198}_{80}Hg + \gamma + 411.8\,\text{keV}$$

with a half-life of about 2.7 days for $^{198}_{79}Au$, and of only 23 ps for $^{198}_{80}Hg^*$. After irradiation of the 411.8 keV γ-photons can be registered by a γ-detector to determine the activation and to calculate the neutron flux.

After measuring the activity A of a metal foil which was irradiated in a *monoenergetic* neutron beam, the neutron flux in principle can be calculated using the formula

$$\Phi = \frac{A}{N\,\sigma_{abs,E}}$$

However, considering corrections on

- decaying nuclei while irradiating with neutrons
- decaying nuclei after irradiating with neutrons
- self shielding due to not infinitely thin metal foils
- detector efficiency

lead to the much more precise formula for the neutron flux

$$\Phi = \frac{\rho\,A\,e^{\lambda t_{inter}}}{\sigma_{abs,E}\,n\,\eta\,m\,G\,(1 - e^{-\lambda t_{irr}})} \tag{4.2}$$

with

$$G = \frac{1}{2\mu\frac{m}{F} + 1} \qquad \mu = \frac{n\sigma_{abs,E}}{\rho} \qquad n = \frac{\rho}{A_u}$$

and

Φ - the monoenergetic neutron flux $[\text{cm}^{-2}\,\text{s}^{-1}]$
ρ - metal density of Au $[19.32\,\text{g}\,\text{cm}^{-3}]$
A - measured activity $[\text{s}^{-1}]$
A_u - atomic mass $(197.97\,\text{u for }^{198}\text{Au})$
F - irradiated foil area $[\text{cm}^2]$
N - number of atoms in the foil
n - target atoms per cubic cm $[\text{cm}^{-3}]$
m - foil mass $[\text{g}]$
G - self shielding factor of the foil
η - detector efficiency of the β/γ-detector
t_{irr} - irradiation time $[\text{s}]$
t_{inter} - time between irradiation and measurement of activation $[\text{s}]$
$\sigma_{abs,E}$ - absorption cross section for the given neutron energy $[\text{cm}^2]$.

However, if the neutron beam is *polychromatic* the absorption cross section is energy dependent (see e.g. the $\frac{1}{v}$-dependence in the thermal and resonances in the epithermal area of ^{1}97Au in Fig. 4.4) weighting of $\sigma_{abs}(E)$ with the actual flux spectrum $N_{Flux}(E)$ of the neutron beam

$$\overline{\sigma}_{abs} = \int_0^\infty \sigma_{abs}(E)N_{Flux}(E)\,dE \tag{4.3}$$

results in a mean absorption cross section of the metal foil $\overline{\sigma}_{abs}^{mean}$, which has to be used in Eq. (4.2) instead of the monoenergetic value $\sigma_{abs,E}$.
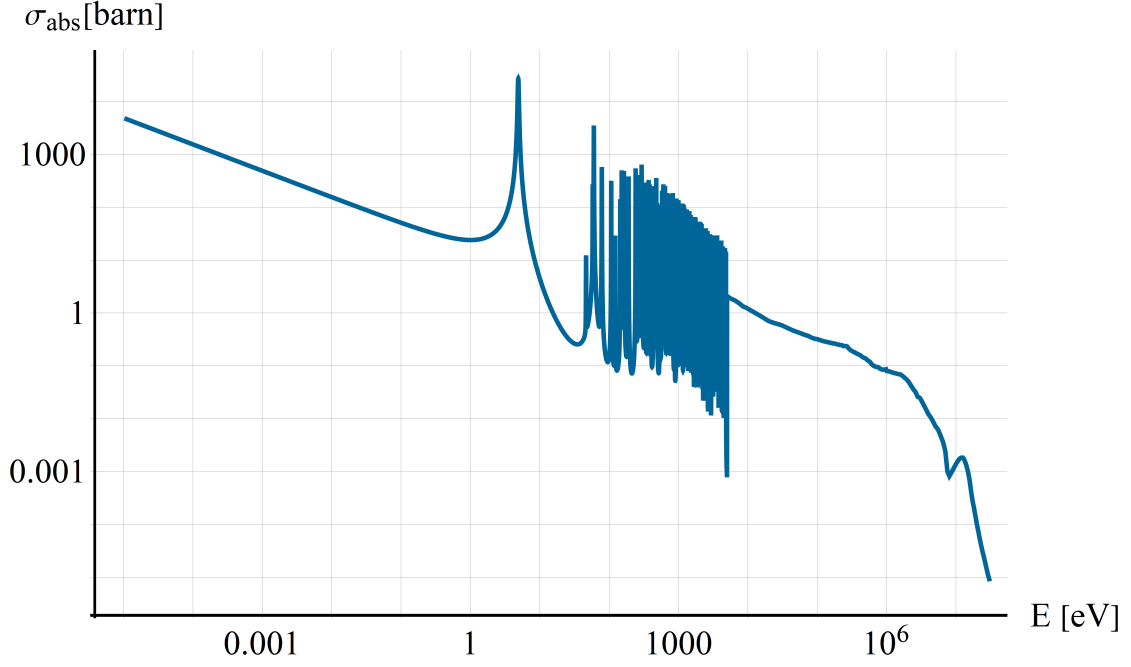
Fig. 4.4.: Neutron absorption cross section $\sigma_{abs}(E)$ of ^{197}Au.

$\overline{\sigma}_{abs}$ is the mean absorption cross section of a specific isotope for a given neutron flux spectrum $N_{Flux}(E)$. Clearly, the accurate measurement of the flux spectrum is of crucial importance for the determination of this artificial absorption cross section, which simplifies all further calculations since the energy-dependent functions $\sigma_{abs}(E)$ and $N_{Flux}(E)$ are now substituted by a single constant.

4.2.2. The mean absorption cross section

For Maxwell-Boltzmann-like distributed neutron beams, as they are available at the TRIGA reactor, often just the absorption cross section value at $25\,\mathrm{meV}$, corresponding to a neutron velocity of $2200\,\mathrm{m\,s^{-1}}$

$$\sigma_{\mathrm{abs,2200}} = 98.65\,\mathrm{b},$$

is used as an approximation.

Using an ideal Maxwell-Boltzmann flux distribution (see Eq. (2.2)) for a moderator temperature of $303\,\mathrm{K}$ and a simple $\frac{1}{v}$-approach, solving Eq. (4.3) results in [39]

$$\overline{\sigma}_{\mathrm{abs,analytical}} = 85.58\,\mathrm{b}.$$

Solving the integral in Eq. (4.3) for the TRIGA spectrum calculated in Eq. (2.11) and using the absorption cross section function for ^{197}Au (see Fig. 4.4) leads to a mean absorption cross section of

$$\overline{\sigma}_{\mathrm{abs,TRIGA}} = 81.28\,\mathrm{b}.$$

Since this value is quite close to $\sigma_{\mathrm{abs,2200}}$ the above mentioned approximation is justified for an estimation of the flux at an error level of about 20%.

Obviously the spectrum of the TRIGA reactor is somewhat harder than a theoretical Maxwell-Boltzmann distribution, which is not surprising, however, taking into account the epithermal and fast neutron contributions.

Solving the integral in Eq. (4.3) for the calculated spectrum of the thermal white beam (i.e. the spectrum behind the filter set) leads to

$$\overline{\sigma}_{\text{abs,WB}} = 98.41 \, \text{b} \, .$$

With this mean absorption cross section for the thermal white beam spectrum the neutron flux at beamtube B can be correctly determined from the measured gold foil activation data.

The shift in the mean absorption cross section compared to the flux spectrum without filters is due to the "softer" spectrum, since epithermal and fast neutrons are scattered out of the beam. This effect can be seen in Fig. 2.6: especially the bismuth filter scatters out very effectively the higher energetic part of the Maxwell-Boltzmann spectrum leading to a 'colder' Maxwell-Boltzmann spectrum. Exactly speaking, the filtered spectrum is just not exactly Maxwell-Boltzmann distributed because the higher energetic part is cut off by the filter set and at very low neutron energies (which in fact play no role at the unfiltered TRIGA spectrum) absorption by the aluminum nuclei of the sapphire filter has some minor influence. However, depending on the required precision of the approximation it is usually justified to assume the filtered spectrum as being Maxwell-Boltzmann distributed.

4.2.3. The mean absorption cross section for Cd-covered neutron activation

As described already in 4.2.1 metal foils can be covered with a thin foil of cadmium to absorb thermal neutrons. Then, the activation of the foil is due to neutrons with higher energy than $\sim 0.4\,\text{eV}$ because thermal neutrons get absorbed very well in the Cd-foil, see Fig. 2.11. Therefore, this so called Cd-covered neutron activation leads to the epithermal and fast flux in the beam.

However, for the calculation of the mean according to Eq. (4.3) one has to know the neutron spectrum that is responsible for the activation process, i.e. the spectrum which has been modified by the Cd-coverage, to determine the epithermal and fast neutron flux correctly.

Therefore the effect of the Cd-foil on the spectrum of the neutron beam can be obtained by multiplying the transmission function of the Cd-foil with the neutron spectrum

$$\Phi_{Cd}(E) = \Phi_{\text{TRIGA}}(E) T_{WB} T_{Cd}$$

with

$$T_{Cd}(E) = e^{-\Sigma_{Cd,abs}(E)d}$$

and

$$\Sigma_{Cd,abs}(E) = \sigma_{Cd,abs}(E) \frac{N_A \rho}{A_u} \, .$$

	d [cm]	m[g]	A[s^{-1}]	error[%]	t_{irr}[s]	t_{inter}[s]
not covered	30	0.2879	5.76	1.70	1800	900
2 mm Cd cover	30	0.2940	0.227	4.95	9000	1145

Tab. 4.4.: Gold foil activation without and with 2 mm Cd-foil [73].

Calculating the weighted absorption cross section for this modified spectrum leads to

$$\overline{\sigma}_{\text{abs,Cd}} = 46.42\,\text{b}.$$

Since the thermal neutrons are now filtered out by the Cd-foil the spectrum is now much harder leading to a lower weighted absorption cross section for gold.

4.2.4. Measurements

These flux measurements (and many others) of the new facility were done in collaboration with Manuel Pangl. Their results can be found in great detail in his diploma thesis [73]. For his calculations, Pangl used $\sigma_{abs,2200}$ for first approximations of the neutron flux because the exact neutron spectrum was yet not fully developed then. Now, with the knowledge of the neutron spectrum these preliminary results can be updated.

Using the data from Tab. 4.4 to calculate the neutron flux with Eq. (4.2) yields total neutron flux value of

$$\Phi_{total} = (2.90 \pm 0.10) \times 10^6 \text{cm}^{-2}\,\text{s}^{-1}$$

and an epithermal and fast neutron flux of

$$\Phi_{epi,fast} = (2.33 \pm 0.48) \times 10^4 \text{cm}^{-2}\,\text{s}^{-1}\ .$$

From the difference of these two flux values the thermal neutron flux follows immediately as

$$\Phi_{thermal} = (2.88 \pm 0.1) \times 10^6 \text{cm}^{-2}\,\text{s}^{-1}\ .$$

The relative fraction of epithermal and fast neutrons is found as

$$\frac{\Phi_{epi,fast}}{\Phi_{total}} = 0.008 \pm 0.0016\ ,$$

which is equivalent to a Cd-ratio of 124.

4.3. Neutron beam geometry measurements

For several experiments like neutron radiography or sample irradiation the homogeneity of the neutron beam is of interest. Therefore, a lot of effort was put in several measurements to characterize the homogeneity of the beam. Three different measurement techniques were used to characterize its homogeneity:
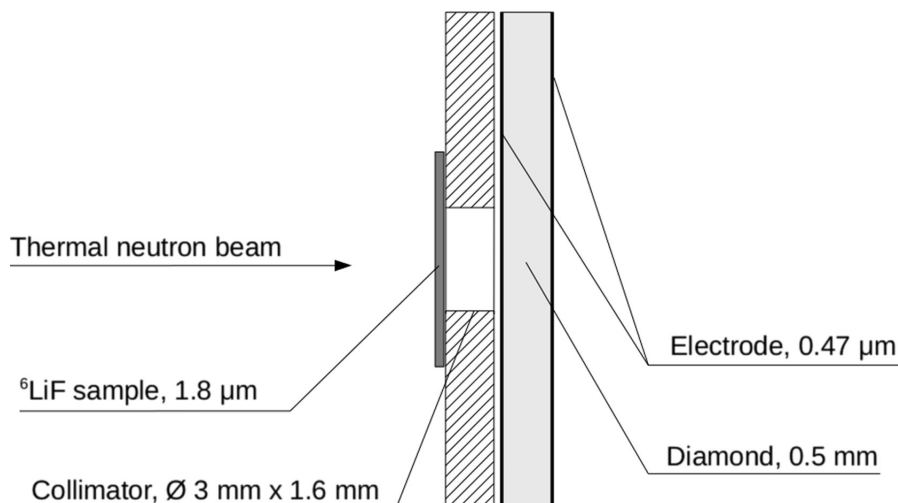
Fig. 4.5.: Scheme of a diamond detector [77].

- Image plates
- Diamond detectors
- Matrix of gold foils.

Image plates are a standard tool in neutron imaging [76]. They have a high dynamic range, high efficiency, high resolution ($\sim 25\,\mu m$), and a big active detector area. Moreover they are mechanically flexible and reusable.

On the surface of a plate, a neutron converter (e.g. Gd_2O_3) is mixed with photo-stimulated luminescence materials such as BaFBr:Eu. When an image with neutrons is taken, Gd emits an electron which excites the BaFBr:Eu-molecule to a metastable state. When this excited molecule is irradiated with laser light it is further excited, leading to luminescence of blue light which then can be detected with a photomultiplier tube. Scanning the whole image plate with the laser beam leads to the image.

Diamond detectors[2] are widely used as beam monitors and particle counters, particularly in high irradiation environments [77]. They consist of a diamond single-crystal ($\varnothing \sim 3\,mm$), a converter foil (e.g. LiF) in front of the diamond, and electrodes to apply a high electric field, as it is shown in Fig. 4.5. In the converter foil the neutron creates an α- and a tritium-particle which produce electron-hole-pairs in the crystal. In combination with an electric field of about $1\,V\,\mu m^{-1}$ these free charge carriers produce tiny current pulses. Analyzing the pulse shape with an advanced hardware/software combination [78] allows to distinguish between neutrons, charged particles, and γ-radiation.

This type of detector was installed on a 2D-scanning table to scan the beam profile.

All the experiments with diamond detectors, image plates, and Au-foils have revealed that the beam is homogeneous over the whole beam area. The result of the image plate measurement is shown in Fig. 4.6. While Fig. 4.6 a shows the raw data from the image plate, in Fig. 4.6 b a horizontal profile is plotted. Only a slight, statistically not significant decrease in the neutron flux might be visible.

---

[2]Special thanks to Christina Weiss, Pavel Kavrigin and Erich Griesmayer from Cividec GmbH!

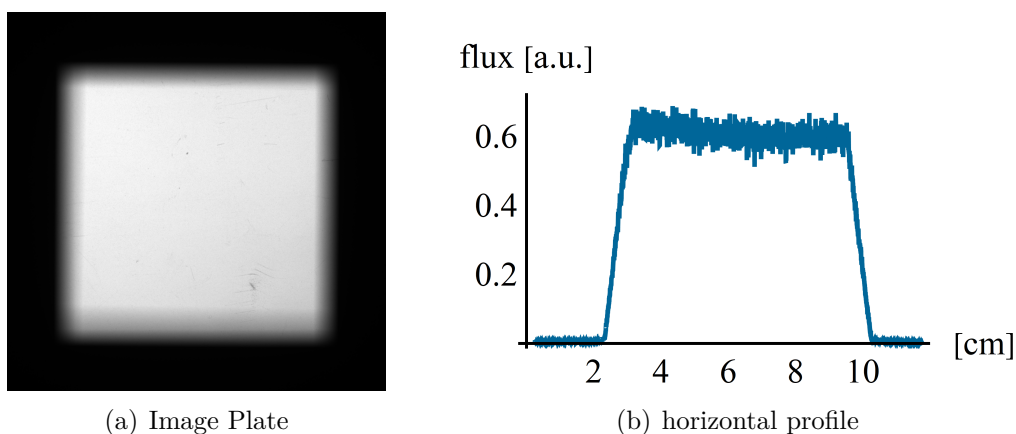(a) Image Plate

(b) horizontal profile

Fig. 4.6.: Neutron beam profile at the beamport at a distance of $30\,cm$ from the beamport wall, measured with an image plate. It can be seen that the neutron flux is fairly homogeneous.

The same result can be seen in Fig. 4.7 where the results of the Au-foil flux measurements with rather bulky foils ($\varnothing$=21 mm) at the beamport and at the beamstop are shown. Again, the center of the neutron beam has got a homogeneous flux. Only the shoulders are rather asymmetrical, possibly due to removable collimators which are mounted in the wall between experimental chamber and pre-chamber which might not be full in axis with the beamtube of the reactor. Nevertheless, the central beam of 65×65mm^2 has got a homogeneous neutron flux.

The measurements with the diamond detector led to the same results but with less statistical significance due to their rather low detection efficiency for thermal neutrons [73].

Since the measurement at the beamstop was done without collimator in the intermediate wall, Fig. 4.7 shows the biggest beam cross section that is possible with the new facility. Depending on the homogeneity requirements the realistically usable cross section is about 250×250mm^2.

4.3.1. Beam divergence measurements

To test the quality of the model geometry and the beam preparation in MCNP, the divergence of the neutron beam in the simulation was compared with the divergence of the real neutron beam.

For this, the width of the beam was measured at the beamport and at the beamstop. The edge of the beam was defined at the point where the flux drops to a tenth. Then, the divergence angle α can be easily defined as

$$\alpha = \tan^{-1}\left(\frac{b-a}{2l}\right)$$

where a is the beam width at the beamport, b is the width at the beamstop and l is the distance between these two locations.
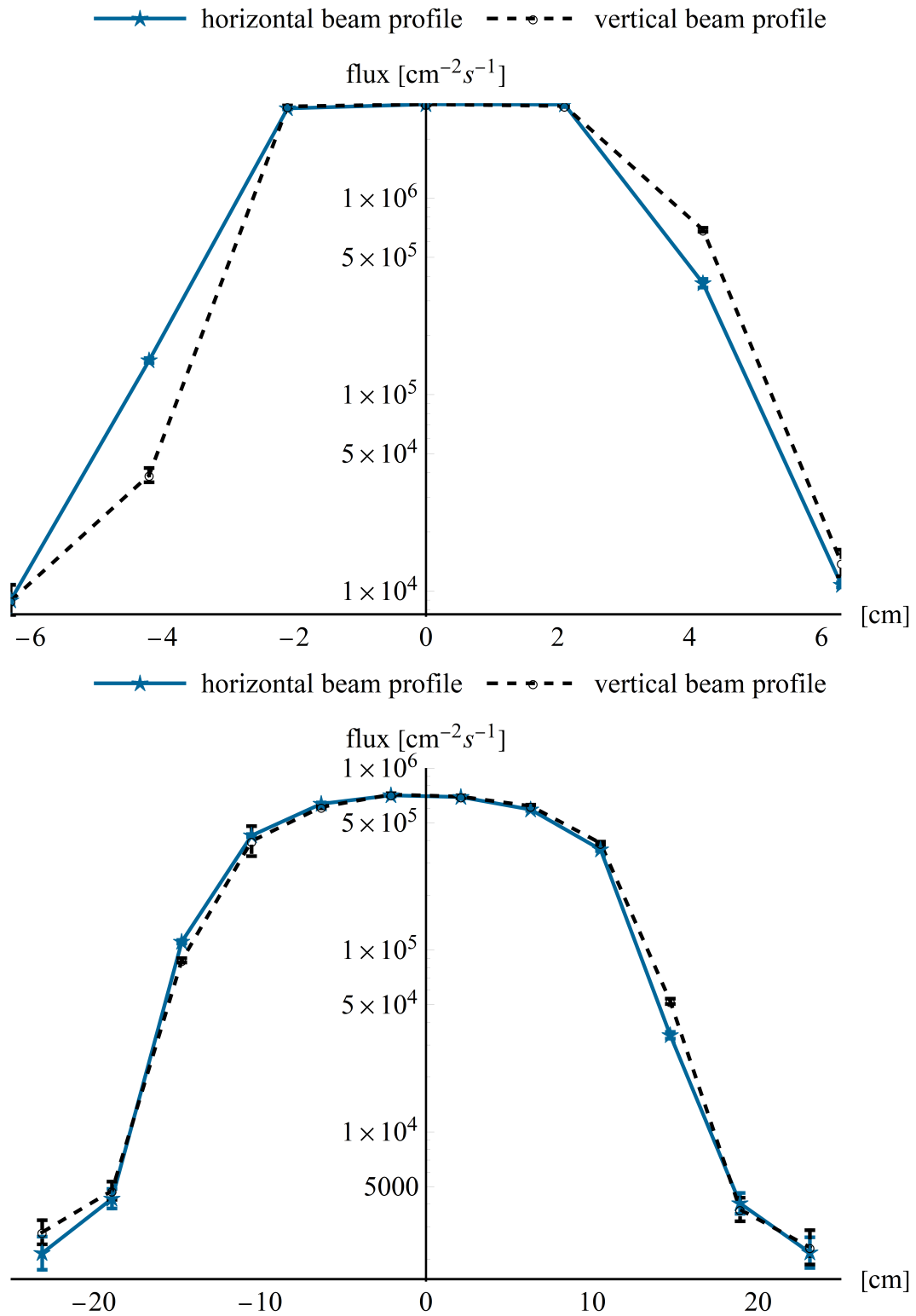
Fig. 4.7.: Horizontal and vertical beam profile measured at the beamport (5 cm away from the beamport wall, with 65×65mm^2-collimator installed) and at the beamstop (250 cm away from the beamport wall, without collimator installed), measured with a matrix of gold foils.
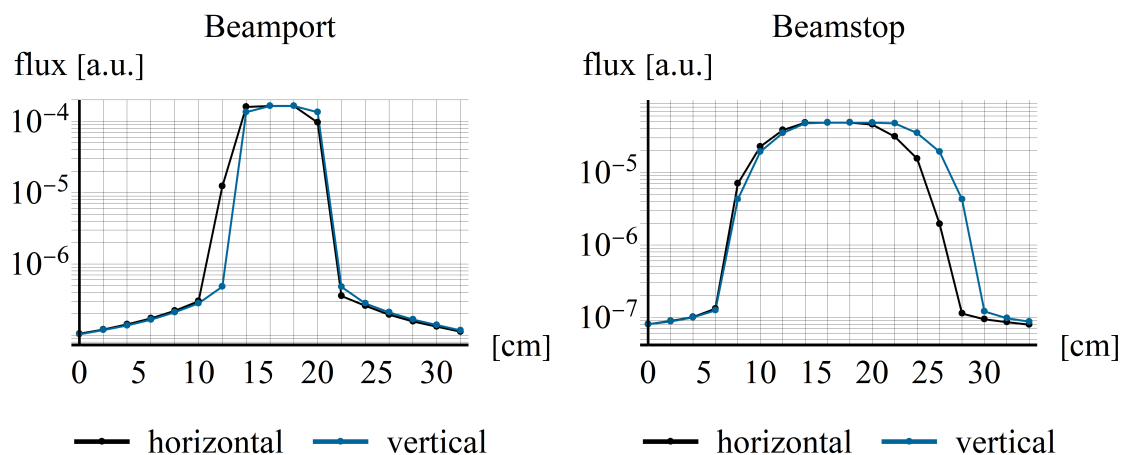
Fig. 4.8.: Neutron beam profile at a distance of (30 cm from the beamport wall), and next to the beamstop (240 cm away from the beamport wall) simulated in MCNP6. Error bars are smaller than the symbols.

	width	error
a_{hor}	9.7 cm	5 %
a_{ver}	9.6 cm	5 %
b_{hor}	18.6 cm	5 %
b_{vert}	18.8 cm	5 %

Tab. 4.5.: Horizontal and vertical width of the neutron beam at the beamport and the beamstop simulated in MCNP.

These lengths were extracted from MCNP6 (see Tab. 4.5 and Fig. 4.8) to calculate the beam divergence α, leading to

$$\alpha_{hor} = 1.21° \pm 0.14°$$

$$\alpha_{vert} = 1.39° \pm 0.15°$$

which is in good agreement with the experimental value of 1.3° [73] that in turn is equivalent to a L/D-value of 44.

4.4. Flux spectrum analysis

Certainly the most interesting part of the spectrum of the new facility is the thermal regime. Since the expected Maxwell-Boltzmann flux distribution of beamtube B (see Fig. 2.4) is modified by the installed filters (see Chapter 2.3), the effectively transmitted spectrum had to be measured carefully to see any deviations from the predicted one.

Therefore, some time-of-flight (TOF) measurements were performed which shall be described the next few pages. While for monochromatic/dichromatic beams only the time structure is of interest [18], for the measurement of the spectrum of polychromatic beams detailed knowledge of the relative intensity of each wavelength

is of importance. There, in contrast to the case of a monochromatic beam some subtle effects, as e.g. the wavelength dependence of the detector efficiency, have to be taken into account which may cause for instance a shift of the spectral maximum.

4.4.1. Basics of time-of-flight experiments

Energy, wavelength, and velocity of neutrons are connected via the relations (2.3). Since for thermal neutrons the velocity is in the range of $1000\,\mathrm{m\,s^{-1}}$ to $10\,000\,\mathrm{m\,s^{-1}}$, their flight time for a typical flight path lengths l_{TOF} of $1\,\mathrm{m}$ to $5\,\mathrm{m}$ is in the ms regime and thus can be measured easily by chopping the continuous beam periodically into short pulses.

For these TOF experiments we have used a small Fermi chopper, consisting of a stack of several sheets of aluminum and cadmium rotating with $50\,\mathrm{Hz}$. When the stack is aligned parallel to the neutron beam the neutrons can pass through the aluminum sheets whereas otherwise they are blocked. The rotation of the stack delivers two neutron pulses per revolution resulting in a pulse repetition rate of $100\,\mathrm{Hz}$. Using a thin ^{3}He detector (inner diameter: 21.2 mm, pressure: 4 bar) that was placed orthogonal to the beam at a distance of l_{TOF}=240 cm from the chopper exit the time-of-flight of each neutron packet was analyzed by means of a LABVIEW®-controlled multi-channel computer interface with 2 µs channel width. A small Cd-diaphragm of about 2 mm width and 30 mm height was inserted front of the cylindrically shaped detector in order to have a well defined effective detection thickness.

In principal, this kind of measurement works both for monochromatic and polychromatic neutrons. However, for polychromatic neutrons some effects have to be taken into account which influence the measured TOF-spectrum.

The effects which had to be taken into account are:

Chopper timing offset Δt - The chopper we have used has a built-in photo sensor which delivers a TTL signal to start the time-of-flight analyzer when the chopper opens for neutrons to pass through. This sensor has a constant but unknown timing offset relative to the actual chopper opening which has to be measured prior to the actual experiments.

Chopper opening function $C(t)$ - The finite opening time interval of the chopper leads to a convolution of its opening function with the neutron spectrum. However, in the case of our Fermi chopper this is just a small correction. Generally, the effective opening function $C(t)$ of neutron choppers can often be approximated either as a Dirac delta function $\delta(t)$, triangular function $\wedge(t)$, rectangular function $\sqcap(t)$, or trapezoidal function.

Detector efficiency - the absorption cross section of ^{3}He that is used as detection gas in the counter is velocity-dependent leading to a likewise velocity dependent detector efficiency. This is clearly the major correction to be taken into account.

Absorption in air and aluminum - along their flight path the neutrons have to travel through air and the aluminum sheets of the chopper. Again, the
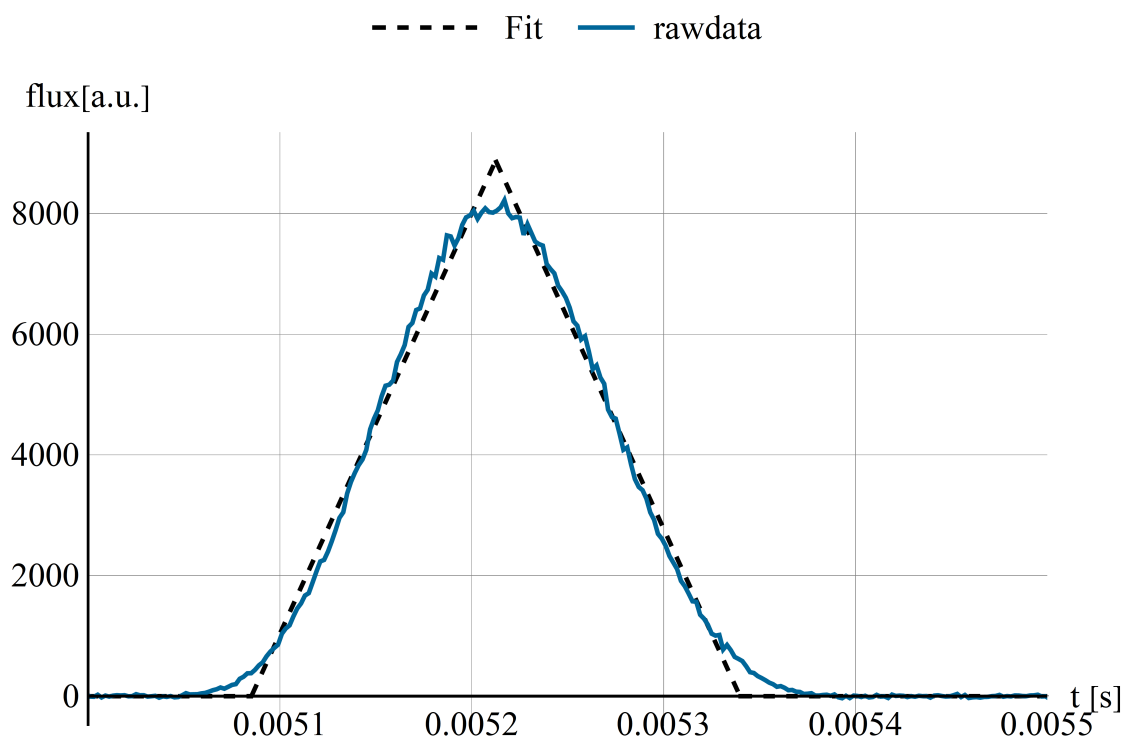
Fig. 4.9.: Measured raw data of the Fermi-chopper used in our TOF experiments and a fit of a triangular function $\wedge(t)$ for its opening function $C(t)$ from which Δt and t_{open} could be calculated.

velocity-dependent absorption cross section effect shifts the spectrum a bit. This is only a very small correction, however.

All these corrections where applied on the thermal neutron spectrum derived in Chap. 2 and compared with the measured raw data. To measure the timing offset and the opening function of the chopper, measurements were done on two dichromatic beamlines of the reactor. These measurements were used also to find out the two wavelengths of those neutron beams.

The chopper timing offset & opening function

Since real choppers do not open and close the neutron beam instantly but with some time distribution, the starting time of the neutron pulses is not well defined. Thus, the measured signal is blurred. In fact, the measured TOF-spectrum $\Phi_{meas}(t)$ is a convolution of the real TOF-spectrum $\Phi(t)$ with the chopper opening function $C(t)$

$$\Phi_{meas}(t) = \Phi(t) * C(t) \ .$$

The chopper opening function depends on *how* the chopper chops the beam. Since before the experiment the inner structure of the chopper was not clear, it was dismounted to study its build-up which is documented in Fig. A.2. For most chopper systems like the one used here a loose aperture is moved across a fixed one. The opening function $\sqcap(t)$ of a slit aperture is a rectangular function, and the opening

function of two such slit apertures moving laterally against each other is just a convolution of two rectangular functions, leading to a triangular function $\wedge(t)$ [79]

$$\wedge(t) = \sqcap(t) * \sqcap(t) .$$

The chopper opening function was measured by mounting the neutron detector as close as possible to the neutron exit face of the chopper. By fitting a triangular function to the raw data of the measurement not only the opening function can be characterized but also the timing offset Δt and the opening time t_{open} can be extracted by the fit that is shown in Fig. 4.9.
It was found that

$$\Delta t = 5.0851 \pm 0.0001 \,\mathrm{ms}$$

and

$$t_{open} = 0.2547 \pm 0.0003 \,\mathrm{ms} ,$$

Additionally, it turned out that a triangular function fits very well to the opening function of our Fermi chopper, i.e.

$$C(t) \approx \wedge(t) .$$

These results are in excellent agreement with the theoretically expected values for $1\,\mathrm{mm}$ slit apertures rotating with $50\,\mathrm{Hz}$. Nevertheless it must be mentioned that these values depend on the experimental installation because even small variations in the alignment of the neutron beam axis with respect to the chopper cause a change of these values. Therefore, the timing offset must be carefully remeasured after every modification of the experimental setup. Furthermore, it must be mentioned that the timing values from above depend on the rotating frequency of the chopper. Since the $50\,\mathrm{Hz}$ frequency of an ordinary power socket is not really constant but always exhibits some fluctuations, the timing of the chopper is also not constant leading to measurements of unknown precision. Therefore, an electronically frequency-stabilized power supply for the chopper would be of advantage.

Detector efficiency

The ^{3}He-proportional counter which was used for our TOF experiment consists of a cylindrical cathode tube with an inner diameter of $21.2\,\mathrm{mm}$, filled with ^{3}He at a pressure of $4\,\mathrm{bar}$, and an electrically isolated thin anode wire stretched along its axis. For the given parameters of the experimental setup used for the measurement of the time-of-flight spectrum the rather small effective thickness causes an inaccuracy of the measured time-of-flight values of only 0.5%.
All types of such ^{3}He-gas-filled proportional counters have the same functional principle and utilize the ^{3}He(n, p)^{3}H reaction

$$^3\mathrm{He} + \,^1\mathrm{n} \to \,^3\mathrm{H} + \,^1\mathrm{p} + \,764 \,\mathrm{keV} ,$$
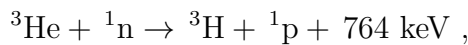
whose cross section exhibits a $1/v$-dependence up to about $200\,\mathrm{keV}$ and has a very large value of about $5400\,\mathrm{b}$ for thermal neutrons ($v = 2200\,\mathrm{ms^{-1}}$). Since the

reaction products proton and triton are charged they ionize the filling gas as they are slowed down and finally stopped, thereby producing secondary ionization charges, electrons and ions, which are accelerated towards the anode wire and the cathode wall, respectively, by applying a voltage of typically about (1 kV) between these two electrodes. In the immediate vicinity of the anode wire the electric field is rapidly increasing so that each of the secondary electrons produces further secondary electrons-ion pairs. This iterative process quickly leads to a charge avalanche, which can be registered easily by means of a charge-sensitive pre-amplifier. The ratio $A = N/N_0$ of the number N of finally produced free electrons to the number N_0 of fee electrons from the primary ionization process is called 'gas gain'. For proportional counters the gas gain is constant, i.e. the detected signal is proportional to the primary ionization, with values in the range $10^2 - 10^6$ depending on the fill-gas and on the *local* electric field conditions. At still higher values of A the proportionality get lost, since then photoionization by UV-photons following secondary ionization of inner shells is no longer negligible. Moreover, in this regime autonomous discharges may take place that are caused by electrons released when ions hit the cathode inner wall. In this context it is remarkable that ^{3}He-proportional counters, although operated mainly at rather low gas gains always require a small amount of a quench gas (usually CO_2) to avoid any breakdown due to either photionization or photoelectric effect on the cathode inner wall. The reason for this somewhat peculiar behavior is the occurrence of long-living (~ 10 ms) metastable states in the noble gas helium after radiation interactions, which may eventually trigger such breakdowns. Collisions with these heavier quench gas atoms deexcite these metastable states and prevent such breakdowns.

Taking into account the energy dependence of the neutron absorption cross section σ_{abs}, the corresponding energy dependence of the detector efficiency can be calculated by adapting Eq. (2.18) and using Eq. (2.19)

$$\epsilon(E) = 1 - e^{-\Sigma(E)d_{Det}} \ ,$$

with d_{Det} as effective detector thickness. In Fig. 4.10 the result of this calculation is shown for the ^{3}He-proportional counter used in the TOF experiment.

Absorption in air and aluminium

In the flight path of the neutrons is air and aluminum (inside of the rotating cylinder of the chopper). Again, absorption of neutrons in these materials is energy dependent and can also be calculated using Eq. (2.18)

$$\Theta(E) = e^{-\sum_i \Sigma_i(E)d_i}$$

for the i different materials in the beam. However, as it can be seen in Fig. 4.11 this is only a minor effect.

Detector saturation

The integral neutron flux of $> 10^6 \, \text{cm}^{-2}$ s at the new *Thermal White Neutron Beam* facility is higher than at all other beamlines of the TRIGA reactor. Whereas
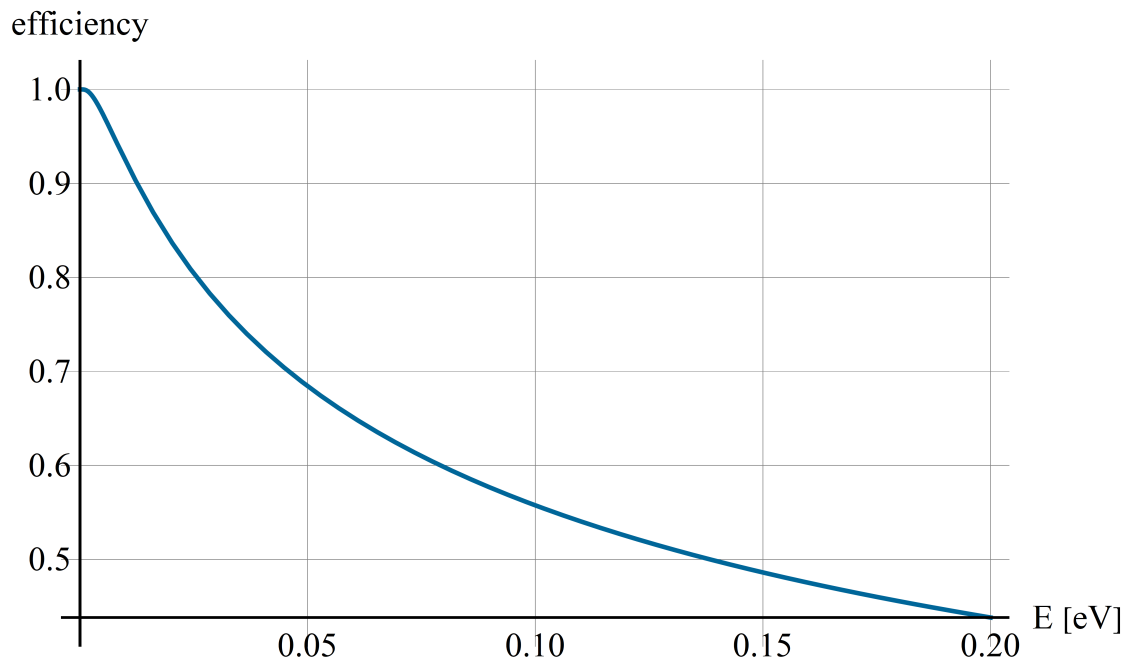
Fig. 4.10.: Efficiency of the ^{3}He-proportional counter tube with an effective diameter of 21.2 mm of the active volume and a gas pressure of 4 bar.
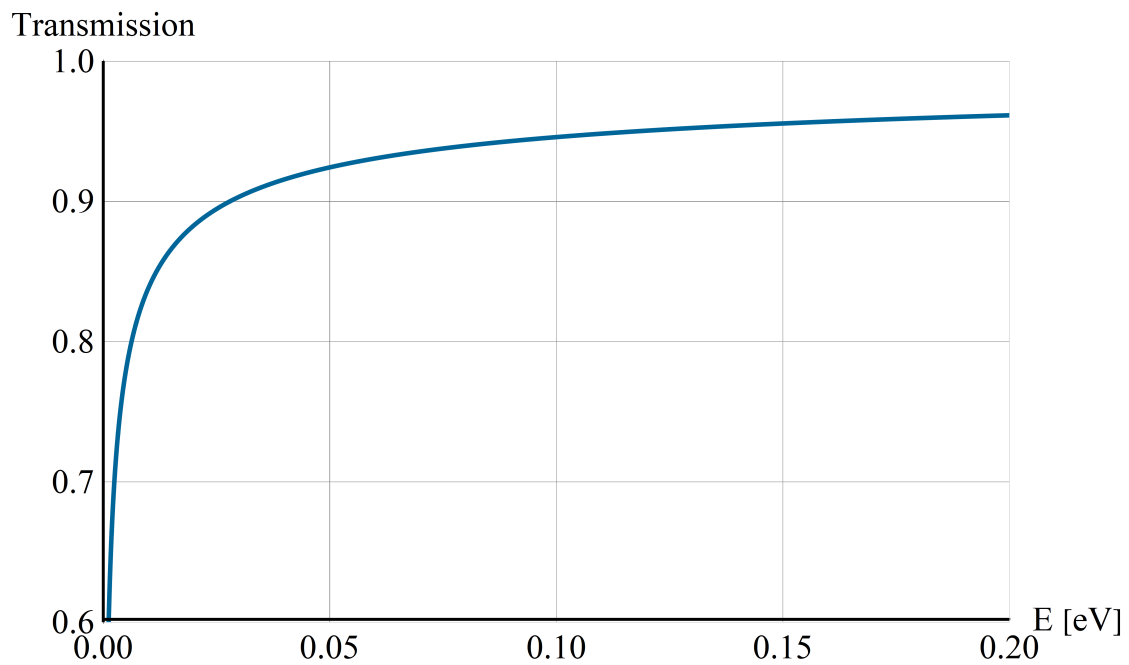

Fig. 4.11.: Transmission function of air and aluminum for the given conditions of the TOF-experiment.

without doubt neither the available hard- nor the software should have any problem to handle such a flux, it was not clear whether the detector can cope with it as well. Such a high flux is rather at the upper working limit of neutron proportional counters and therefore eventually might lead to dead-time induced saturation losses, which in turn would cause a distortion of the measured spectrum. Fortunately, this problem is somewhat relieved by the time-of-flight dispersion along the flight path from the chopper to the detector which distributes the integral intensity of each of the short neutron packages leaving the chopper over a larger time interval.

Since the distribution of the time intervals between two sequent neutrons is Poisson-distributed [80], the effect of the dead time τ of a detector can be corrected easily according to

$$n = \frac{m}{1 - m\tau} \ ,$$

where n is the real count rate, m is the measured count rate, and τ is the dead-time of the detector.

A series of experiments at different reactor power and with different cadmium apertures in front of the detector were performed to find out whether or not an eventual detector saturation affects the shape of the measured time-of-flight spectra. It was possible to vary the neutron flux over several orders of magnitude but not any deviation of the TOF-spectrum was found.

4.4.2. Measurements

For comparing the theoretical spectrum with the measured TOF-spectrum there are two possibilities: all corrections mentioned above can be applied to the experimentally measured spectrum, or the theoretical spectrum gets shifted by the corrections and the result is compared with the raw experimental data. In principle, both ways are correct. Since the correction of the chopper opening function $\wedge$ includes a convolution, it is more convenient to apply the corrections to the theoretical spectrum because then a deconvolution is avoided. In Fig. 4.12 the impact of the triangular chopper opening function $\wedge$, the detector efficiency ϵ, and the neutron absorption Θ in the flight path on the theoretical spectrum is shown.

Since the width of the opening function of the chopper is very short compared to the length of the time-of-flight spectrum, the correction $\wedge$ can be neglected. Likewise the correction of the neutron absorption in the flight path Θ is negligible. However, an absolute must is the correction of the detector efficiency ϵ which shifts the spectrum clearly.

In Fig. 4.13 the corrected theoretical spectrum is compared with the ideal Maxwell-Boltzmann distributed spectrum of the TRIGA reactor and with the raw data of the TOF measurement. The corrected theoretical spectrum fits very well to the experimental raw data. In particular the maximum of the theoretical curve coincides exactly with that of the measured spectrum. It can be clearly seen that, as expected, the sapphire/bismuth-filter installed in beamtube B partly blocks the higher energetic portion of the Maxwell-Boltzmann spectrum in the thermal region. This can be interpreted simply as a shift of the thermal spectrum towards the colder energy regime. Furthermore, obviously some imperfections of the filter set cause residual Bragg-scattering which leads to dips in the observed energy
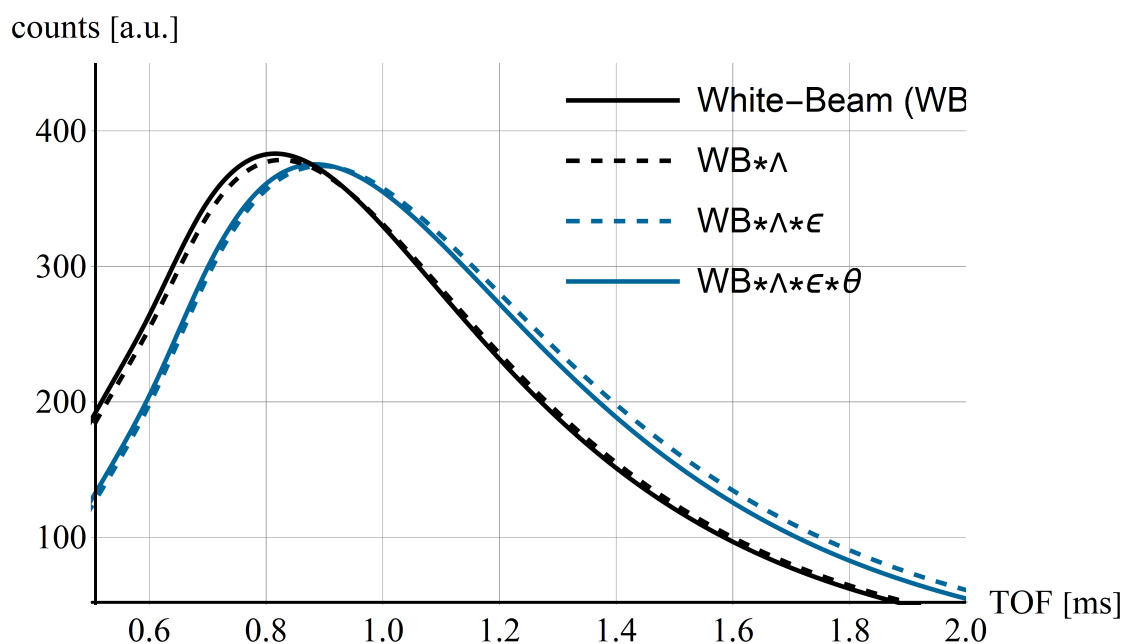
Fig. 4.12.: The impact of the corrections of the triangular chopper opening function $\wedge(t)$, the detector efficiency ϵ, and the absorption of neutrons Θ in the flight path is shown. Clearly the biggest shift is caused by the hence most important correction of the detector efficiency ϵ.
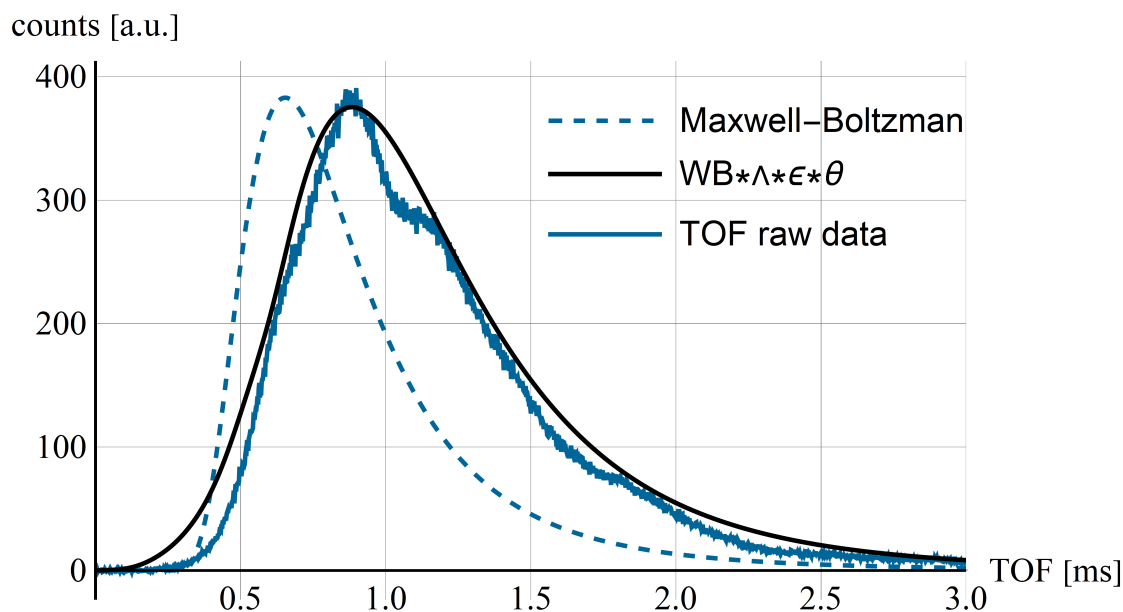

Fig. 4.13.: Comparison of the corrected spectrum of the white beam with the ideal Maxwell-Boltzmann distributed spectrum of the TRIGA reactor and the TOF raw data. The maxima of the corrected theoretical curve and the measured spectrum coincide perfectly. The dips at the slope of the measured spectrum are very likely due to residual Bragg-scattering of the sapphire/bismuth filters.

spectrum (see Fig. 4.13). However, these dips do not impose any problem for users since their positions are well known and reproducible. Therefore they can be taken into account easily in the evaluation of any kind of experimental data.

Time-of-flight experiments are a well-established standard technique in neutron physics. The required corrections are well known, simple, and often even negligible. Indeed, the good agreement of the shape of the measured wavelength spectrum with the theoretical predictions is a really satisfying result since this spectrum is of outstanding importance for any kind of future experiments to be performed at the *Thermal White Neutron Beam* facility.

4.5. Estimation of the facility's activation

Before constructing the biological shielding of the facility thoughts were given on the final disposal of the used materials at the end of their lifetime. To keep the future decommissioning process simple and cheap, activation of all utilized materials shall be kept as low as reasonably achievable (ALARA-principle).

By calculating the saturation activity A_{sat} it is possible to estimate the activity of the isotopes used for the facility after neutron irradiation with flux Φ for a period t. By utilizing only elements with a low saturation activity for the radiation shielding it is possible to avoid radioactive waste. To achieve this goal only elements with a small absorption cross section σ_{abs} and either a short (smaller than several days) or a very long half-life (greater than thousands of years) have to be used.

The expected activity A of a sample can be calculated using the relation

$$A = \sigma_{abs}\Phi\frac{m}{n}N_A(1 - e^{-\lambda t}) \ .$$

For $t \to \infty$, this leads to

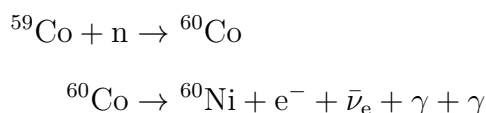$$A_{sat} = \sigma_{abs}\Phi\frac{m}{A_u}N_A \ , \tag{4.4}$$

where σ_{abs} is the absorption cross section, m is the mass, and A_u is the atomic mass of a given element. N_A is Avogadro's constant and Φ is the neutron flux. Thus, A_{sat} defines the expected maximum activity of a given amount m of an element after an infinite time of neutron irradiation with flux Φ. Apparently, this is the estimation of the worst-case scenario.

The biological shielding is made of two components: concrete and construction steel for reinforcement. The concrete itself contains the elements H, B, C, O, Na, Mg, Al, Si, K, Ca, Mn, and Fe (see Appendix A.2). All these elements will not lead to radioactive waste because the boron doping leads to a low thermal neutron flux within the shielding concrete. Apart from that their absorption cross sections and the half-lifes are low.

The construction steel (BST 550 M550) that has been used is a low-alloy steel whose major components are Fe and C. However, construction steel is not defined via its exact alloy composition but only by its mechanical properties. The exact alloy composition depends on the specific production conditions of the respective steel mill and is therefore unknown.

The most important alloy elements for steel are B, C, N, Al, Si, Ti, V, Cr, Mn, Co, Ni, Cu, Nb, Mo, Ta, and W. For the expected neutron flux all these elements with the exception of Co are irrelevant from a neutron activation point of view. Only Co exhibits aggravating physical properties: the absorption cross section of ^{59}Co is quite high ($\sigma_{abs} = 37.18\,\mathrm{b}$) and the half-life of ^{60}Co of about 5.27 years is neither short nor very long, and the two emitted γ-photons accompanying its β-decay to ^{60}Ni have high energies of 1.17 MeV and 1.33 MeV, respectively:

$$^{59}\mathrm{Co} + \mathrm{n} \rightarrow {}^{60}\mathrm{Co}$$

$$^{60}\mathrm{Co} \rightarrow {}^{60}\mathrm{Ni} + \mathrm{e}^- + \bar{\nu}_\mathrm{e} + \gamma + \gamma$$

Since the saturation activity depends on the initial ^{59}Co content of the steel, it has to measured carefully.

4.5.1. Cobalt content measurements

Since the alloy composition of construction steel is not standardized and hence unknown, attention had to be given to possible Co-traces. For this, samples of the construction steel were taken before the production of the biological shielding have started.

The first idea was to perform an X-ray analysis of these steel samples. Unfortunately this was not successful because the energy difference of the K_α and K_β lines of Fe and 27 is indistinguishable small.

The second idea was to use neutron activation analysis. However, this idea was refused also after talking to experts of neutron activation analysis from the Atominstitut [81] because the γ-background of Fe would be much higher than the expected signal of the Co-trace.

The third attempt was successful: the concentration of Co was measured by means of an inductively coupled plasma mass spectrometer (ICP-MS) that is available at the Atominstitut.

For this, sample steel parts were dissolved in 37% concentrated hydrochloric acid (HCl) in order to produce a solvent which can be analyzed by ICP-MS. All stoichiometric properties were measured during the production of the liquid sample. The ICP mass spectrometer's sensitivity to Co was gauged using a Co-sample of known concentration. A background reference measurement was provided by analyzing the Co-signal of triply distilled water.

After a simple stoichiometric calculation the Co-contents of the two samples were found to be $5.13 \times 10^{-3}\,\mathrm{w\%}$ and $2.06 \times 10^{-3}\,\mathrm{w\%}$, respectively.

Using Eq. (4.4) with a conservative estimation for the neutron flux on the inner surface of the biological shielding of $\Phi = 10^3\,\mathrm{cm}^2\,\mathrm{s}^{-1}$ (taken from MCNP simulations) leads to a specific saturation activity of ^{60}Co of less than $0.02\,\mathrm{Bq\,g}^{-1}$. This specific activity is much lower than the legal limit of the Austrian radiation protection regulation ('Strahlenschutzverordnung') [33] which is $0.1\,\mathrm{Bq\,g}^{-1}$ for ^{60}Co for non-constraining approval for solids and liquids ('uneingeschränkte Freigabe von festen Stoffen und Flüssigkeiten'). This simple estimation shows that the biological shielding is going to be regular demolition waste but not radioactive waste at the

end of its life-time. This result makes future decommissioning easier and much cheaper.

Boron steel apertures

Inside of beamtube B an insert was installed for proper positioning of the neutron filters and for defining the beam cross section, see Fig. 4.15. Both on the front (directed towards the reactor core) and the rear side of this *beamtube insert* an aperture made of boron steel was mounted. Since the neutron flux at the position of the front aperture is in the order of $10^9 \, \text{cm}^{-2} \, \text{s}^{-1}$ [42], attention had to be given to avoid excessive activation of these apertures. Therefore the respective front side of each aperture was covered with 2 mm cadmium to reduce the thermal neutron flux inside of the material by about six orders of magnitude.
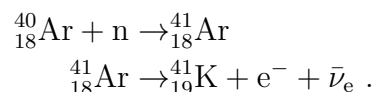
Contrary to construction steel alloy, the steel that is used for the apertures (Böhler Neutronit® A976SF) is well defined: it is made of Fe, C, Cr, Ni, and B, with very little content of cobalt (see Tab. 4.6). Except of cobalt all these elements have a low absorption cross section and their daughter products after an eventual neutron activation have short half-lifes. Moreover, the boron content of the apertures will further reduce the thermal neutron flux significantly. Thus, the apertures will hardly become activated and therefore will not be an essential source of radioactive waste.

	C	Cr	Ni	Co	B
Alloy A976SF	0.03%	19.1%	12.7%	<0.05%	1.8%

Tab. 4.6.: The components of the steel alloy used for the neutron beam apertures inside the beamtube. The front side of each aperture, which is directed towards the reactor core, is covered with 2 mm of cadmium to avoid excessive neutron activation.

4.5.2. Air activation

Not only the shielding materials can be activated by neutron radiation but also the air in the interior of the shielding chamber. The most prominent components of air are N, O, Ar, and water vapor. However, only Ar can be activated in noteworthy quantities

$$^{40}_{18}\text{Ar} + \text{n} \rightarrow \, ^{41}_{18}\text{Ar}$$
$$^{41}_{18}\text{Ar} \rightarrow \, ^{41}_{19}\text{K} + \text{e}^- + \bar{\nu}_{\text{e}} \, .$$

^{40}Ar has an absorption cross section σ_{abs} of 0.68 b and ^{41}Ar has a half life of 109 minutes. The activation of ^{40}Ar is the reason why at all beamtubes of the reactor a special ventilation system is installed.

In order to estimate the prospected saturation activity A_{sat} of ^{41}Ar inside the shielding chamber the neutron flux has to be known. MCNP-simulations show that

Fig. 4.14.: The beamtube insert right before installation. Dimensions to be found in Appendix A.4. Special thanks to Andreas Musilek, Mario Villa, Ernst Klapfer and Robert Bergmann (as seen from left to right)!
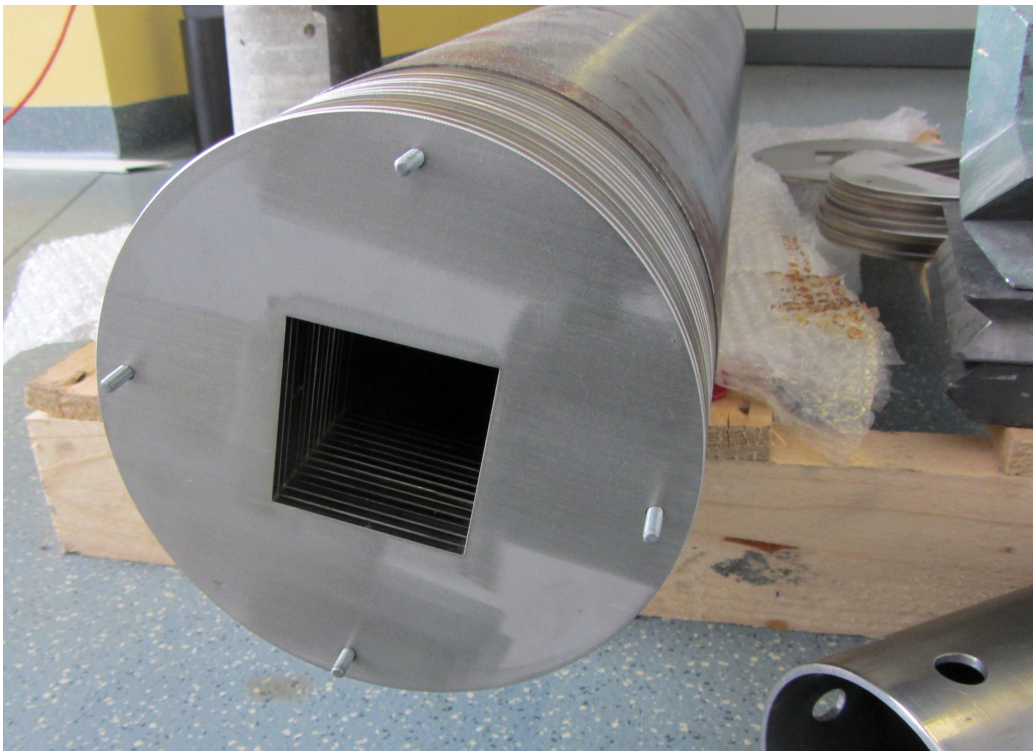

Fig. 4.15.: The beamtube insert with mounted boron steel apertures for beam definition. The 2 mm Cd-shielding of the aperture was installed after taking the picture. Dimensions of the aperture, see Appendix A.4.

the neutron flux is about $10^7\,\mathrm{cm^{-2}\,s^{-1}}$ in the beam and about $10^4\,\mathrm{cm^{-2}\,s^{-1}}$ outside of the beam (see Tab. 4.7).

	beam	off-beam
flux Φ	$10^7\,\mathrm{cm^{-2}\,s^{-1}}$	$10^4\,\mathrm{cm^{-2}\,s^{-1}}$
volume	$0.013\,\mathrm{m^3}$	$0.013\,\mathrm{m^3}$
mass of Ar	$0.22\,\mathrm{g}$	$312\,\mathrm{g}$

Tab. 4.7.: Physical properties to estimate the ^{40}Ar activation [34, 35, 64].

Using Eq. (4.4) leads to a total specific saturation activity of $2.9\,\mathrm{kBq\,m^{-3}}$. Converting the specific saturation activity to a specific dose rate by using the factor

$$1\,\mathrm{Bq\,m^{-3}} = 2.2 \times 10^{-4}\,\mathrm{\mu Sv\,h^{-1}}$$

which can be found in [82], leads to a total specific saturation dose rate of $0.6\,\mathrm{\mu Sv\,h^{-1}}$ generated by ^{40}Ar activation. Although this dose rate is quite low, a ventilation system was installed nevertheless because of radiation protection and workplace regulations. This ventilation system is connected to the ventilation thread A ('Abluftstrang A') where also the exhaust airstreams of the reactor, the beamtubes, and the 'dry irradiation room' ('Trockenbestrahlungsraum') are merged and discharged to atmosphere after cleaning in a multi-level filter system.

4.6. First tests of a Laue-Bragg-camera

For the purpose of filtering out both fast neutrons and reactor γ-radiation a sapphire and a bismuth crystal were bought. Whereas for the sapphire crystal there was a priori no doubt that is a single crystal, it had to be verified that the bismuth crystal is indeed monocrystalline before it could be mounted in beamtube B of the reactor. This was done by installing a 'quick and dirty' Laue-Bragg-Camera setup within the shielding chamber of the new facility (see Fig. 4.16). The crystal was also tested with an X-ray Laue-Bragg-Camera[3] in order to compare the results of both measurements. While with neutrons the main structure can be recognized from the (few) visible reflections (Fig. 4.17), X-ray radiation did not reveal any reflection (Fig. 4.18). X-ray radiation emitted by a Cu-anode ($\sim 1.54\,\text{Å}$) can only penetrate the upper surface layer ($\sim 8\,\mathrm{\mu m}$) of the material with high atomic number (Z=83) while neutrons penetrate the whole bulky crystal. The obvious conclusion is that the crystal structure of the surface layer must have been destroyed by cutting and polishing the crystal.

A further measurement with X-rays of another Bi-crystal, borrowed temporarily from the Institute of Solid-state Physics, and a simulation of the Laue-Bragg diffraction pattern of monocrystalline bismuth (see Figs. 4.19 and 4.20) demonstrate that its crystal structure is very similar, indeed, to the structure of our own crystal as it was found with neutrons. Since the experimental setup was rather simple

---

[3]Special thanks to Klaudia Hradil (TU-X-ray center) and Andrej Prokofiev and Snezana Stojanovic from the Institute of Solid-state Physics of the TU for their support!

not visible:
30x30 mm² PE-collimator
Cd-aperture (d=2 mm)

Bi-crystal (l=50 mm, d=100 mm)
distance
crystal - Image Plate:
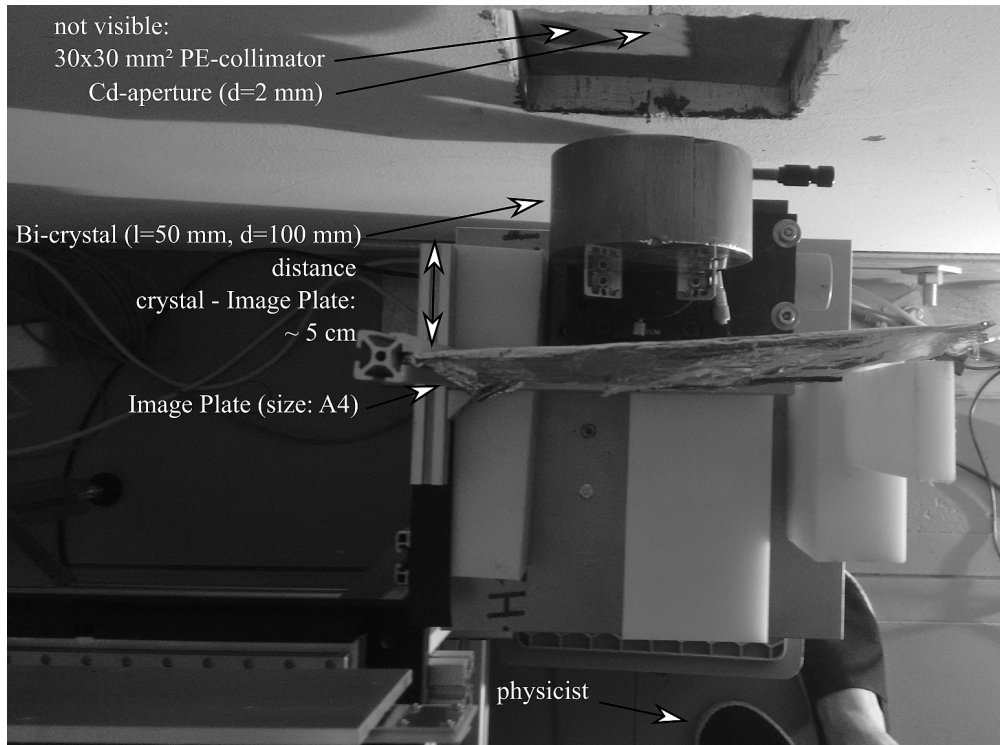~ 5 cm

Image Plate (size: A4)

physicist

Fig. 4.16.: Rough-and-ready experimental setup of a neutron Laue-Bragg-Camera
with an image plate detector to check whether the analyzed bismuth-
block is poly- or monocrystalline.

and the whole experiment took less than one day (with individual measurement
times of only one hour) this is a quite pleasant result. Likewise satisfying is the
fact that this first experiment demonstrates that it is easy to install quickly a new
experimental setup within the radiation shielding chamber of the *Thermal White
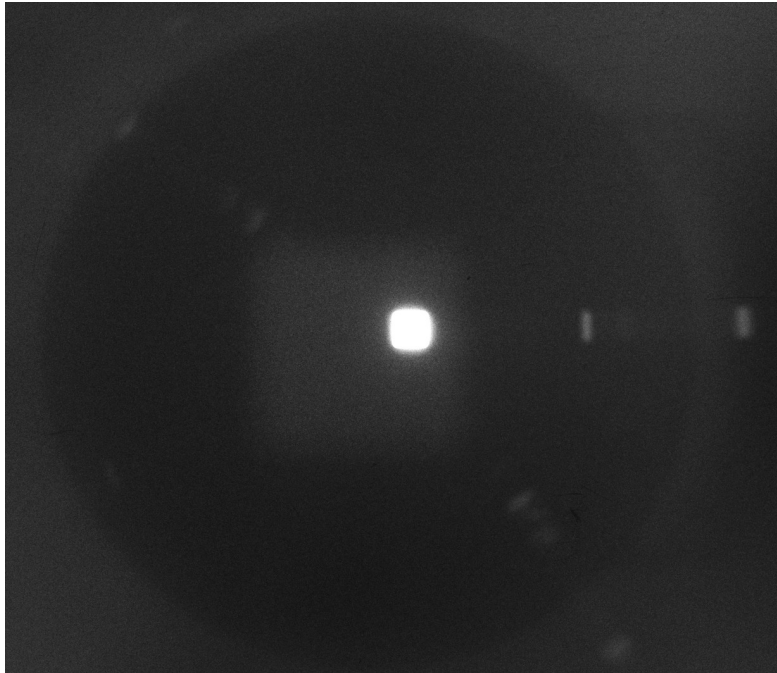Neutron Beam* facility.

Fig. 4.17.: The image taken with the Laue-Bragg-camera from Fig. 4.16. The white spot in the center is the transmitted beam, the other spots are Bragg-reflections from the Bi-crystal. The square in the center is from the pre-collimation system.
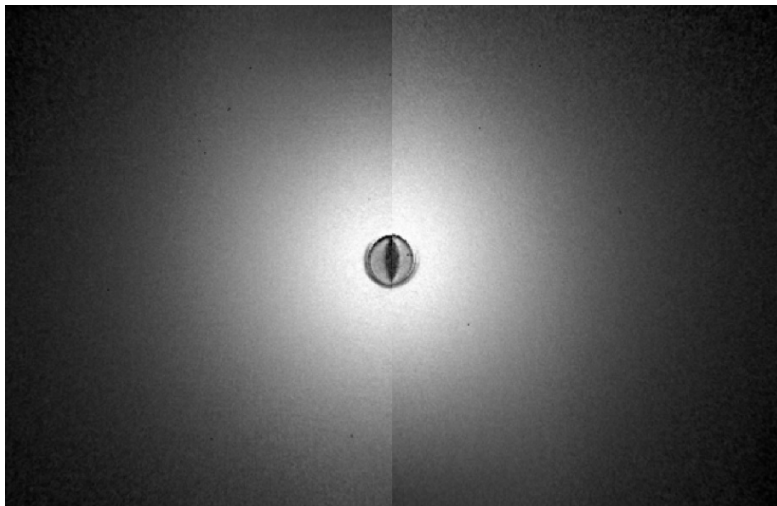

Fig. 4.18.: The same experiment done with X-ray radiation from a Cu-anode ($\sim 1.54\,\text{Å}$). No Bragg-reflections are visible.
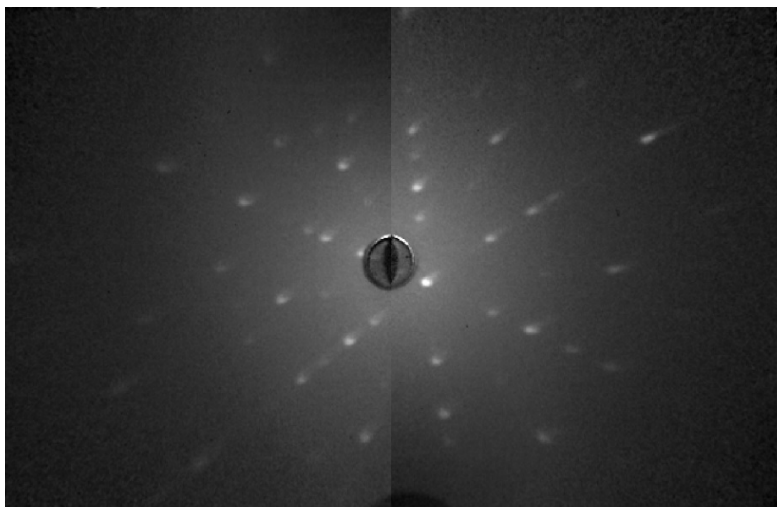
Fig. 4.19.: An X-ray Laue-Bragg image done on a very different Bi-single crystal for the purpose of comparison. The 6-fold symmetry of the rhombohedral crystal structure is well recognizable.
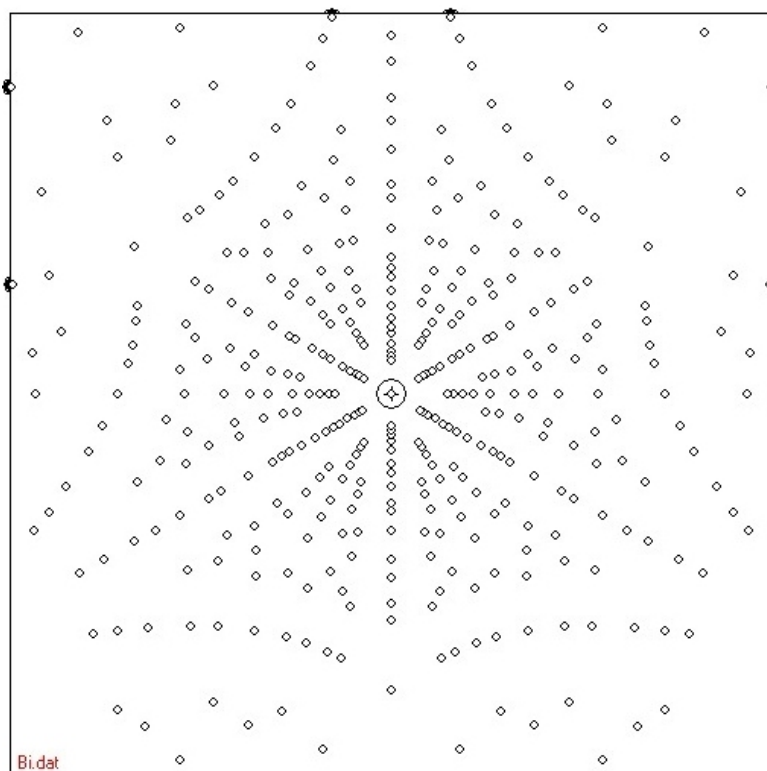

Fig. 4.20.: A simulation of the Laue-Bragg diffraction pattern of a bismuth single crystal.

5. The Neutron Resonator MONOPOL

W<small>HILE</small> the basic principle of spatial magnetic spin resonance was introduced in the 1960ies by Drabkin [15], the idea was extended by Badurek and Jericha at the beginning of the new millenium [13]. Several prototypes of a neutron spin resonator called MONOPOL (an acronym of **mono**chromatization and **pol**arization) have been developed to show the potential in this new concept [18]. The knowledge accumulated is currently merged into a new hardware concept of MONOPOL which will no longer remain in the prototype phase: after tests at the *Thermal White Neutron Beam* facility of the Atominstitut end of 2018 the resonator is going to be part of the PERC experiment at the FRM II reactor in Munich.

This chapter is dedicated exclusively to the neutron spin resonator MONOPOL. After a short general statement on polarized neutrons and a brief description of working principle of MONOPOL, in Section 5.3 one particular result of experiments with the most recent prototype of MONOPOL with very cold neutrons (VCN) at the Institute Laue-Langevin (ILL) is presented to illustrate its capabilities. While the new concept of the resonator for its use with thermal neutrons is presented in Section 5.4, the future of MONOPOL is outlined in Section 5.5.

At present, first measurements with a supermirror polarizer are ongoing at the *Thermal White Neutron Beam* facility to establish the basis for future experiments with polarized neutrons, in particular for those utilizing a MONOPOL-like device. These measurements will be presented in the last section of this chapter.

5.1. Polarized neutrons

As a fermion, each neutron has a spin vector $\vec{s}_n$. If an external magnetic field $\vec{B}$ (guiding field) is applied then there are only two possible orientations of the neutron's spin: parallel and anti-parallel to $\vec{B}$. The degree of polarization P of an ensemble of neutrons is defined as

$$P = \frac{N_+ - N_-}{N_+ + N_-} \ ,$$

where N_+ and N_- are the numbers of neutrons with spin-'up' and spin-'down', respectively. For a non-polarized neutron beam both numbers are equal, thus $P = 0$.

Polarized neutrons have become a standard tool in neutron physics with a broad range of applications both in applied sciences and in fundamental physics research. The neutron group at the Atominstitut currently uses polarized neutrons in many very different types of experiments, such as the qBOUNCE experiment [26], MONOPOL [20], USANSPOL [83], polarimetry experiments [84], or experiments on the neutron β-decay [3], to mention just a few arbitrary up-to-date examples.

Three different methods of polarizing a neutron beam, namely

- Bragg reflection at magnetic crystals
- Total reflection at polarizing supermirrors
- Polarized ^{3}He spin-filters

have turned out to be most relevant and therefore shall be described briefly.

Magnetic crystal Bragg reflection [85]: in a saturated magnetic crystals the total form factor is the sum of the form factors for nuclear scattering and for magnetic scattering

$$F_{\mathrm{tot}} = F_{\mathrm{nuc}} \pm F_{\mathrm{mag}} \ ,$$

where the signs refer to the two possible neutron spin states. If the nuclear and the magnetic form factors have the same size, i.e. $F_{\mathrm{nuc}} = F_{\mathrm{mag}}$, then for one spin state $F_{\mathrm{tot}} = 0$ there is no scattering at all whereas for the opposite spin orientation the scattering cross section is non-zero. Thus, Bragg reflection takes place only for one spin state and the - inevitably monochromatic - reflected beam gets fully polarized. However, only a few crystal materials are known which fulfill the necessary equality of nuclear and magnetic form factors almost exactly [86]. By far the most important and almost exclusively utilized is the (111)-reflection of so-called 'Heusler alloy' (Cu_2MnAl, $d_{111} = 3.453\,\text{Å}$) single crystals. Clearly, a polychromatic polarized neutron beam cannot be produced with this method and it is therefore no reasonable option for installation at the *Thermal White Neutron Beam* facility.

Total reflection at polarizing supermirrors: For magnetic materials the index of refraction for neutrons of wavelength λ is given as [86]

$$n = 1 - \lambda^2 \left(\frac{Nb_{\mathrm{coh}}}{2\pi} \mp \frac{m_{\mathrm{n}}\mu B}{h^2} \right) \ . \tag{5.1}$$

N is the particle density, b_{coh} the coherent nuclear scattering length, m_{n} the neutron mass, μ the neutron magnetic moment, B the saturation induction, and h Planck's constant. The first term in the bracket of Eq. (5.1) belongs to nuclear and the second term to magnetic scattering. One can see immediately that for one of the two spin states the index of refraction gets smaller than 1 ($n < 1$) if magnetic scattering exceeds nuclear scattering. Hence for this particular spin orientation the material is optically less dense than air, which implies that upon grazing incidence of the neutron beam on a flat surface at an angle that is less or equal to the critical angle θ_{crit}, which follows from

$$\cos\theta_{\mathrm{crit}} = n \ ,$$

total reflection will take place. Unfortunately, for thermal neutrons $|\,n - 1\,| \approx 10^{-5}$ and the critical angles are correspondingly low. It is worth to mention here that for most elements the purely nuclear neutron index of refraction is smaller than 1. Of all materials the (very expensive) isotope ^{58}Ni has the largest critical angle

$$\theta_{\mathrm{crit,Ni-58}} = 2\,\mathrm{mrad}\,\text{Å}^{-1} \ ,$$

which is to compare with that of natural nickel

$$\theta_{\text{crit,Ni−nat}} = 1.73 \, \text{mrad} \, \text{Å}^{-1} \; .$$

Polarizing supermirrors which have first been proposed by Mezei [87] consist of a stack of thin extremely flat glass plates, slightly bent to avoid direct transmission without and mirror reflection. Each of these plates is coated with hundreds of pairwise thin layers of magnetic and nonmagnetic material (ideally with opposite sign of their nuclear scattering lengths b_{coh}, like e.g. Co-Ti). A set of permanent magnets keeps the Co-layers at magnetic saturation. By stepwise increasing the layer thickness a quasi-continuum of 'pseudo-Bragg peaks' appears since each wavelength finds its appropriate layer spacing to fulfill the well-known condition for Bragg reflection. For angles exceeding the critical angle of total reflection the reflectivity of such a supermirror is, of course, not 100%, but for a broad range of thermal wavelength it reaches values of more than 90%. Hence it appears as if the critical glancing angle has been increased. Indeed, often the so-called 'm-value' of a supermirror is quoted which is defined as

$$\theta_{\text{crit}} = m \, \theta_{\text{crit,Ni−nat}}$$

and compares the critical angle of a given supermirror with that at a flat surface coated with natural nickel. Since the angular separation of the reflected neutrons from with opposite spin which fly straight ahead through the glass plate is very small, the rear side of each glass plate usually is coated with a strongly absorbing gadolinium layer.

At present supermirrors with m-values up to 8 are commercially available which are extremely expensive, however. Since supermirrors maintain their high reflectivity for all wavelengths above a certain lower limit they are able to polarize a white thermal beam as a whole. Fig. 5.1 shows the Co-Ti supermirror that we have used for the test measurement described in Section 5.6. It is not a state-of-the-art device, it was bought already about 20 years ago at a rather moderate price from the Institute of Nuclear Physics, Gatchina near St. Petersburg, it allows to polarize only a small beam and its m-value has never been defined by the manufacturer. Nevertheless it is of great scientific value, since many worldwide recognized experiments could be realized at the Atominstitut as well at the ILL Grenoble which would not have been possible without it usage.

Polarized ³He spin-filters: spin-polarized ³He has an extremely large neutron absorption cross section

$$\sigma_{\uparrow\downarrow} = 5925 \, \text{barn} \cdot \text{Å}/\lambda$$

if neutron and helium spin are antiparallel, whereas for parallel alignment no absorption but only potential scattering occurs with a very low cross section

$$\sigma_{\text{scatt},\uparrow\uparrow} \approx 5 \, \text{barn} \; .$$

³He can be polarized to a degree of typically up to 80% by using either of two optical pumping methods, 'Metastability Exchange Optical Pumping' (MEOP) [88]
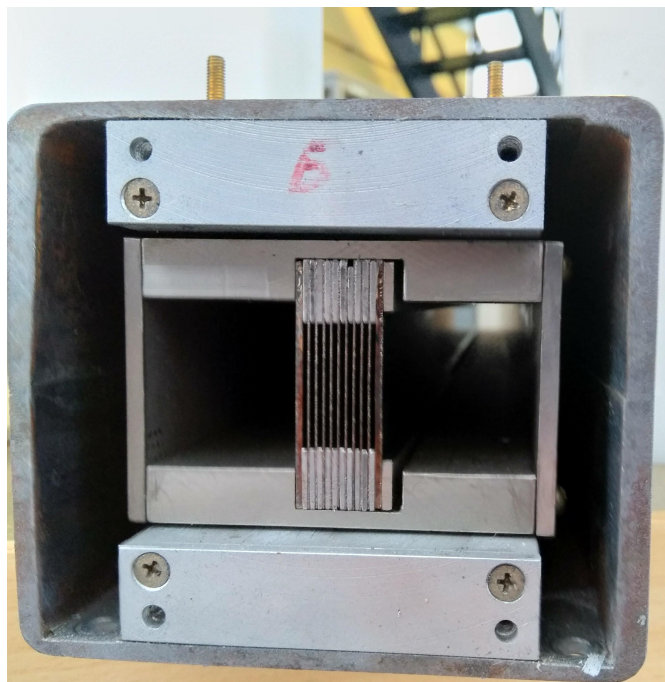
Fig. 5.1.: The interior of Atominstitut's Co/Ti supermirror II. The stack of coated glass plates is slightly bent to prevent direct transmission without mirror reflection. The Co-layers are magnetically saturated by permanent magnets. The beam cross section is 10×20 mm^2.

and 'Spin Exchange Optical Pumping' (SEOP) [89]. Filling such spin-polarized ^{3}He gas at a typical pressure of about 2 bar into a small quartz glass vessel allows to realize extremely effective broadband neutron polarizers and/or analyzers [90] with wide angular acceptance. Unlike to any other type of neutron polarizers the trajectories of the transmitted neutrons are not at all influenced by the insertion of such ^{3}He spin-filters. Therefore it is e.g. sufficient to place a cylindrically bent quartz vessel immediately behind the sample to analyze the polarization of neutrons that have been scattered over a large range of angles. To achieve the same angular coverage with supermirrors quite a large number of such expensive analyzers would be required have to be mounted immediately in front of the detectors in order to avoid the loss of information about the neutron scattering angles.

Meanwhile state-of-the-art ^{3}He spin-filters achieve decay times of the nuclear polarization of about 100 hours, which allows to perform even long-term neutron scattering experiments without filter replacement. However, an essential drawback is the (currently ?) poor availability of ^{3}He and its meanwhile extremely high price. Not to forget the effort of installing and maintaining the optical pumping infrastructure that is locally required at any neutron research center that wants to utilize this technology. For a small institution like the Atominstitut such ^{3}He spin-filters are therefore no realistic option.

5.2. Pulsed spatial magnetic spin resonance

As already mentioned, the main concept of spatial magnetic spin resonance has been proposed by Drabkin et al. already 1962 [15] and experimentally realized in 1968 [16]. There neutrons, polarized antiparallel to a vertical homogeneous static magnetic field, propagate horizontally through a transversal spatially alternating magnetic field with time-independent amplitude. Since in its rest frame each neutron - depending on its respective velocity - 'sees' its own frequency, the interaction of neutrons with such a NMR-like arrangement of crossed static and time-dependent magnetic fields leads to a resonant spinflip process just for a certain wavelength, which depends only on the resonator geometry and the strength of the vertical magnetic field. Thus only neutrons of this specific wavelength can pass an analyzer that is mounted behind the resonator, since due to their spinflip only their polarization is properly aligned along the analyzer orientation. Tuning the vertical 'selector' field allows the selection of neutrons with a certain wavelength. The most simple design of such a *'Drabkin-resonator'* consists of a meander-shaped aluminum foil that is placed between two polarizing supermirros and is supplied by a DC-current, see Fig. 5.2.

In order to chop this continuous monoenergetic beam into neutron packets which are required for time-of-flight measurements it is sufficient simply to turn the transversally alternating magnetic field of the resonator on and off periodically in time. The minimal duration of the neutron pulses that can be achieved in principle with such a *'conventional'* pulsed mode of operation of the resonator for strictly monochromatic neutrons of velocity v is determined by their time-of flight $\Delta t_{\min} = L/v$ through the whole resonator of length L. However, to achieve the smallest possible pulse width it is necessary that synchronously with the neutron passage time only one of the successive resonator half-periods should be activated, thereby 'accompanying' the particles during their propagation through the resonator. To realize this *'traveling-wave'*(TW) mode of operation a new type of resonator has been developed, named *'Badurek-resonator'* after its inventor [13]. There the original meander-foil is replaced by a sequence of single-turn aluminum coils, each forming one half-period of the resonator of length a (Fig. 5.2). Evidently, for the travelling-wave mode of operation each of these coils has to be supplied with its individual pulsed DC-current.

In contrast to the conventional pulsed Drabkin-type resonator the principally minimal pulse width that can be achieved for a monochromatic beam with the traveling-wave mode of operation corresponds to the neutron transit time $\Delta t_{\mathrm{TW,min}} = a/v$ through just one half-period. A further advantage of the modular resonator assembly compared to the standard-meander setup is its flexibility with respect to an amplitude modulation of the transversal field which allows to eliminate unwanted side-maxima in the spin-flip probability [18].

The spin flip probability $W(\lambda)$ for a neutron traversing a resonator with identical magnetic field amplitude B_1 in each of its elements is [29]

$$W(\lambda) = \frac{\xi^2}{(\Delta\lambda/\lambda)^2 + \xi^2} \times \sin^2\left[\frac{\pi L\lambda}{2a\lambda_0}\sqrt{(\Delta\lambda/\lambda)^2 + \xi^2}\right] , \qquad (5.2)$$
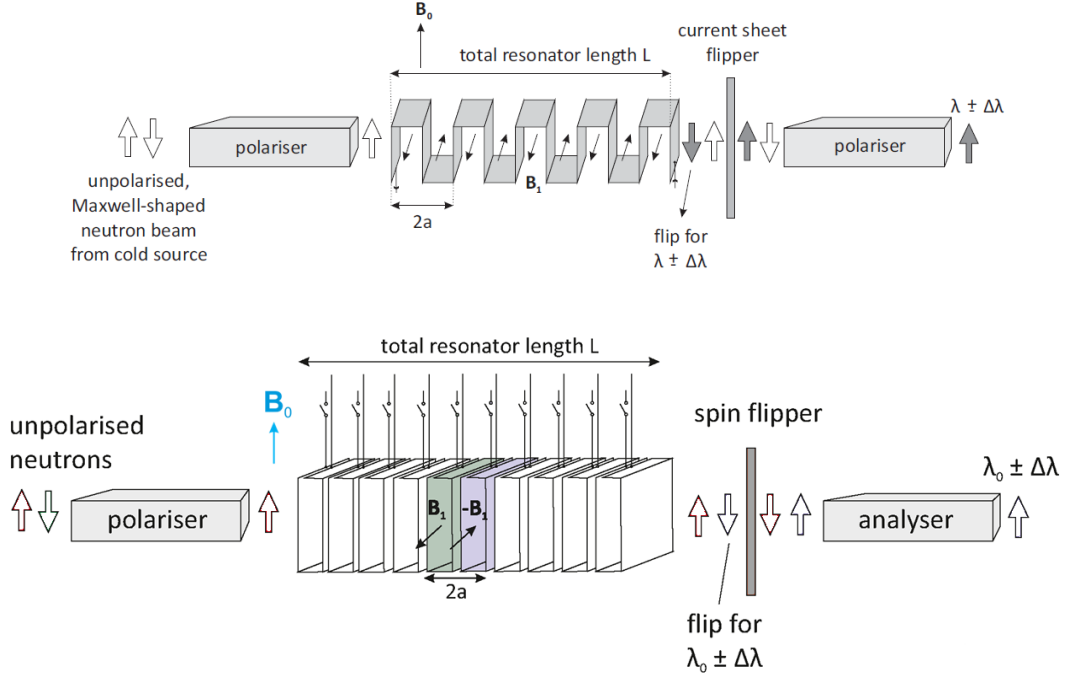
Fig. 5.2.: The basic experimental setup for spatial magnetic neutron spin resonance consists of the resonator placed between two supermirror polarizers, a broadband spin flipper (e.g. current-sheet) to establish 'dark-field' conditions. In the 'Drabkin-type' resonator the required spatially alternating magnetic field is produced by a DC-current supplied meander-shaped aluminum foil (upper picture). Contrary, the 'Badurek-type' resonator generates the transverse field components by means of a stack of individually controlled single-turn coils, thereby allowing a traveling-wave mode of resonator operation (see text).

with

$$\Delta\lambda = \lambda - \lambda_0 \tag{5.3}$$

and the resonance wavelength

$$\lambda_0 = \frac{\pi h}{am|\gamma|}\frac{1}{B_0} \ . \tag{5.4}$$

ξ is proportional to the ratio of the spatial alternating magnetic resonance field amplitude and the strength of the vertical selector field B_0

$$\xi = \frac{2}{\pi}\frac{B_1}{B_0} \ . \tag{5.5}$$

A spin flip occurs if both the resonance condition

$$\Delta\lambda = 0 \tag{5.6}$$

and the amplitude condition

λ_0	B_0	B_1	I_1	$\Delta t_{\text{TW,min}}$
40 Å	1.36 G	0.043 G	0.45 A	126 µs
5 Å	13.56 G	0.426 G	4.51 A	13 µs
1.8 Å	37.68 G	1.183 G	12.53 A	4.55 µs
1 Å	67.82 G	2.13 G	22.55 A	2.53 µs

Tab. 5.1.: Characteristic values of the selector field strength B_0, transverse field amplitude B_1, and of the current generating B_1 in the resonator coils for a set of neutron wavelength. $\Delta t_{\text{TW,min}}$ denotes the theoretically minimal I_1-current pulse duration for traveling-wave (TW) mode of operation of the of the actual MONOPOL setup with a total length $L = 50$ cm and a half-period $a = 1$ cm.

$$\frac{L}{a}\xi = 2k + 1 \qquad k \in \mathbb{N}_0 \tag{5.7}$$

are fulfilled. This set of equations allows to calculate the magnetic field strengths that are required for a spin flip. The necessary current to generate the resonance field B_1 in the resonator coils can be determined via the empirical relation

$$B_1 = I_1 \times 0.0945 \, \text{G/A} \, ,$$

which is taken from [91]. Additionally, the lower theoretical limit of the I_1-current pulse duration $\Delta t_{\text{TW,min}}$ is listed, which for the traveling-wave mode of operation is just the neutron transit time through one half-period of the resonator for given wavelength. Characteristic values of these parameters are given in Tab. 5.1 for very cold , cold, and thermal neutrons. It can be seen that in particular for thermal neutron neutrons the specification of the required pulsed power supply system to run MONOPOL are extremely demanding.

5.3. MONOPOL experiments with very cold neutrons

Several different prototypes of the neutron spin resonator MONOPOL have been developed. The last version was designed in 2013 [91, 92] and was tested in 2014 at the instrument PF2 of the Institut-Laue-Langevin (ILL) in Grenoble with a beam of white *very cold neutrons* [2, 93]. Since very cold neutrons have velocities in the range of $100 \, \text{m s}^{-1}$ the required currents are about one order of magnitude lower and the current pulse times are about one order of magnitude longer than with thermal neutrons ($v \sim 2200 \, \text{m s}^{-1}$). The probably most exiting experiment was to see for the first time the action of this MONOPOL prototype upon the spectrum of a polychromatic beam for different active lengths of the resonator and for two different orders of the wavelength resonance [19]. The time-of-flight distributions with and without running the resonator continuously were obtained by means of a mechanical disc chopper which was mounted at the PF2-beamport. Then the start signal of the mechanical chopper was synchronized with the resonator running in
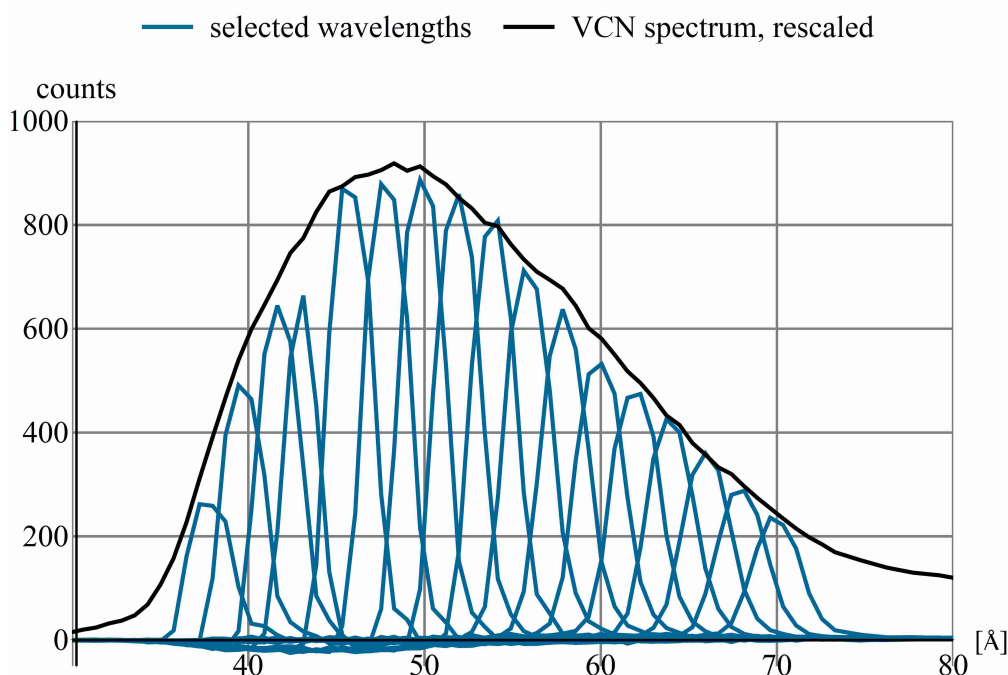
Fig. 5.3.: Spectrum analysis of the VCN-beam at PF2 at the ILL done with MONO-
POL in traveling-wave-mode (TWM) with 2 ms pulses and a mechanical
disk chopper at the PF2-VCN beamport. The resonator's transmission
wavelength was tuned in 2 Å-steps between 37 Å and 69 Å. A re-scaled
wavelength spectrum of the VCN-beam obtained with the resonator
turned off envelopes all the pulsed spectra, indeed.

traveling-wave mode with 2 ms pulse width. By tuning the resonator's transmission
successively to 17 different resonance wavelengths in the range between 37 Å and
69 Å the wavelength distributions plotted in Fig. 5.3 were obtained. It can be
seen that the properly re-scaled VCN spectrum that is obtained if the resonator is
turned off exactly envelops all the pulsed spectra, indeed.

5.4. MONOPOL-power supply for thermal neutrons

After the successful first test experiments at a VCN-beam an improved current-
source concept that should allow to run MONOPOL also with thermal neutrons
was elaborated by Andrew Pelczar, the head of the electronic laboratory of the
Atominsitut. Since thermal neutrons are about one order of magnitude faster than
VCN, currents to generate magnetic fields need to be one order of magnitude higher
and current switching times need to be one order of magnitude faster. For neutrons
with 1 Å, currents of 20 A have to be switched in about 3 μs, which is all but no
trivial task. Since no commercial power supply could be found that meets the
required specifications an appropriate, quite complex power supply was designed
for this project [94].

The basic concept of this current-source is just as simple as splendid and is shown
in Fig. 5.4: a power source for smaller but precise currents (PS1) and a power

source for larger and less precise currents (PS2) are feeding the electric circuit. The current can be switched between the real load (the resonator coil) and an artificial load (a resistor) for switching the magnetic field in the coil on and off by n-channel metal-oxide-semiconductor field-effect transistors (MOSFETS). Thereby both otherwise unavoidable long settling times of several hundreds of microseconds and current switching spikes are avoided since the magnitude of the current stays constant. Thus short switching times in the low μs-regime are achievable. This new power supply system required for MONOPOL's operation with thermal neutrons has reached an enormous complexity, since each of the individual coils of the resonator has to be controlled by a separate current-source, which means that 48 circuit boards are required, see Fig. 5.5.
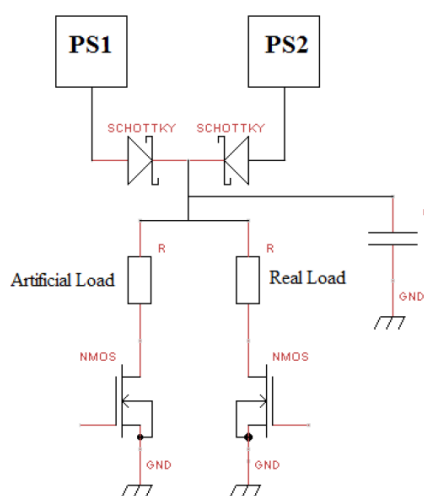

Fig. 5.4.: Schematic electronic circuit of the new MONOPOL current-sources. More details can be found in the text.

5.5. MONOPOL at the *Thermal White Neutron Beam* facility

The entirely new resonator power supply system that has been developed for running MONOPOL at a thermal neutron beam is going to be ready for first neutron experiments at the end of 2018. Consequently, the resonator will soon be tested at the *Thermal White Neutron Beam* facility. The first preparatory neutron polarizer experiments (see Section 5.6) are of advantage for the correct and accurate installation of the resonator setup. After the experiments at the white VCN beam in 2014 (see Section 5.3), this will be the first time that MONOPOL's performance will be checked at a thermal white neutron beam. Experiments with thermal neutrons without doubt are the 'top class' of experiments for MONOPOL because the strengths of the currents to be switched are much larger and their switching times much shorter compared to the case of cold or VCN neutrons.

Nevertheless, the most challenging scientific case of MONOPOL will be its planned installation at the PERC experiment at the FRM II research reactor in Munich
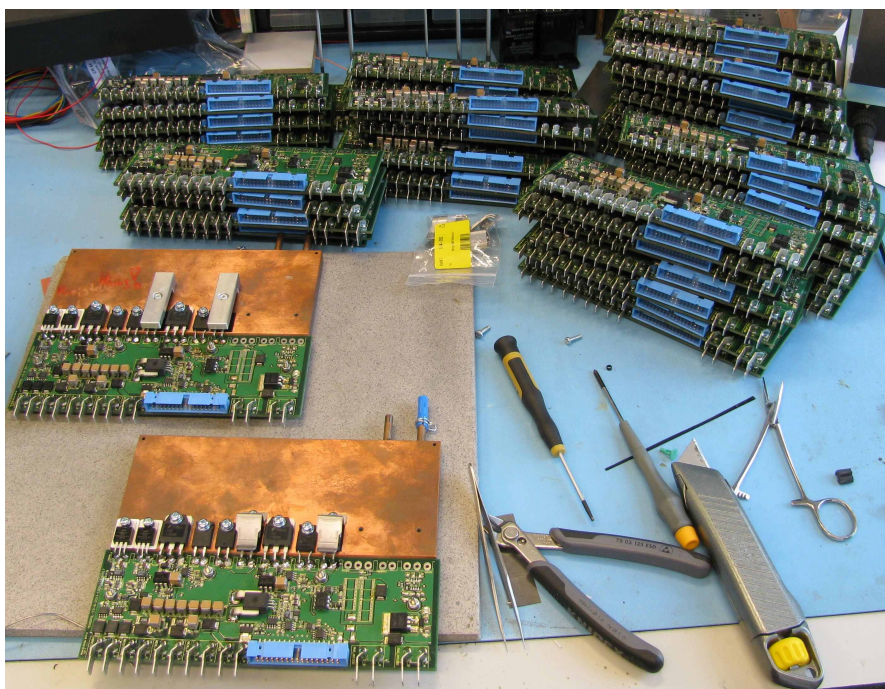
Fig. 5.5.: Circuit boards of the newly designed power supply for the neutron resonator MONOPOL. Every single circuit board controls the current within one of the 48 individual coils of the resonator.

[3]. For this high-precison β-decay experiment with cold neutrons MONOPOL is going to be an important tool for neutron beam tailoring and PERC will benefit immensely from its high flexibility. Surely MONOPOL's biggest advantage for PERC will be the easily possible change of the neutron velocity, the length of a neutron package, or the package repetition rate. The variation and adjustment of all these parameters can be achieved almost instantaneously. Thus the flexibility provided by MONOPOL is much higher than that achievable with ordinary velocity selectors or disc choppers. Due to this flexibility e.g. the optimal length of a dispersing neutron package can be found out and adjusted easily, as well as the optimal time interval between two subsequent packages with respect to minimization of background signals by proper synchronization with PERC's integrated mechanical background chopper. Undoubtedly this will lead to a faster and better characterization of the entirely new PERC setup and consequently to more precise scientific results.

5.6. Polarizer characterization at the *Thermal White Neutron Beam*

MONOPOL is going to be tested at the *Thermal White Neutron Beam* facility end of 2018. As a first preparatory step of setting up the resonator at this intense polychromatic beam a supermirror polarizer was installed and characterized, see Fig. 5.6.
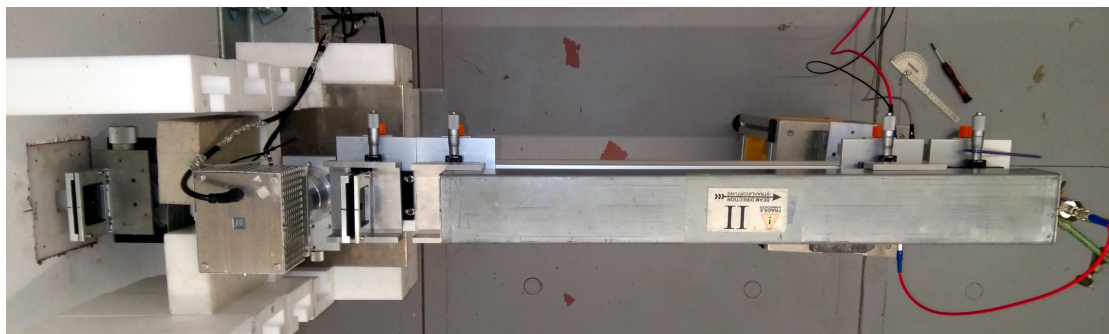
Fig. 5.6.: Starting on the left hand side: the thermal white neutron beam passes a $3 \times 10\,\text{mm}^2$ Cd-slit aperture, then a Fermi chopper, and another $3 \times 10\,\text{mm}^2$ Cd-slit aperture for sharp collimation (distance between the apertures: 30 cm). Thereafter, the beam gets polarized by a Ti-Co supermirror. The transmitted polarized neutrons are detected by a ^{3}He-detector seen on the right-hand side of the picture. The angle of the supermirror relative to direction of the incident neutron beam can be tuned my means of a lateral linear translation stage mounted close to the downstream end of the polarizer, keeping its entrance window matched with the chopper window.

A curved polarizing Co-Ti supermirror (unfortunately neither the exact radius of curvature nor the m-value and thus the critical angle θ_c of the mirror are known) is placed in a sharply collimated neutron beam, the angle θ of the mirror relative to the beam trajectory can be tuned by means of a linear translation stage. Several time-of-flight measurements were performed to investigate the modification of the neutron spectrum that is caused by the wavelength- and angle-dependent mirror reflectivity. Since this is the first time that at the Atominstitut a supermirror is utilized at a polychromatic neutron beam, this spectrum modification is of particular interest. As seen from Fig. 5.7 also the integral transmission of the supermirror changes with varying θ, exhibiting a maximum at an angle of about $0.25°$. Unfortunately a measurement of the polarization degree P of the transmitted beam could not be part of this experiment, since no second supermirror was freely available on short call to act as analyzer. However, from previous measurements with a pair of supermirrors with monochromatic neutrons it is known that P is not maximal if the integral transmission is at its maximum but rather for a somewhat larger glancing angle of about $0.5°$.

In Fig. 5.8 the transmission of the polarizer is shown both as a function of its angle relative to the neutron beam and of the neutron wavelength. Additionally, a measurement without polarizer was performed so that the intensity ratio p of neutrons transmitted by the polarizer and those registered in the absence of the supermirror can be calculated, see Fig. 5.9. The increasing efficiency of the polarizer for colder neutrons is clearly visible.

However, the glancing angle-dependence of the neutron spectrum can be seen best if all time-of-flight spectra of Fig. 5.8 are normalized according to Eq. (2.6) to make them directly comparable: for higher glancing angles the spectrum is shifted clearly towards longer wavelengths, see Fig. 5.10. While the maximum of
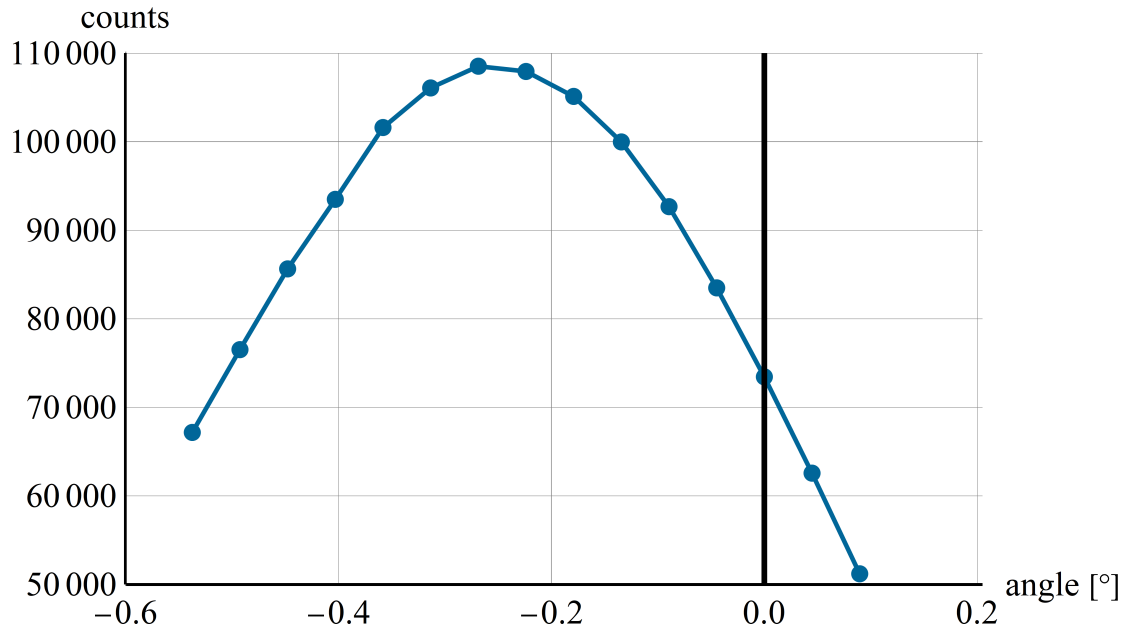
Fig. 5.7.: The integral transmission of the curved Co-Ti supermirror as a function of its angle θ relative to the neutron beam.
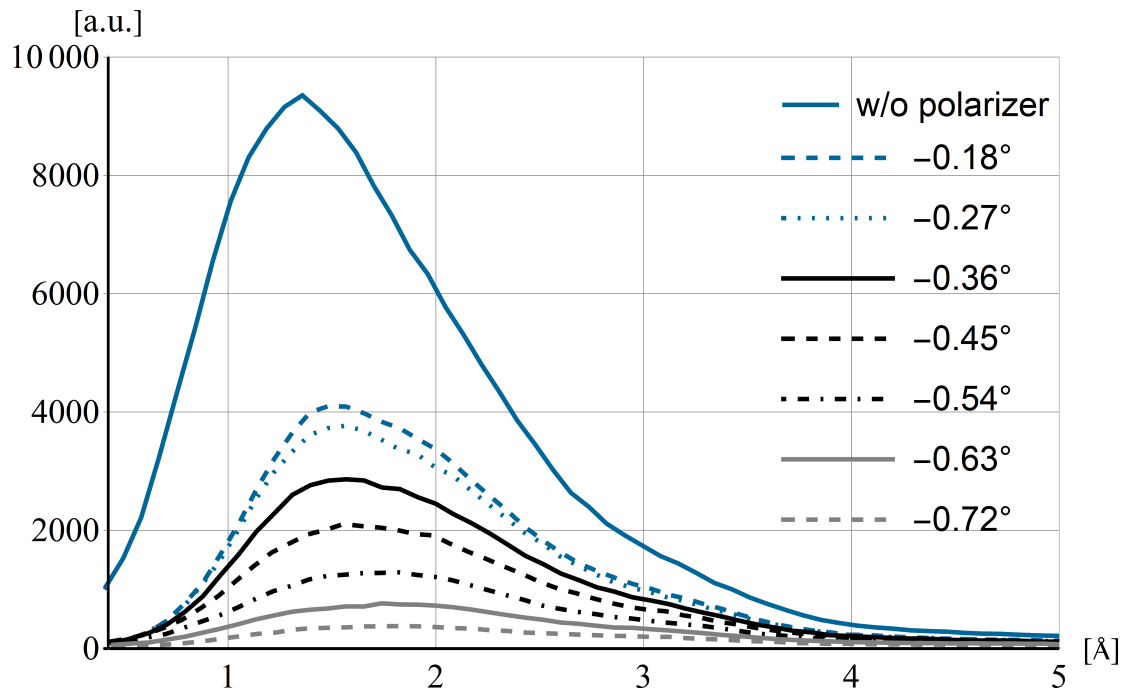

Fig. 5.8.: Neutron spectra as a function of the polarizer alignment angle θ obtained by means of time-of-flight measurements. The also plotted spectrum taken without supermirror in the beamline has its maximum at 1.35 Å. The data are corrected for wavelength-dependent detector efficiency.
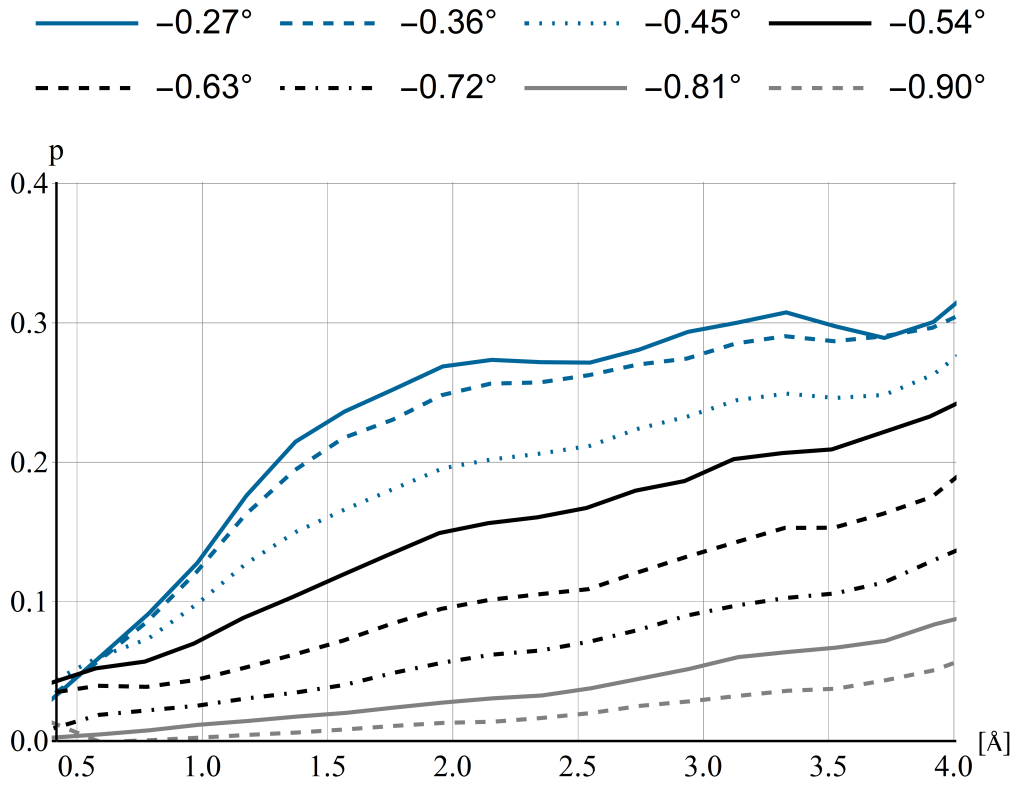
Fig. 5.9.: The intensity ratio p between neutrons transmitted by the polarizer and those registered in the absence of the supermirror (see Fig. 5.8) reveals the angle-dependence of the relative transmission as a function of the neutron wavelength. The data are corrected for wavelength-dependent detector efficiency.
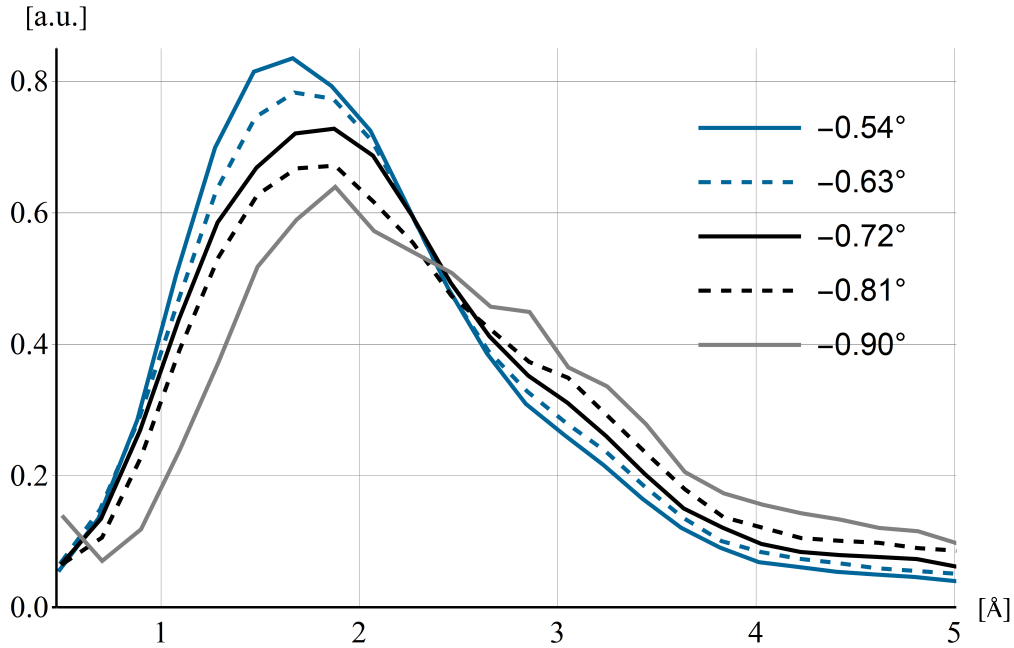

Fig. 5.10.: Normalizing the time-of-flight measurements reveals that the transmitted neutron spectrum gets colder with increasing glancing angle. The data are corrected for wavelength-dependent detector efficiency.

the spectrum of the thermal white neutron beam is at $1.35\,\text{Å}$ the maximum with polarizer is between $1.6\,\text{Å}$ and $1.9\,\text{Å}$, depending on the respective glancing angle.

These measurements have shown the feasibility of polarizing neutrons at the thermal white neutron beam. The installation and proper adjustment of the polarizing supermirror has turned out to be very simple and plenty of space is still available for experimental setups. Quite some useful information about the proper installation of a such a polarizer at the thermal white beam could be gained. Characteristics like glancing angle-dependence, total transmission and spectral shift of the supermirror have been measured and are essential for future experiments with polarized neutrons. This experiment also has figured out that there will be sufficient space for the neutron spin resonator MONOPOL with its quite long experimental setup consisting of two polarizers, two spin flippers, 48 resonator coils, and a ^{3}He-detector (at least $3\,\text{m}$ in total). Thus, it has set the basis for the installation of the next generation of MONOPOL which will start end of 2018 [95].

6. Conclusion & Outlook

THE clear objective of this thesis was the design and installation of a multi-purpose and high-flux *Thermal White Neutron Beam* facility at the TRIGA reactor in Vienna.

The TRIGA reactor offers already an excellent infrastructure for a number of very different neutron physics experiments (as it is described in Chapter 1), such as there are for example: neutron radiography and tomography, neutron polarimetry, neutron interferometry, ultra-small-angle scattering, or neutron activation analysis. However, one important facility was missing over the last decades: a neutron beam which is not monochromatic but polychromatic (thus, with a so-called 'white' spectrum) and therefore offers the highest possible flux.

In this thesis, a concept for such a beam facility was worked out and realized. Its main characteristics are

- a highest possible neutron flux of up to $\sim 10^7\,\mathrm{cm}^{-2}\,\mathrm{s}^{-1}$
- high flexibility
- easy accessibility even during reactor operation
- large experimental space
- low fast neutron and γ-background
- safe and simple usability

Since a high flux implies high dose rates, a biological shielding was necessary to be in compliance with radiation protection rules. A special radiation protection concrete was designed and tested which allowed a massive reduction of the thickness of the heavy concrete walls and also to reduce radiation background of the experiments. Moreover, this shielding chamber of the new *Thermal White Neutron Beam* facilty is flexible and can be assembled, disassembled, and/or modified easily by the reactor crew.

To reduce γ- and fast neutron background a filter set composed of a $15\,\mathrm{cm}$ thick sapphire single-crystal and a $10\,\mathrm{cm}$ thick bismuth single-crystal has been installed inside of beamtube B of the TRIGA reactor. The modification of the neutron spectrum caused by this filter set as well as the change of the integral neutron flux was described theoretically, then calculated, and finally measured experimentally.

By simulating the shielding utilizing the classified software package MCNP and testing the new concrete experimentally it could be verified that this facility will comply with all radiation protection requirements.

After its installation the biological shielding was characterized in collaboration with an external expert to get a legal permission from the responsible ministry to use it routinely. The given dose rate limit of $5\,\mathrm{\mu Sv\,h}^{-1}$ on the outer surface of the radiation shielding chamber of the *Thermal White Neutron Beam* facility was held clearly. Additionally, the measured dose rate at the outer surface of the radiation chamber was compared with the result of simulations and no statistical significant deviations were found.

6. Conclusion & Outlook

The at that time unknown neutron beam characteristics such as

- neutron flux at different positions
- beam cross section at various positions
- beam divergence
- beam homogeneity
- Cd-ratio of the neutron spectrum
- in-beam neutron and γ-dose rate
- the thermal neutron flux spectrum

were measured to characterize the new facility (as it is shown in Chapter 4 in great detail). These measurements are an important basis for planning future experiments to be performed at this new facility.

The most important characteristic of the new facility is the integral total neutron flux at the beamport, which was measured to be

$$\Phi_{total} = (2.90 \pm 0.10) \times 10^6 \mathrm{cm}^{-2}\,\mathrm{s}^{-1}$$

and the integral thermal neutron flux at the beamport:

$$\Phi_{total} = (2.88 \pm 0.10) \times 10^6 \mathrm{cm}^{-2}\,\mathrm{s}^{-1}$$

Which leads to a Cd-ratio of 124. Uninstalling the bismuth filter would increase the neutron flux by a factor of about 3.3 (which follows from Tab. 3.1) leading to a total neutron flux of $\sim 10^7\,\mathrm{cm}^{-2}\,\mathrm{s}^{-1}$.

First experiments done with the *Thermal White Neutron Beam* have shown its scientific value but also its broad applicability. For instance, for the International Atomic Energy Agency (IAEA) flash memory cards and other quite bulky electronic devices, such as electronic seals and cameras often to be used in radiation environments, were tested with respect to their radiation hardness while they were switched on and in operation. Additionally, the new facility was used also as a station for radiography (as it is shown in Fig. A.1) to distinguish between different types of memory cards. Meanwhile these experiments already have been completed successfully.

Furthermore, the quality of a single-crystal bismuth was checked by installing a 'quick and dirty' Laue-Bragg camera to demonstrate the broad applicability of the *Thermal White Neutron Beam* (details were given in Section 4.6).

The last two experiments mentioned have illustrated that the new *Thermal White Neutron Beam* facility could be used also as a splendid station for neutron imaging and radiography. Because of a neutron flux which is about 10 times higher, a comparable effective collimation ratio (so-called 'L/D-ratio'), a larger beam diameter (depending on the chosen distance to the beam port), and - due to the installation of neutron filters - a much better Cd-ratio than that available at the present radiography stations of the TRIGA reactor (as it can be seen in Tab. 6.1).

	Thermal White Neutron Beam	Station 1	Station 2
Flux $cm^{-2}\,s^{-1}$	2.9×10^6	3×10^5	1.3×10^5
L/D-ratio	44	50	125
Beam-diameter	36-625	40	9
Cd-ratio	124	3	20

Tab. 6.1.: Comparison of the *Thermal White Neutron Beam* used as a radiography station with the already existing radiography stations at the TRIGA reactor in Vienna [96].

The installation of a polarizing supermirror (details were described in Section 5.6) has shown the feasibility of utilizing polarizing neutrons at the new facility but it constitutes also the basis of the first *'big'* experiment which will start in the end of 2018 at the *Thermal White Neutron Beam*: a thorough test of the neutron resonator MONOPOL (explained in Chapter 5) for the first time with thermal neutrons. A completely new power supply had to be developed for this ambitious purpose, which currently is going to be completed.

MONOPOL will no longer remain in the prototype stadium: after successful characterization it will be used for beam preparation at the PERC-instrument for high-precision neutron β-decay. Contrary to the experiments with very cold neutrons at the ILL in 2014, thermal neutrons are about 10 times faster. Therefore, currents have to be 10 times higher and current switching times by a factor of 10 shorter. Without doubt this will be a challenging benchmark for MONOPOL. The successful experiments with VCN (explained in Section 5.3) in combination with those experiments that will be performed with thermal neutrons will cover large parts of the neutron spectrum and definitely will show the high flexibility of this new device.

The first goal will be the analysis of the thermal neutron spectrum, similar that done with VCN in 2014 (as it is shown in Fig. 5.3).

Besides of that, the *Thermal White Neutron Beam* is also going to push detector research at the Atominstitut. Currently three different types of neutron detectors, namely

- a CVD diamond based detector in combination with pulse shape analysis [77]
- a UCN track detector with µm-resolution [97] and
- an online UCN detector with low background rate [98]

are under development at the Atominstitut. In the past the only possibility to test these detectors was on a monochromatic beam line with low flux ($\sim 10^3\,cm^{-2}\,s^{-1}$). Due to the fact that all these detectors have quite a low detection efficiency for thermal neutrons the possibility of testing them with a more than 1000 times higher neutron flux will push the development of these detectors tremendously.

Probably the most prominent point for improving the new facility concerns the neutron detection equipment that is available for high neutron fluxes and large beam diameters. The currently used 1-inch-^{3}He-detector which was purchased for low-flux neutron beam experiments exhibits significant saturation effects if more

than some mm^2 of its surface are exposed to the *Thermal White Neutron Beam* . Therefore either adequate high-flux detectors, or alternatively detectors with a lower efficiency might be required for future experiments. As it was mentioned above, it should also be feasible to install a competitive (temporary) imaging station at the *Thermal White Neutron Beam* facility. For this, an imaging system such as a cooled CCD-camera in combination with a neutron scintillator plate for large beam diameter would be of particular interest.

A. Appendix

A.1. Thermal White Beam neutron spectra

[99]Here, the *Thermal White Neutron Beam* spectra are listed, ready to use for MCNP6. Since the filter set shifts the spectrum a bit, the spectra for the possible filter sets used are listed. The given "Filterfactor" is the relative reduction of the total flux compared to the reactor neutron spectrum in beamtube B.

```
c  15cmSa-0cmBi
c  Filterfactor: 0.3605
SI3 H 1E-10 5E-10 1E-9 5E-9 1E-8 5E-8 1E-7 5E-7 1E-6   &
      5E-6 0.00001 0.00005 0.0001 0.0005 0.001 0.005   &
      0.01 0.05 0.1 0.5 1 5 10 18
SP3 D 0 0.0000433323 0.000216381 0.00996901            &
     0.0307568 0.420729 0.262906 0.223692 0.0207468    &
     0.0106366 0.000808664 0.000953149 0.000273199     &
     0.000490432 0.000166919 0.000313056 0.000109739   &
     0.000206323 0.0000315427 0.0000993375 0.000487251 &
     0.0109645 0.00478628 0.000612902
```

```
c  15cmSa-5cmBi
c  Filterfactor: 0.1899
SI3 H 1E-10 5E-10 1E-9 5E-9 1E-8 5E-8 1E-7 5E-7 1E-6   &
      5E-6 0.00001 0.00005 0.0001 0.0005 0.001 0.005   &
      0.01 0.05 0.1 0.5 1 5 10 18
SP3 D 0 0.0000786634 0.000394735 0.0174901 0.0501722   &
     0.515208 0.232997 0.151214 0.0116661 0.00578166   &
     0.000430971 0.00050612 0.000144852 0.000259943    &
     0.0000884607 0.000165904 0.0000581559 0.000107556 &
     0.0000154035 0.00008066 0.000415917 0.00801568    &
     0.00395368 0.000754138
```

```
c  15cmSa−10cmBi
c  Filterfactor:  0.1084
SI3 H   1E−10 5E−10 1E−9 5E−9 1E−8 5E−8 1E−7 5E−7 1E−6   &
        5E−6 0.00001 0.00005 0.0001 0.0005 0.001 0.005   &
        0.01 0.05 0.1 0.5 1 5 10 18
SP3 D   0 0.000131462 0.000662898 0.0282567 0.0753864    &
        0.590109 0.191085 0.0947862 0.00603962 0.00289327 &
        0.000211438 0.000247402 0.0000707005 0.000126833  &
        0.000043157 0.0000809369 0.0000283714 0.0000517033 &
        6.97524E−6 0.0000625064 0.000327835 0.00548217     &
        0.00305497 0.000854795
```

```
c  15cmSa−15cmBi
c  Filterfactor:  0.0666
SI3 H   1E−10 5E−10 1E−9 5E−9 1E−8 5E−8 1E−7 5E−7 1E−6 &
        5E−6 0.00001 0.00005 0.0001 0.0005 0.001 0.005 &
        0.01 0.05 0.1 0.5 1 5 10 18
SP3 D   0 0.000204001 0.00103366 0.0424009 0.105237    &
        0.637706 0.146259 0.0555603 0.00290362 0.00134447 &
        0.0000963186 0.00011229 0.0000320415 0.0000574615 &
        0.0000195498 0.0000366628 0.0000128516            &
        0.0000231129 2.95522E−6 0.0000464389              &
        0.000240616 0.00354156 0.00222978 0.000900229
```

A.2. Shielding concrete recipe

Here, the recipe for the shielding concrete is listed. Design and civil engineering tests were done by smartminerals GmbH. Since B_4C is a very expensive additive, it the amount can varied and fit to the shielding problem, see [63].

	Rezeptur MV2
Größtkorn der Gesteinskörnung	25 mm
Zement (CEM II/B 32,5N)	$280 \, \text{kg m}^{-3}$
Anrechenbarer BM-Gehalt	$280 \, \text{kg m}^{-3}$
Zusatzmittel Dynamon LZF	$2.13 \, \text{kg m}^{-3}$
Gesamtwassergehalt	$180 \, \text{kg m}^{-3}$
Hämatit 0/6	$1283 \, \text{kg m}^{-3}$
Hämatit 6/25	$881 \, \text{kg m}^{-3}$
Serpentin 0/4	$96 \, \text{kg m}^{-3}$
Serpentin 4/8	$594 \, \text{kg m}^{-3}$
Borkarbid (B_4C)<1 mm	$68 \, \text{kg m}^{-3}$
Betoneinbautemperatur	$20 \, °\text{C}$
Frischbetonrohdichte	$3392 \, \text{kg m}^{-3}$
Ausbreitmaß nach 10 min	40 cm
Luftgehalt im Frischbeton	1,5% (nach 10 min)
Druckfestigkeit 56 Tage	$55 \, \text{N mm}^{-2}$
Betonsortenbezeichnung	C25/30 (56) XC1 GK25 F38

Tab. A.1.: The recipe of the shielding concrete. The B_4C content is variable. For the slabs a content of $68 \, \text{kg m}^{-3}$ was used, while for the chamber the content was $34 \, \text{kg m}^{-3}$.

A.3. MCNP concrete recipes

Here, the MCNP recipe of the shielding concrete and of ordinary concrete which was evaluated experimentally is listed. For more details, see chapter 3.2.1.

A.3.1. Ordinary concrete

```
c  Material specifications concrete
c ——Normalbeton (density = −2.395 g/cc)
m4 &
1001.62c            −0.022095            &
1002.24c            −0.000005            &
6000.24c            −0.002484            &
8016.62c            −0.574699            &
8017.66c            −0.000232            &
11023.62c           −0.015208            &
12000.62c           −0.001266            &
13027.62c           −0.019953            &
14028.24c           −0.279872            &
14029.24c           −0.014719            &
14030.24c           −0.010036            &
19000.62c           −0.010045            &
20000.62c           −0.042951            &
26054.62c           −0.000363            &
26056.62c           −0.005914            &
26057.62c           −0.000139            &
26058.62c           −0.000019
```
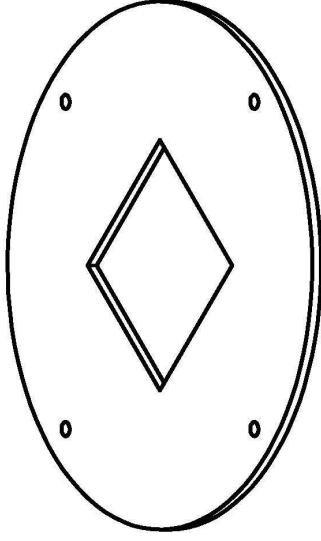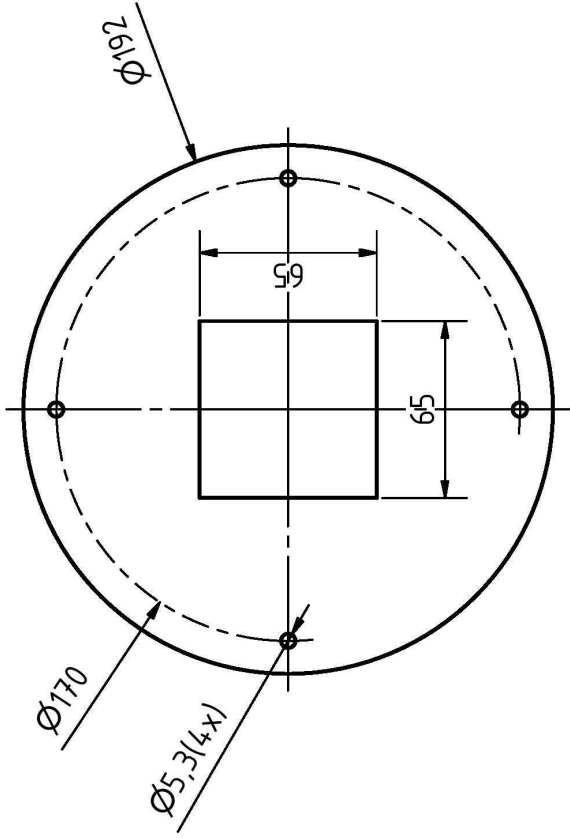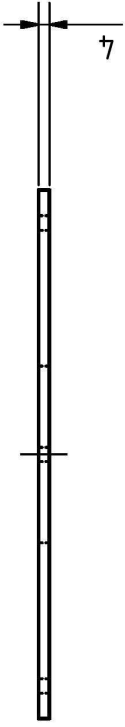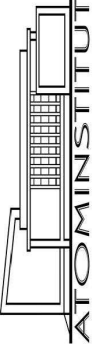
A.3.2. Shielding concrete

```
c  Material  specifications  concrete
c  Concrete  Smart  Minerals   (density  =  −3.383  g/cc)
c  2w%B4C
m4 &
1001.62c     −0.011223663       &
1002.24c     −0.000000253986    &
5010.66c     −0.003134146       &
5011.66c     −0.01261533        &
6000.24c     −0.004580657       &
8016.62c     −0.384999793       &
8017.66c     −0.00015542        &
11023.62c    −0.002095599       &
12000.62c    −0.040945392       &
13027.62c    −0.005512826       &
14028.24c    −0.062418723       &
14029.24c    −0.003282719       &
14030.24c    −0.002238289       &
19000.62c    −0.001667769       &
20000.62c    −0.010947576       &
25055        −0.0000204202      &
26054.62c    −0.025619233       &
26056.62c    −0.417388832       &
26057.62c    −0.00981012        &
26058.62c    −0.001340952
```

A.4. Drawings

On the following page, the drawing of the boron-steel aperture installed inside of the beamtube can be found. 15 of such aperture-plates are installed mounted at the front of the beamtube insert for beam definition. The front-side of the aperture is covered with a 2 mm cadmium sheet to prevent excessive neutron activation. On the backside of the beamtube insert, 14 of these apertures-plates are installed and also covered with a 2 mm cadmium sheet.

7

Ø192

65

65

Ø170

Ø5,3(4x)

A.5. Pictures

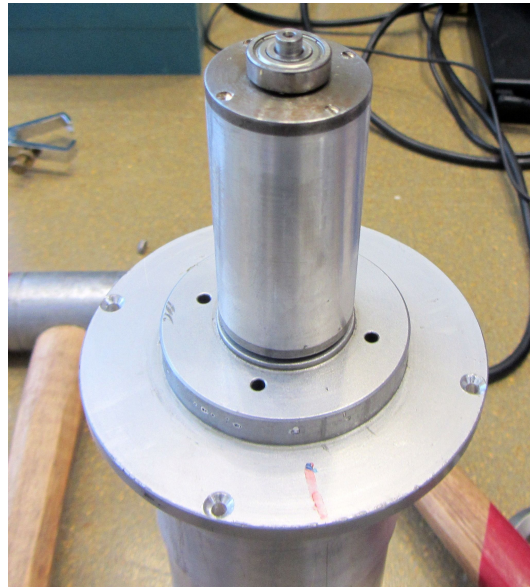**Fig. A.1.:** Radiographic image of SD-cards and micro SD cards from different suppliers. It was taken at the Thermal White Beam by means a 2D-image plate detector. Exposure time: 60 s. The image was taken for the IAEA to characterize SD cards.
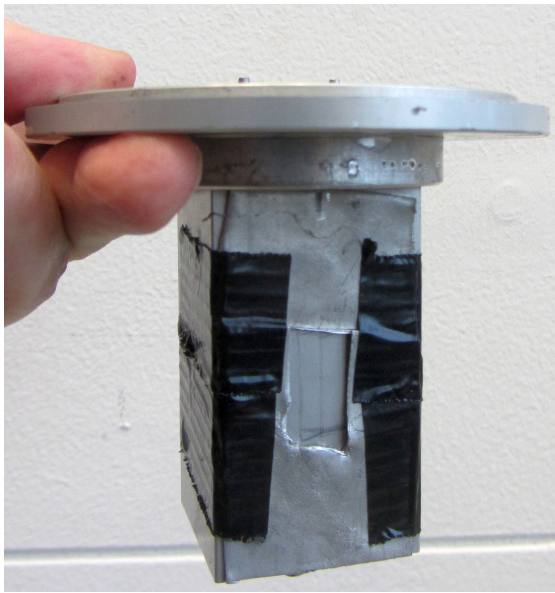
(a) inner box

(b) rotating cylinder

(c) engravings on rotating cylinder

Fig. A.2.: The inner structure of the ATI's Fermichopper. On picture (b) the rotating cylinder can be seen (upside down), which is capsuled inside of a box made of aluminium (b). On picture (c), the upper cap of the rotating cylinder is dismantled. Engravings of the aluminium and cadmium sheets were found. The thickness of the sheets is 1 mm. The diameter of the cylinder is 32 mm

(a) The interlock's control unit and lattice door for access control
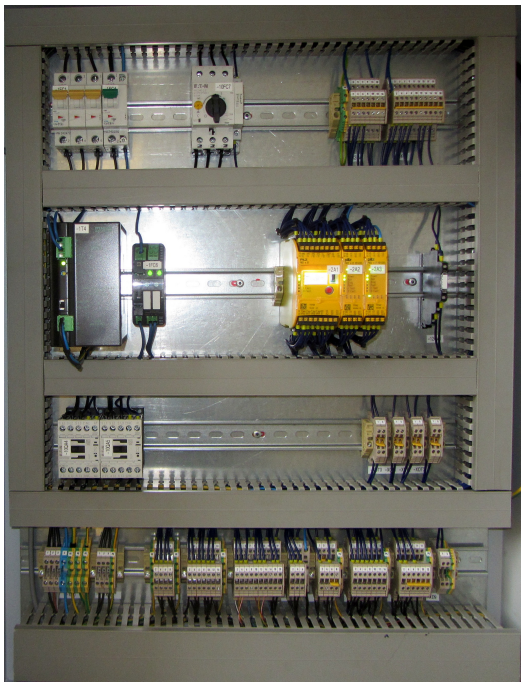
(b) The interlock's main control box

(c) end switches

Fig. A.3.: The interlock system is controlled by PNOZmulti 2 from Pilz GmbH (picture (b) in the center. The position of the lift table is controlled by 2 magnetic end switches. An additional mechanic end switch is installed for redundancy.

Bibliography

[1] *A General Monte Carlo N-Particle (MCNP) Transport Code*, `https://mcnp.lanl.gov/-` (2018), accessed: 04.04.2018

[2] E. Jericha, J. Bosina, P. Geltenbort, M. Hino, W. Mach, T. Oda, G. Badurek, *Neutron detection in the frame of spatial magnetic spin resonance*, Nucl. Instr. Meth. Phys. Res. A **845** (2017) 552–555

[3] D. Dubbers, H. Abele, S. Baeßler, B. Märkisch, M. Schumann, T. Soldner, O. Zimmer, *A clean, bright, and versatile source of neutron decay products*, Nucl. Instr. Meth. Phys. Res. A **596** (2008) 238–247

[4] J. Chadwick, *Possible existence of a neutron*, Nature **129** (1932) 312

[5] D. Dubbers, M. G. Schmidt, *The neutron and its role in cosmology and particle physics*, Rev. Mod. Phys. **83** (2011) 1111–1117

[6] G. Badurek, *Fast inversion of neutron spin*, Nucl. Instr. Meth. Phys. Res. A **189** (1981) 543–553

[7] G. Badurek, H. Rauch, A. Zeilinger, *Dynamic concepts in neutron polarization*, Zeitschrift f. Physik B-Condensed Matter **38** (1980) 303–311

[8] G. Badurek, S. Müller, *Analytical approach to dynamic neutron polarization*, Proc. ILL Millennium Symposium (2001) 326–328

[9] S. Müller, G. Badurek, *Loss-free polarization of pulsed neutron beams*, Appl. Phys. A **74** (2002) S231–S233

[10] G. Badurek, C. Hartl, E. Jericha, *Loss-free neutron polarization*, Physica B **397** (2007) 192–194

[11] G. Badurek, C. Hartl, E. Jericha, *A non-conventional neutron polariser concept*, Nucl. Instr. Meth. Phys. Res. A **586** (2008) 95–99

[12] B. Alefeld, G. Badurek, H. Rauch, *Observation of the neutron magnetic resonance energy shift*, Zeitschrift f. Physik B-Condensed Matter **41** (1981) 231–235

[13] G. Badurek, E. Jericha, *Upon the versatility of spatial neutron magnetic spin resonance*, Physica B **335** (2003) 215–218

[14] G. Badurek, C. Gösselberger, E. Jericha, *Design of a pulsed neutron magnetic spin resonator*, Physica B **406** (2011) 2458–2462

[15] G. M. Drabkin, *Analysis of energy spectrum of polarized neutrons with the aid of a magnetic field*, Sov. Phys. JETP **16** (1963) 781

[16] G. M. Drabkin, V. A. Trunov, V. B. Runov, *Static magnetic field analysis of a polarized neutron spectrum*, Sov. Phys. JETP **27** (1968) 194

[17] M. M. Agamalyan, G. M. Drabkin, S. V. I, *Spatial spin resonance of polarized neutrons. A tunable slow neutron filter*, Physics Reports **168** (1988) 265–303

[18] C. Gösselsberger, *Entwicklung eines Wanderwellen-Neutronenspinresonators*, Dissertation, TU Wien (2012)

[19] E. Jericha, C. Gösselsberger, H. Abele, S. Baumgartner, B. Berger, P. Geltenbort, M. Hino, T. Oda, R. Raab, G. Badurek, *A traveling-wave magnetic neutron spin resonator for tailoring polarized neutron beams*, in preparation (2018)

[20] C. Gösselsberger, H. Abele, G. Badurek, E. Jericha, S. Nowak, G. Wautischer, A. Welzl, *Design of a novel pulsed spin resonator for the beta-decay experiment PERC*, Physics Procedia **17** (2011) 62 – 68

[21] G. Konrad, H. Abele, M. Beck, C. Drescher, D. Dubbers, J. Erhart, H. Fillunger, C. Gösselsberger, W. Heil, M. Horvath, E. Jericha, C. Clauser, *et al.*, *Neutron Decay with PERC: a Progress Report*, Journal of Physics: Conf. Ser. **340** (2012) 012048, (The PERC Collaboration)

[22] H. Rauch, W. Treimer, U. Bonse, *Test of a single crystal neutron interferometer*, Phys. Lett. A **47** (1974) 369–371

[23] H. Rauch, S. A. Werner, *Neutron Interferometry: Lessons in Experimental Quantum Mechanics, Wave-Particle Duality, and Entanglement. 2nd ed.*, Oxford University Press (2015), ISBN 978-0-19-871251-0

[24] V. V. Nesvizhevsky, H. G. Börner, A. K. Petukhov, H. Abele, S. Baeßler, F. J. Rueß, T. Stöferle, A. Westphal, A. M. Gagarski, G. A. Petrov, A. V. Strelkov, *Quantum states of neutrons in the Earth's gravitational field*, Nature **415** (2002) 297–299

[25] T. Jenke, P. Geltenbort, H. Lemmel, H. Abele, *Realization of a gravity-resonance-spectroscopy technique*, Nature Physics **7** (2011) 468

[26] T. Jenke, G. Cronenberg, J. Burgdörfer, L. A. Chizhova, P. Geltenbort, A. N. Ivanov, T. Lauer, T. Lins, S. Rotter, H. Saul, U. Schmidt, H. Abele, *Gravity resonance spectroscopy constrains dark energy and dark matter scenarios*, Phys. Rev. Lett. **112** (2014) 151105–1–151105–5

[27] H. Lemmel, P. Brax, A. N. Ivanov, T. Jenke, G. Pignol, M. Pitschmann, T. Potocar, M. Wellenzohn, M. Zawisky, H. Abele, *Neutron interferometry constrains dark energy chameleon fields*, Phys. Lett. B **743** (2015) 310–314

[28] G. Badurek, G. P. Westphal, P. Ziegler, *A Fourier neutron time-of-flight diffractometer*, Atomkernenergie **29** (1977) 27–29

[29] G. Badurek, A. Kollmar, A. Seeger, W. Schalt, *Use of a Drabkin spin resonator in inverted geometry neutron time-of-flight spectroscopy*, Nucl. Instr. Meth. Phys. Res. A **309** (1991) 275–283

[30] B. Alefeld, A. Kollmar, G. Badurek, G. M. Drabkin, *Space-time focusing of polarized neutrons*, Nucl. Instr. Meth. Phys. Res. A **306** (1991) 300–304

[31] G. Badurek, H. Weinfurter, S. Wehinger, A. Zeilinger, R. Gähler, A. Kollmar, *The non-dispersive phase of the scalar Aharonov-Bohm effect*, Phys. Rev. Lett. **71** (1993) 307–311

[32] *Strahlenschutzgesetz (StrSchG): Bundesgesetz über Maßnahmen zum Schutz des Lebens oder der Gesundheit von Menschen einschließlich ihrer Nachkommenschaft vor Schäden durch ionisierende Strahlen (Strahlenschutzgesetz - StrSchG)* (2017)

[33] *Strahlenschutzverordnung (StrSchV): Verordnung des Bundesministers für Land- und Forstwirtschaft, Umwelt und Wasserwirtschaft, des Bundesministers für Wirtschaft und Arbeit, des Bundesministers für Verkehr, Innovation und Technologie, der Bundesministerin für Bildung, Wissenschaft und Kultur sowie der Bundesministerin für Gesundheit und Frauen über allgemeine Maßnahmen zum Schutz von Personen vor Schäden durch ionisierende Strahlung (Allgemeine Strahlenschutzverordnung - AllgStrSchV)* (2017)

[34] W. Mach, D. Hainz, A. Musilek, *Beschreibung des neuen Strahlplatzes am Strahlrohr B des TRIGA Reaktors*, Techn. Ber., Atominstitut, TU Wien (2016)

[35] W. Mach, *Ergänzungen zum Dokument 'ATIB1602 - Beschreibung des neuen Strahlplatzes am Strahlrohr B des TRIGA Reaktors'*, Techn. Ber., Atominstitut, TU Wien (2016)

[36] W. Mach, *2. Ergänzungen zum Dokument 'ATIB1602 - Beschreibung des neuen Strahlplatzes am Strahlrohr B des TRIGA Reaktors'*, Techn. Ber., Atominstitut, TU Wien (2017)

[37] H. Smith, *Conversion Coefficients for Use in Radiological Protection Against External Radiation*, ICRP publication 74, Annals of the ICRP 26(1996)3-4, Oxford: Pergamon press (1997), ISBN 0080427391

[38] H. Maier-Leibnitz, *Grundlagen für die Beurteilung von Intensitäts- und Genauigkeitsfragen bei Neutronenstreumessungen*, Nukleonik **8** (1966) 61–67

[39] H. Rauch, *Messung von effektiven Neutronentemperaturen mit einem Neutronen-Kristallspektrometer am TRIGA Mark 2-Reaktor*, Atomkernenergie **10** (1965) 145

[40] B. E. Watt, *Energy spectrum of neutrons from thermal fission of U 235*, Phys. Rev. **87** (1952) 1037–1041

[41] B. Dörschel, L. Herforth, *Neutronen-Personendosimetrie*, Springer Basel AG (1979), ISBN 978-3-0348-5299-9

[42] M. Cagnazzo, C. Raith, T. Stummer, M. Villa, H. Böck, *Measurement of neutron flux distribution and energy spectrum in the horizontal beam tube at the TRIGA Mark II Reactor Vienna*, RRFM Transactions (2014) 336–342

[43] M. Cagnazzo, C. Raith, M. Villa, H. Böck, *Measurement of the In-Core Neutron Flux Distribution and Energy Spectrum at the Triga Mark II Reactor of the Vienna University of Technology/Atominstitut*, NENE conference proceedings (2014)

[44] M. Cagnazzo, *Neutronic modelling of the new TRIGA core and experimental validation*, Dissertation, TU Wien (2018)

[45] C. Raith, *Neutron activation analysis measurement in different energy ranges at the TRIGA Mark II reactor for determination of the neutron spectrum*, Diplomarbeit, TU Wien (2015)

[46] B. Brockhouse, *Crystal filter to produce pure thermal neutron beams from reactors*, Rev. Sci. Instr. **30** (1959) 136–137

[47] *Evaluated Nuclear Data File (ENDF)*, `http://www.nndc.bnl.gov/exfor/endf00.jsp` (2018), accessed: 04.04.2018

[48] I. I. Gurevich, L. V. Tarasov, *Low energy neutron physics*, North-Holland Publ. Co. (1968)

[49] G. E. Bacon, *Neutron Diffraction*, Clarendon Press, Oxford (1975), ISBN 0198513534

[50] L. Liang, R. Rinaldi, H. Schober (Hg.), *Neutron Applications in Earth, Energy and Environmental Sciences*, Springer Science & Business Media (2008), ISBN 978-0-387-09415-1

[51] W. Scharenberg, *Kristallfilter für kalte und thermische Neutronenstrahlen*, Forschungszentrum Jülich GmbH Zentralbibliothek, Verlag, Jül- 875 - RX (1972), http://hdl.handle.net/2128/4466

[52] J. M. Cassels, Progr. Nucl. Phys. **1** (1950) 185

[53] H. Machner, *Einführung in die Kern-und Elementarteilchenphysik*, Wiley Online Library, Kap. 4, Kernmodelle, 127–184 (2013)

[54] D. Sippel, K. Kleinstück, *Über die Verwendung von Wismut als Filter für thermische Neutronen bei Experimenten mit Reaktorstrahlung*, Kernenergie **4** (1961) 839–841

[55] J. P. Barton, *Filters for thermal neutron radiography*, Nondestructive Testing and Evaluation **16** (2001) 95–110

[56] J. G. Barker, D. F. R. Mildner, J. A. Rodriguez, P. Thiyagarajan, *Neutron transmission of single-crystal magnesium fluoride*, J. Appl. Cryst. **41** (2008) 1003–1008

[57] D. F. R. Mildner, G. P. Lamaze, *Neutron transmission of single-crystal sapphire*, J. Appl. Cryst. **31** (1998) 835–840

[58] R. Born, D. Hohlwein, J. R. Schneider, K. Kakurai, *Characterization of a sapphire single crystal for the use as filter in thermal neutron scattering*, Nucl. Instr. Meth. Phys. Res. A **262** (1987) 359–365

[59] M. Bacak, *Design der Strahlungsabschirmung für einen weißen Neutronenstrahl am TRIGA Mark II Forschungsreaktor der TU Wien*, Diplomarbeit, TU Wien (2015)

[60] J. K. Shultis, R. E. Faw, *An MCNP primer*, Techn. Ber., Kansas State University, USA (2011), http://hdl.handle.net/2097/15754

[61] S. Haas, *Simulationen zur Abschirmung von Neutronen mit MCNP*, Diplomarbeit, TU Wien (2013)

[62] J. M. Verbeke, C. Hagmann, D. Wright, *Simulation of neutron and gamma ray emission from fission*, Techn. Ber., UCRL-AR-228518, Lawrence Livermore National Laboratory (2009)

[63] S. Krispel, G. Maier, *Prüfbericht B 14151-1, Entwicklung einer optimalen Betonrezeptur für Strahlenschutz-Schwerbeton BVH Experimentierplatz Atominstitut*, Techn. Ber., Smartminerals GmbH (2015)

[64] W. Mach, E. Jericha, M. Bacak, D. Hainz, A. Musilek, M. Villa, H. Abele, *Installation of a Thermal White Neutron Beam Facility at the TRIGA reactor in Vienna*, NENE 2017 conference proceedings (2017)

[65] F. Hainzl, *Experimental characterization of shielding materials for neutrons and gamma radiation*, Bachelor thesis, TU Wien (2015)

[66] M. Hofer, P. Necker, *Analyse und Simulation der Abschirmungswirkung von mit Bor versetztem Strahlenschutzbeton im Vergleich zu herkömmlichen Baubeton*, Project thesis, TU Wien (2015)

[67] A. Hawlik, *Strahlpräparation am Strahlrohr B des TRIGA Mark II Forschungsreaktors der TU Wien*, Diplomarbeit, TU Wien, in progress (2018)

[68] Fa. Thermo-Scientific, *Gebrauchsanweisung Dosisleistungsmessgerät FH 40 G* (2007)

[69] D. Hainz, G. Hampel, W. Mach, A. Musilek, *Protokoll: Strahlenschutzüberwachung an der Experimentierkammer für den Weißen Strahl bei Routinebetrieb*, Techn. Ber., Radiation protection service, Atominstitut, TU Wien (2017)

[70] D. Hainz, W. Mach, A. Musilek, *Protokoll: Strahlenschutzüberwachung an der Experimentierkammer für den Weißen Strahl bei Routinebetrieb (11.08.2017)*, Techn. Ber., Radiation protection service, Atominstitut, TU Wien (2017)

Bibliography

[71] A. Danner, *Flux and doserate measurements for characterizing a new kind of shielding concrete*, Project thesis,TU Wien (2018)

[72] A. Hefner, *Untersuchungen über die radiologische Gefährdung bei Strahlrohrexperimenten am Trigamark II*, Dissertation, Technische Hochschule Wien (1970)

[73] M. Pangl, *Charakterisierung des thermischen Weißen Strahls am TRIGA Reaktor des Atominstituts*, Diplomarbeit, TU Wien, Wien (2018)

[74] F. Bensch, *Die Absolutmessung der Flußdichte thermischer Neutronen*, Technische Hochschule Wien, Habilitationsschrift (1972)

[75] H. Böck, *Neutron activation foil manual*, Atominstitut, TU Wien (1989)

[76] E. Dyrnjaja, *Application of neutron radiography to fuel cells, hydrogen filled micro hollow spheres, boron micro-inhomogeneities and to plate heat exchangers*, Dissertation, TU Wien (2016)

[77] P. Kavrigin, P. Finocchiaro, E. Griesmayer, E. Jericha, A. Pappalardo, C. Weiss, *Pulse-shape analysis for gamma background rejection in thermal neutron radiation using diamond detectors*, Nucl. Instr. Meth. Phys. Res. A **795** (2015) 88–91

[78] C. Weiß, E. Griesmayer, C. Guerrero, G. Badurek, E. Jericha, H. Leeb, *A new CVD diamond mosaic-detector for (n,α) cross-section measurements at the n_TOF experiment at CERN*, Nucl. Instr. Meth. Phys. Res. A **732** (2013) 190–194

[79] C. B. Lang, N. Pucker, *Mathematische Methoden in der Physik*, Springer-Verlag Berlin Heidelberg (2016), ISBN 978-3-662-49312-0

[80] I. Hughes, T. Hase, *Measurements and their uncertainties: A practical guide to modern error analysis*, Oxford University Press (2010), ISBN 978-0-19-956633-4

[81] H. Sterba, J. M. Welch, Private Communication (2017)

[82] International Atomic Energy Agency & World Health Organization, *International basic safety standards for protecting against ionizing radiation and for the safety of radiation sources*, IAEO Vienna (1996), http://www.who.int/iris/handle/10665/41593

[83] E. Jericha, G. Badurek, M. Trinker, *Ultra-small-angle scattering with polarized neutrons*, Physica B **397** (2007) 88–90

[84] J. Erhart, S. Sponar, G. Sulyok, G. Badurek, M. Ozawa, Y. Hasegawa, *Experimental demonstration of a universally valid error–disturbance uncertainty relation in spin measurements*, Nature Physics **8** (2012) 185

[85] W. G. Williams, *Polarized neutrons*, Clarendon Press, Oxford (1988), ISBN 0-19-851005-5

[86] G. Badurek, *Polarized Neutrons*, Lecture Scripts of the 7th European Winter School on Neutrons and Synchrotron Radiation (2011) 713–769, edts.: O. Paris, H. Amenitsch, E. Bauer, G. Krexner, Ch. Streli, P. Wobrauschek

[87] F. Mezei, *Novel polarized neutron devices: supermirror and spin component amplifier*, Communications on Physics **1** (1976) 81–85

[88] F. D. Colegrove, L. D. Schearer, G. K. Walters, *Polarization of He-3 gas by optical pumping*, Phys. Rev. **132** (1963) 2561–2572

[89] T. G. Walker, W. Happer, *Spin-exchange optical pumping of noble-gas nuclei*, Rev. Mod. Phys. **69** (1997) 629–644

[90] W. Heil, J. Dreyer, D. Hofmann, H. Humblot, E. Lelievre-Berna, F. Tasset, ^3He *neutron spin-filter*, Physica B **267** (1999) 328–335

[91] R. Raab, *Weiterentwicklung eines Wanderwellen-Neutronenspinresonators für sehr kalte Neutronen*, Diplomarbeit, TU Wien (2013)

[92] B. M. Berger, *Experimentelle Umsetzung der Geschwindigkeitsselektion mittels Spinresonanz für sehr kalte Neutronen (VCN)*, Diplomarbeit, TU Wien (2013)

[93] J. Bosina, *Charakterisierung eines 'Badurek'-Resonators für sehr kalte Neutronen*, Diplomarbeit, TU Wien (2015)

[94] A. Frank, *Konzept und Test einer Steuerung für einen magnetischen Wanderwellenresonator zur Wellenlängenselektion von langsamen Neutronen*, Diplomarbeit, TU Wien (2018)

[95] C. Burger, *t.b.a.*, Diplomarbeit, TU Wien (2019)

[96] S. Koerner, B. Schillinger, P. Vontobel, H. Rauch, *A neutron tomography facility at a low power research reactor*, Nuclear Instruments and Methods in Physics Research Section A: Accelerators, Spectrometers, Detectors and Associated Equipment **471** (2001) 69–74

[97] H. Filter, *Preparation of an interference experiment with slow neutrons: A feasibility study of Lloyd Mirror in Earths gravitational field.*, Dissertation, TU Wien (2018)

[98] T. Jenke, G. Cronenberg, H. Filter, P. Geltenbort, M. Klein, T. Lauer, K. Mitsch, H. Saul, D. Seiler, D. Stadler, M. Thalhammer, H. Abele, *Ultracold neutron detectors based on 10B converters used in the qBounce experiments*, Nuclear Instruments and Methods in Physics Research Section A: Accelerators, Spectrometers, Detectors and Associated Equipment **732** (2013) 1 – 8

[99] C. Gösselsberger, H. Abele, G. Badurek, E. Jericha, W. Mach, S. Nowak, T. Rechberger, *Neutron beam tailoring by means of a novel pulsed spatial magnetic spin resonator*, *Journal of Physics: Conference Series*, Bd. 340, IOP Publishing (2012), Bd. 340, 012–028

Acknowledgments

Auch wenn letztendlich mein Name auf der ersten Seite dieser Arbeit steht, so wäre es undenkbar, dass sie ohne Unterstützung von den unterschiedlichsten Seiten zu Stande gekommen wäre. Experimentalphysik bedeutet Teamarbeit, das ist mir durch diese Arbeit klar geworden.

Das Team:

Vielen Dank an Prof. Gerald Badurek und Prof. Hartmut Abele für die Ermöglichung des Themas. Ohne die zahlreichen Diskussionen wäre diese Arbeit nicht möglich!

Ein besonderer Dank gilt Dr. Erwin Jericha, der durch unzählige Diskussionen, Ideen und Geistesblitze meinen Alltag und dadurch auch diese Arbeit auf besondere Weise geprägt hat. Keine Frage war Dir, Erwin, zu blöd, keine Diskussion zu lang! Von Dir habe ich nicht nur unglaublich viel über Neutronen gelernt, sondern auch über das Leben!

Danke an das Reaktorteam und das Team des betrieblichen Strahlenschutzes: von Euch habe ich gelernt, wie ein Kernreaktor und der Strahlenschutz in all ihren physikalischen, technischen, rechtlichen und organisatorischen Details funktionieren!

Dank gebührt natürlich auch allen meinen Studienkollegen: Joachim Bosina, Gunther Cronenberg, Eva Dyrnjaja, Hanno Filter, Andreas Fuchs, Johannes Hans Hecher, Michael Klopf, Robert Raab, Tobias Rechberger, Martin Thalhammer. Unzählige Tipps & Tricks, Kaffees und Diskussionsrunden haben den Alltag geprägt, aufgelockert und erleichtert!

Danke an die 18 Projekt-, Bachelor- und Diplomstudenten, die ich mitbetreuen durfte. Die Diskussionen mit Euch allen waren äußerst fruchtbar!

Herzlichen Dank an all die helfenden 'Hände' aus der mechanischen Werkstätte, der E-Werkstatt, der Buchhaltung, dem Sekretariat und der Haustechnik.

Einen ganz besonderen Dank für offene Ohren, und helfende Hände sowie Pfoten gebührt natürlich auch meinem Bruder Rainer und in herausstechender Weise meiner Freundin Elli und meinem Hund Alegra. Danke, dass ihr mich und die Achterbahn der Gefühle, die man Dissertation nennt, ausgehalten habt.

> *'If I have seen further it is by standing on y^e shoulders of giants.'*
>
> - Sir Isaac Newton
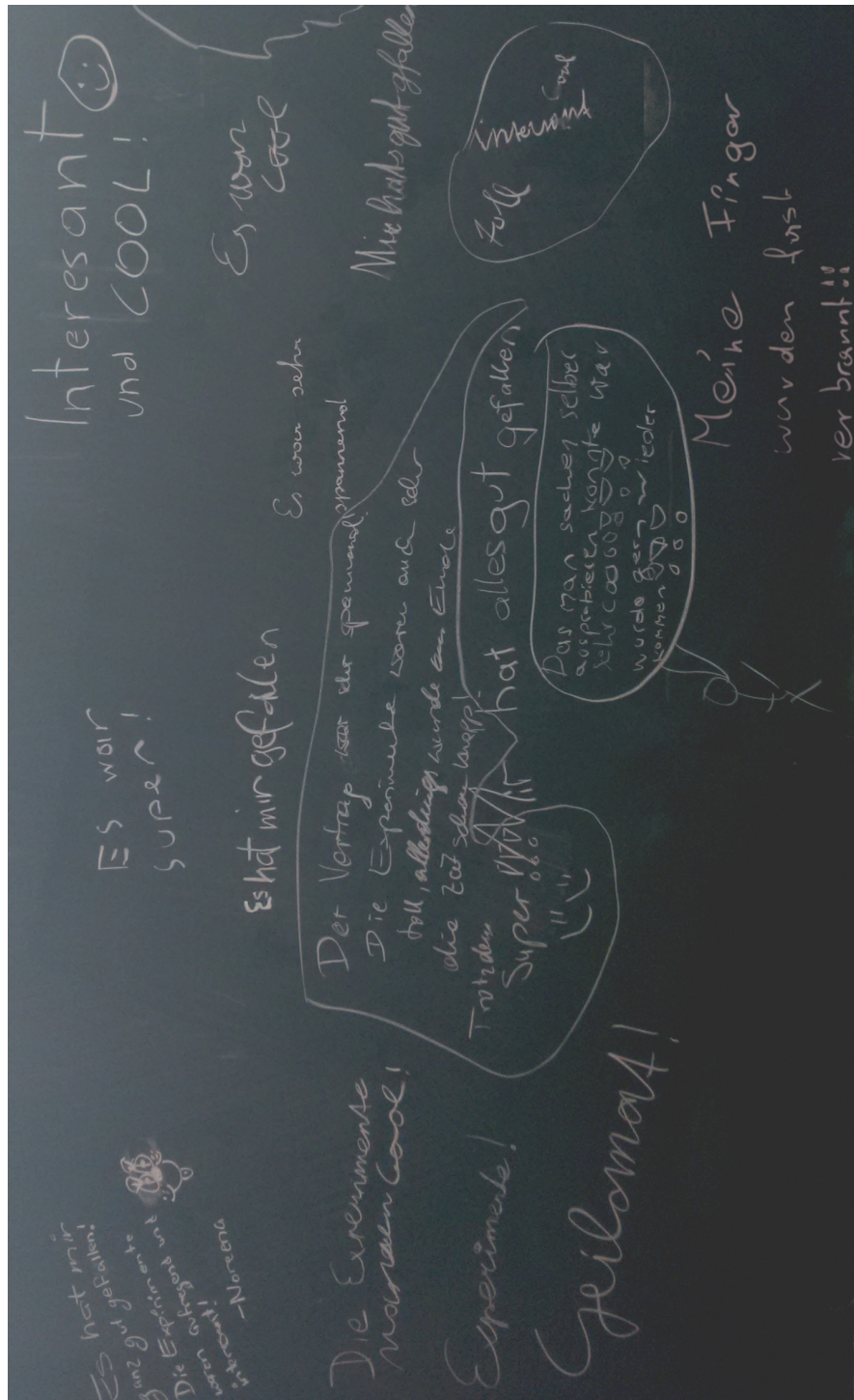
"Es war super!",

"Interessant und cool!",

"Experimente! Geilomat!",

"Ich fand gut, dass man manche Experimente selber machen konnte.",

"Der Vortrag war sehr spannend! Die Experimente waren auch sehr toll, allerdings wurde am Ende die Zeit sehr knapp!",

"Meine Finger wurden fast verbrannt!!"

Ehrliches Feedback von Kindern der Kinderuni 2015, das auch ausgezeichnet zu dieser Dissertation passt.

Curiculum Vitæ

PERSON

Name	**Dipl.Ing Wilfried Mach**
Adress	Franz-Glaser-Gasse 36, 1170 Wien
Telephone	0676/72-82-665
E-Mail	willi@mach.at
Nationality	Austrian
Date of birth	12.02.1987

EDUCATION

2014 - now	**Ph.D. (experimental physics, neutron physics), Atominstitut, TU Wien**
2013	**Master's Thesis**, (neutron physics), Atominstitut, TU Wien "Modellunabhängige Datenanalyse von Ultrakleinwinkelstreuung mit polarisierten Neutronen"
2012	Research stay (two months) at CERN, Switzerland
2011	Exchange semester at the University of Loughborough, England
2010 - 2013	Master's Degree, Faculty of Physics, TU Wien
2006 - 2010	**Bachelor's Degree**, Faculty of Physics, TU Wien
2005	Matura, with focus in Mathematics, Physics, English and Fine Arts.
1997 - 2005	Realgymnasium Geblergasse, Vienna

LANGUAGES:

German (native)
English (fluent)
French (basic)

PUBLICATIONS:

- E. Jericha, J. Bosina, P. Geltenbort, M. Hino, W. Mach, T. Oda, G. Badurek, *Neutron detection in the frame of spatial magnetic spin resonance*, Nucl. Instr. Meth. Phys. Res. A **845** (2017) 552–555

- W. Mach, E. Jericha, M. Bacak, D. Hainz, A. Musilek, M. Villa, H. Abele, *Installation of a Thermal White Neutron Beam Facility at the* triga *reactor in Vienna*, NENE 2017 conference proceedings (2017)

- C. Gösselsberger, H. Abele, G. Badurek, E. Jericha, W. Mach, S. Nowak, T. Rechberger, *Neutron beam tailoring by means of a novel pulsed spatial magnetic spin resonator*, *Journal of Physics: Conference Series*, Bd. 340, IOP Publishing (2012), Bd. 340, 012028